

A DISSERTATION FOR THE DEGREE OF DOCTOR OF PHILOSOPHY

**Heterogeneous Polymer Design of
Acrylic Pressure-Sensitive Adhesives for Flexible Displays**

유연 디스플레이용 아크릴 점착 소재의
비균질 고분자 설계

Advisor: Hyun-Joong Kim

by

Ji-Soo Kim

PROGRAM IN ENVIRONMENTAL MATERIALS SCIENCE

GRADUATE SCHOOL

SEOUL NATIONAL UNIVERSITY

FEBRUARY, 2024

SEOUL NATIONAL UNIVERSITY
GRADUATE SCHOOL
PROGRAM IN ENVIRONMENTAL MATERIALS SCIENCE

WE HEREBY RECOMMEND THE THESIS BY
Ji-Soo Kim

ENTITLED

Heterogeneous Polymer Design of Acrylic Pressure-Sensitive Adhesives
for Flexible Displays

BE ACCEPTED IN FULFILLMENT OF THE REQUIREMENTS FOR
THE DEGREE OF DOCTOR OF PHILOSOPHY

JANUARY, 2024

COMMITTEE ON FINAL EXAMINATION

Chairman

Prof. Jong Chan Lee

Co-Chairman

Prof. Hyun-Joong Kim

Member

Ph. D. Ick-Kyung Sung

Member

Ph. D. Jae Heung Lee

Member

Ph. D. Youngdo Kim

Abstract

Heterogeneous Polymer Network Design of Acrylic Pressure-Sensitive Adhesives for Flexible Displays

Ji-Soo Kim

Program in Environmental Materials Science

Graduate School

Seoul National University

Research on the development of acrylic pressure-sensitive adhesives (PSAs) for the new generation of optical and electrical device components is underway, as acrylic polymers offer excellent transparency and exhibit good adhesion properties through the PSA molecule itself. Elastic behavior over a broader strain range is necessary for use in high-tech functional materials like stretchable displays. To date, the main focus of improvement has been on reducing the low-temperature modulus of adhesive materials. However, current techniques for improving the flexibility of acrylic adhesive films have limitations that hinder progress in adhesive properties. Therefore, this study aims to enhance both elasticity and adhesion properties by heterogenizing the network structure of adhesive materials. The heterogeneous polymer network undergoes notable changes in its physical properties, making it an excellent contender for various applications, such as electrodes and porous carriers. Researchers are currently conducting studies grounded in introductory physical chemistry to better understand the structure and properties of the heterogeneous

copolymer. Therefore, the morphological, molecule structural, and physical understanding of the adhesive material using non-homogenization of acrylic copolymers becomes a worthwhile topic of exploration.

This paper is focused on the molecular structure of acrylic polymers using photolithography and PIMS, respectively. The properties of the adhesive material resulting from polymer heterogeneity were systematically investigated from rheological and mechanical aspects. We studied the morphology and properties of thin films as a function of the polymer crosslinking network and the chain end length. We aimed to contribute to a deeper understanding of the micro phase behavior of heterogeneous copolymer thin films and increase their application potential.

In Chapter 1, we summarized the importance of research on improving the flexible properties of acrylic adhesive materials. We summarized the theoretical and experimental results on improving the properties of adhesive materials through heterogenization. In addition, polymerization-induced microphase separation, in short, PIMS, which was used as the primary technique for heterogenization of acrylic copolymers in this study, was introduced.

In Chapter 2, basic research on the application of photolithography was conducted. The photolithographic method was used to prepare a heterogeneous adhesive material. The possibility of improving the recovery and adhesion properties of heterogeneous adhesive materials was confirmed.

In Chapter 3, a crosslinked network with linear PBA as chain ends was prepared by PIMS using living radical polymerization. The relationship between the network structure, phase behavior, and the rheological and physical properties was studied. An extensive range of linear elastic behavior of the prepared heterogeneous adhesive material was confirmed.

In Chapter 4, we reported a STEM measurement of the micro phase behavior of the copolymer network as a function of the length of the linear PBA block at

the end of the chain. The self-assembly morphology of living radical polymerization-induced microphase separation polymers was visualized and analyzed. Furthermore, the molecular structure was elaborated and clarified based on the Flory-Rehner equation. The molecular structural analysis and physical properties of adhesive materials with nano-scale heterogeneity are studied. The applicability of heterogeneous PSA as transparent adhesive materials for flexible displays was examined.

Keywords: Acrylic Pressure-Sensitive Adhesive, Flexible OCA, Elastomer, Heterogeneous, Photolithography, Polymerization-induced Microphase Separation.

Student Number: 2018-29259

Table of Contents

Chapter 1

Introduction

| | |
|---|-----------|
| 1. Introduction | 2 |
| 1.1 Pressure-Sensitive Adhesives | 2 |
| 1.2 Optically Clear Adhesive for Flexible Display | 3 |
| 1.3 Introduction of Heterogeneous Material | 6 |
| 1.3.1. Methods for Property Control of PSA | 6 |
| 1.3.2. Elastic Property of Heterogeneous Material | 7 |
| 1.3.3. Adhesion Property of Heterogenous Material | 9 |
| 1.3.4. Artificial Method of Heterogeneity | 11 |
| 1.3.5. Spontaneous Method of Heterogeneity | 14 |
| 1.4 Introduction of Polymerization-Induced Microphase Separation. | 14 |
| 1.4.1 Micro phase Separation and Flory-Huggins Parameter | 14 |
| 1.4.2. Driving Force and Mechanism of in-situ Nano-Structuring | 17 |
| 1.4.3. Factors controlling Polymerization-Induced Microphase Separation | 19 |
| 2. Literature review | 21 |
| 2.1. Mechanism of Improving Physical Properties of Heterogenous PSA | 21 |
| 2.2. Macro Scale Heterogeneous PSA by Photo Lithography | 22 |
| 2.3. Nano Scale Heterogeneous PSA by in-situ Nano-Structuring | 25 |
| 3. Objectives | 28 |
| 3.1. Understanding the Properties of Heterogeneous PSAs | 28 |
| 3.2. Fabrication of Novel Nano Structured Heterogeneous PSA | 29 |
| 3.3. Influence of Polymer Network on Elasticity | 30 |

Chapter 2

Macro Scale Heterogeneous PSA using UV Patterning

| | |
|---|-----------|
| 1. Introduction | 33 |
| 2. Experimental | 35 |
| 2.1. Fundamental Study on UV Curing System for Acrylic PSA | 35 |
| 2.1.1. Materials | 35 |
| 2.1.2. Synthesis of the Pre-polymer | 36 |
| 2.1.3. UV Curing Condition controlling Polymer Structure and Property | 36 |
| 2.1.4. UV/UV Step Curing | 39 |
| 2.1.5. Characterization | 40 |
| 2.2. Heterogeneous PSA using UV Patterning | 46 |
| 2.2.1. Materials | 46 |
| 2.2.2. Preparation of UV Patterned Acrylic PSA film | 46 |
| 2.2.3. Characterization | 49 |
| 3. Results and Discussion | 51 |
| 3.1. UV Curing System controlling Polymer Structure and Property | 51 |
| 3.1.1. Molecular Structure: Conversion and Gel Fraction | 51 |
| 3.1.2. Mechanism of Structure Change: EPR and Real Time FT-IR | 55 |
| 3.1.3. Mechanical Properties according to the Polymer Network Structure | 57 |
| 3.2. UV/UV Step Curing | 61 |
| 3.2.1. Kinetic Study for UV/UV Step Curing | 61 |
| 3.3. Heterogeneous PSA using UV Patterning | 65 |
| 3.3.1. Identification of the UV Pattern Formation | 65 |
| 3.3.2. Viscoelastic Property: Storage Modulus | 67 |
| 3.3.3. Flexibility: Strain Recovery and Stress Relaxation Properties | 68 |
| 3.3.4. Applicability to OCA: Adhesion Properties and Transmittance | 70 |
| 4. Conclusions | 73 |

Chapter 3

Nano Scale Heterogeneous PSA

using Polymerization-Induced Microphase Separation

| | |
|---|-----------|
| 1. Introduction | 76 |
| 2. Experimental | 78 |
| 2.1. Materials | 78 |
| 2.2. Synthesis of 2-(butylthiocarbonothioylthio) Propanoic Acid | 78 |
| 2.3. RAFT Polymerization of Macro CTA (PBA ₉₆ -CTA) | 79 |
| 2.4. Aminolysis of Macro-CTA | 80 |
| 2.5. Preparation of the Nanostructured PSA Specimens | 81 |
| 2.5.1. Homogeneous PSA | 81 |
| 2.5.2. PIMS PSA | 83 |
| 2.5.3. Blend PSA | 84 |
| 2.5.4. Crosslinked Polymer Matrix of Heterogeneous PSAs. | 84 |
| 2.6. Characterization | 85 |
| 2.6.1. Nuclear Magnetic Resonance (NMR) Spectroscopy | 85 |
| 2.6.2. Gel Permeation Chromatography (GPC) | 85 |
| 2.6.3. Transmission Electron Microscope (TEM) | 85 |
| 2.6.4. Wide Angle X-ray Scattering (WAXS) | 85 |
| 2.6.5. DSC Measurement | 86 |
| 2.6.6. Storage Modulus and T_g | 86 |
| 2.6.7. Tensile Test and Cyclic Stretching-Recovery Property | 86 |
| 2.6.8. Adhesion Property | 87 |
| 2.6.9. Stress Relaxation Test | 87 |
| 3. Results and Discussion | 88 |
| 3.1. Results of Synthesis and Polymerization | 88 |

| | |
|---|------------|
| 3.1.1. Synthesis of 2-(butylthiocarbonothioylthio) Propanoic Acid | 88 |
| 3.1.2. RAFT Polymerization of Macro-CTA | 89 |
| 3.1.3. Aminolysis of Macro-CTA | 90 |
| 3.2. Confirmation of Heterogeneous Structure | 91 |
| 3.2.1. TEM Image | 91 |
| 3.2.2. WAXS | 91 |
| 3.2.3. Glass Transition Temperature of Heterogeneous PSAs | 94 |
| 3.3. Rheological Properties according to Heterogeneous Structure | 96 |
| 3.3.1. Rheological Properties | 96 |
| 3.3.2. Tensile Test | 99 |
| 3.3.3. Cycle Test | 100 |
| 3.4. Mechanical Properties according to Polymer Network Structure | 104 |
| 3.4.1. Stress Relaxation Test | 104 |
| 3.4.2. Adhesion Properties | 104 |
| 4. Conclusions | 107 |

Chapter 4

Influence of PBA Chain Length of Polymerization-Induced Microphase Separated PSA on Molecular Structures and Properties.

| | |
|---|------------|
| 1. Introduction | 109 |
| 2. Experimental | 110 |
| 2.1. RAFT Polymerization of Macro CTA with M_n Variation | 110 |
| 2.2. Preparation of the PIMS PSA Specimens | 111 |
| 2.3. Characterization | 114 |
| 2.3.1. Transmission Electron Microscope (TEM)..... | 114 |
| 2.3.2. Stress Relaxation Test..... | 114 |
| 2.3.3. Adhesion Property | 114 |
| 2.3.4. Swelling Test..... | 115 |
| 2.3.5. Folding Test | 115 |
| 3. Results and Discussion | 118 |
| 3.1. Results of Synthesis and Polymerization..... | 118 |
| 3.1.1. Synthesis of 2-(butylthiocarbonothioylthio) Propanoic Acid | 118 |
| 3.1.2. Synthesis of Macro-CTA | 118 |
| 3.2. Morphology of Heterogeneous PSA | 121 |
| 3.2.1. TEM | 121 |
| 3.2.2. SAXS and WAXS | 127 |
| 3.3. Rheological Properties according to Heterogeneous Structure | 129 |
| 3.3.1. Rheological Properties | 129 |
| 3.3.2. Tensile Test..... | 133 |
| 3.4. Mechanical Properties according to Heterogeneous Structure | 135 |
| 3.4.1. Stress Relaxation Test..... | 135 |

| | |
|--|------------|
| 3.4.2. Adhesion Properties | 138 |
| 3.5. Polymer Network Structure according to PBA Chain Length Variation | 140 |
| 3.5.1. Calculation of Molecular Weight between Crosslinking by Swelling Test | 140 |
| 3.5.2. Schematic Molecular Structure | 148 |
| 3.6. Application Test | 150 |
| 3.6.1. Folding Test | 150 |
| 3.6.2. Transmittance and Haze | 155 |
| 4. Conclusions | 158 |

Chapter 5

Overall Conclusions

| | |
|---|------------|
| 1. Overall Conclusions | 161 |
| 1.1. Identify the Potential for Improving Properties of Heterogeneous PSA | 162 |
| 1.2. Fabrication of Novel Nano Structured Heterogeneous PSA | 163 |
| 1.3. Study of Polymer Network exhibiting Linear Elasticity | 164 |

| | |
|-------------------------|------------|
| References | 165 |
|-------------------------|------------|

| | |
|--------------------|------------|
| 국문 초록 | 192 |
|--------------------|------------|

List of Tables

| | |
|---|-----|
| Table 2-1. Compositions of the raw materials used for the synthesis of pre-polymers. | 35 |
| Table 2-2. UV curing conditions of UV patterned PSA film. | 47 |
| Table 3-1. Compositions of mixtures applied to manufacture the nanostructured PSAs. R: homogeneous random copolymer; B: micro phase separated PIMS PSA containing soft block of PBA, L: macro phase separated PSA blended with linear PBA. | 82 |
| Table 3-2. T_g (°C) measured with DSC and DMA shear sandwich mode. ... | 95 |
| Table 4-1. Compositions of bulk mixtures applied to cast the PIMS PSAs (mol%). | 113 |
| Table 4-2. Characterization of macro-CTAs synthesized by RAFT-mediated polymerization of butyl acrylate in acetonitrile. | 120 |
| Table 4-3. Summary of morphology characterization for homogeneous(R) and heterogeneous (B80, B100, B200, B2000, B8000) materials. ... | 126 |
| Table 4-4. F_i and V_i of atomic group of poly butyl acrylate. | 141 |
| Table 4-5. Calculated M_{BB} and M_{CE} of the prepared PSA samples. | 144 |
| Table 4-6. Haze of the PSA samples and PET films. Since the PSA was measured between two PET films, control refers to two of PET films. | 156 |

List of Figures

| | |
|--|----|
| Figure 1-1. Enhancement in peel force for various levels of heterogeneity (Xia, <i>et al.</i> , 2013). | 11 |
| Figure 1-2. Step-and-repeat and step-and-scan configurations and light intensity of photo masked light. | 12 |
| Figure 1-3. The schematic diagram showing the formation of a polymeric relief image using lithography. | 13 |
| Figure 1-4. Representative polymer-polymer phase behaviors that can be realized with different molecular architectures (Bates, 1991). | 16 |
| Figure 1-5. Schematic illustration of a) PIPS, b) PISA, and c) PIMS processes. | 18 |
| Figure 1-6. Imaginary 3D phase diagram illustrating the PIMS process starting with a polymerization mixture of polymer A in monomer b (Huang and Lodge, 1998). | 20 |
| Figure 1-7. Fabrication of UV patterned PSA.(Yoo, <i>et al.</i> , 2021) | 23 |
| Figure 1-8. UV patterned PSA which contain both high and low cured region (Back, <i>et al.</i> , 2019). | 24 |
| Figure 1-9. Relationship of storage modulus and flexibility of UV patterned and non-patterned PSA (Back, <i>et al.</i> , 2019). | 25 |
| Figure 1-10. Synthesis of acrylic block PSA via RAFT polymerization (Sajjad, <i>et al.</i> , 2020). | 26 |
| Figure 1-11. Polymerization-induced microphase separation (PIMS) mechanism and resulting materials. a) PIMS process. b - d) AFM phase images in tapping mode. e) Small-angle x-ray scattering (SAXS) profiles of the materials (Bobrin, <i>et al.</i> , 2022). | 27 |
| Figure 1-12. Comprehensive objectives of this study. | 28 |
| Figure 1-13. Comprehensive experimental flow of this study. | 31 |

| | |
|--|----|
| Figure 2-1. Synthesis of the OCA prepolymer. | 37 |
| Figure 2-2. Appearance and structure of the UV LED curing device. | 38 |
| Figure 2-3. UV/UV step curing process for the acrylic PSA. | 40 |
| Figure 2-4. Instrumental set-up for real-time infrared spectroscopy analysis of ultrafast photopolymerizations. | 42 |
| Figure 2-5. a) Process of manufacturing the UV patterned PSA film. b) Schematic diagram of the curing degree of UV patterned PSA containing quantitative size of the pattern repeating unit. | 48 |
| Figure 2-6. Effects of UV light intensity on the gel fraction of acrylic PSA samples as a function of a) UV exposure energy and b) exposure time. The lines are drawn for easier figure reading. | 53 |
| Figure 2-7. Effects of UV light intensity on the curing conversion of acrylic PSA films as a function of a) UV exposure energy and b) exposure time. | 54 |
| Figure 2-8. In-situ initiated radical concentration of each UV intensity measured by EPR. | 55 |
| Figure 2-9. Change of C double bond conversion for each UV light intensity, measured by real time FT-IR. | 56 |
| Figure 2-10. Differences in the number of propagating chains and hence differences in the final polymer network structure due to differences in the number of radicals initiated at low versus high UV intensity. | 57 |
| Figure 2-11. Physical properties of cured PSA film as a function of curing UV intensity. a) peel strength, b) lap shear strength, c) strain recovery, and d) shear strain. | 60 |
| Figure 2-12. Real-time heat flow after a) primary and b) secondary curing step. Area under the exothermic curves corresponding to c) primary and d) secondary curing step. | 63 |

| | |
|---|----|
| Figure 2-13. Maximum heat flows and corresponding approach times for a) primary and b) secondary curing step. | 64 |
| Figure 2-14. Young's modulus data of a) sea and b) island region of the UV pattern cured PSA samples. | 66 |
| Figure 2-15. a) Storage modulus data measured by rheometer of the UV pattern cured PSA samples (25 °C, angular frequency of 10 rad/s). | 68 |
| Figure 2-16. a) Strain recovery property, and b) stress relaxation property of the UV pattern cured PSA samples. The relationship between the storage modulus and strain recovery, with the trend line calculated by the least squares method, c) pattern 5 and 4~9 composed of a highly cured connected region d) pattern 5 and 1~4 composed of a highly cured island region. | 71 |
| Figure 2-17. a) Peel strength, b) probe tack, and c) transmittance property of the UV pattern cured PSA samples. | 72 |
| | |
| Figure 3-1. Synthesis of 2-(butylthiocarbonothioylthio) propanoic acid | 79 |
| Figure 3-2. RAFT polymerization of PBA ₉₆ -CTA | 80 |
| Figure 3-3. Synthesis of inert PBA ₉₆ via aminolysis of PBA ₉₆ -CTA in the presence of methyl acrylate. | 81 |
| Figure 3-4. Photoinitiated RAFT copolymerization of AA, BA, and PEGDA in the presence of PBA ₉₆ -CTA and TPO. | 83 |
| Figure 3-5. Preparing heterogeneous polymer network using PIMS. | 84 |
| Figure 3-6. ¹ H-NMR result of BTPA synthesized. | 88 |
| Figure 3-7. ¹ H-NMR result of RAFT polymerized PBA ₉₆ -CTA. *: residual BA monomer. | 89 |

| | |
|--|-----|
| Figure 3-8. ¹ H-NMR result of inert PBA96 linear polymer chain which is removed BTPA by aminolysis. The by-product, methyl 3-(hexylamino) propanoate was detected. | 90 |
| Figure 3-9. TEM images of the cured PSA. a, d) R0.5; b, e) B40, and c, f) L40, magnification: a, b, c) 20000 x, d, e, f) 50000 x. | 92 |
| Figure 3-10. a) WAXS data of the homogeneous (R0.5), microphase separated (B30, B40), and macro phase separated PSA (L30, L40). b) Graph scaled from 0 to 0.2 | 93 |
| Figure 3-11. Heat flow curves of homogeneous(R), microphase separated(B30, B40), and macro phase separated PSA (L30, L40) measured by DSC measurements. | 95 |
| Figure 3-12. a) Storage modulus and b) tan delta curves of homogeneous (R), micro phase separated (B30, B40), and macro phase separated PSA (L30, L40), measured by temperature sweep test. | 97 |
| Figure 3-13. a) Storage and b) tan delta curves of homogeneous (R), micro phase separated (B30, B40), and macro phase separated PSA (L30, L40), measured by frequency sweep test. | 98 |
| Figure 3-14. Stress-strain curve of tensile test. a) Homogeneous PSA (R), b) micro phase separated PSA (B30, B40), and c) macro phase separated PSA (L30, L40). | 101 |
| Figure 3-15. a) Young modulus and b) strain at elastic limit of homogeneous PSA (R), micro phase separated PSA (B30, B40), and macro phase separated PSA (L30, L40). | 102 |
| Figure 3-16. Load and unload stress-strain curves of a) R0.1, b) B40, c) Net dissipated energy per each cycle. | 103 |
| Figure 3-17. a) Stress relaxation, b) strain, c) normalized stress curve of the PSAs. | 105 |
| Figure 3-18. Calculated values of a) strain recovery and b) stress relaxation properties, c) Peel strength of PSAs. | 106 |

| | |
|---|-----|
| Figure 4-1. RAFT polymerization of Macro CTA with M_n variation. $n = 70, 80, 100, 200, 1000, 2000, 8000$ | 110 |
| Figure 4-2. Photoinitiated RAFT copolymerization of AA, BA, and PEGDA in the presence of PBA_n -CTA and TPO. | 112 |
| Figure 4-3. Molecular schematic of chain extension of PBA_n -CTA. | 112 |
| Figure 4-4. Structure of a) the actual foldable display and b) the test specimen used for folding test (Back, <i>et al.</i> , 2022). | 116 |
| Figure 4-5. a) Outside and b) inside view of the equipment for the dynamic folding test. c) Scheme for the in-fold test procedure. d) Pictures of the folding plate (w/o specimen, side view, top view, and set test view) (Back, <i>et al.</i> , 2022). | 117 |
| Figure 4-6. NMR spectra of RAFT polymerized PBA_n -CTAs. *: residual BA monomer. The spectra normalized by a resonance at 4.03 ppm. · | 119 |
| Figure 4-7. STEM images of a) homogeneous PSA and PIMS PSA samples prepared with b) PBA_{80} -CTA, c) PBA_{100} -CTA, d) PBA_{200} -CTA, e) PBA_{2000} -CTA, f) PBA_{8000} -CTA. (Magnification: 10k) | 122 |
| Figure 4-8. STEM images of a) homogeneous PSA and PIMS PSA samples prepared with b) PBA_{80} -CTA, c) PBA_{100} -CTA, d) PBA_{200} -CTA, e) PBA_{2000} -CTA, f) PBA_{8000} -CTA. (Magnification: 25k) | 123 |
| Figure 4-9. STEM images of a) homogeneous PSA and PIMS PSA samples prepared with b) PBA_{80} -CTA, c) PBA_{100} -CTA, d) PBA_{200} -CTA, e) PBA_{2000} -CTA, f) PBA_{8000} -CTA. (Magnification: 25k) | 125 |
| Figure 4-10. Schematic illustration of microphase separated morphology. PBA domains are shown in purple; crosslinked P(BA-stat-AA-stat-PEGDA) domains are shown in green. D_{TEM} : PBA domain width, L_{TEM} : PBA domain length, d_{TEM} : domain spacing. | 126 |
| Figure 4-11. Representative a) SAXS and b) WAXS data of PIMS PSA (blue lines) and the homogeneous PSA (black line). | 128 |

| | |
|---|-----|
| Figure 4-12. Temperature-dependent a) storage modulus and b) loss factor of homogeneous PSA (black line) and PIMS PSA samples (blue lines). | 130 |
| Figure 4-13. Stress-strain curves of homogeneous PSA (black line) and PIMS PSA samples (blue lines). | 134 |
| Figure 4-14. Schematic of increasing elasticity and toughness of highly entangled polymer networks(Li, <i>et al.</i> , 2022) | 134 |
| Figure 4-15. Variation of a) strain, b) stress, and c) normalized stress during a stress relaxation test. | 136 |
| Figure 4-16. a) Stress relaxation of PSA samples after loading 100% strain for 10 min. b) Strain recovery of each PSA sample after 5 min of recovery time. | 137 |
| Figure 4-17. a) Peel strength and b) probe tack of PSA samples. | 139 |
| Figure 4-18. Hypothetical segment λ connecting the end of the backbone (BB) segment and the middle of the crosslinker (XC) segment (Borges, <i>et al.</i> , 2020) | 142 |
| Figure 4-19. a) Total molecular weight between crosslinks and entanglement and b) gel fraction of the PSA samples. | 146 |
| Figure 4-20. a) Ratio of the length of the chain end to the length of the backbone between the crosslink and entanglement points and b) crosslinking density of the PSA samples. | 147 |
| Figure 4-21. Schematic diagram of the PSA polymer network. | 149 |
| Figure 4-22. The folding cycle number at which each sample failed in the room temperature, low temperature, and high temperarue/humidity folding tests. | 150 |
| Figure 4-23. PSA samples after 200k folding test at 25 °C. a) B70, b) B80, c) B100, d) B200, e) B1000, f) B2000, g) B8000, h) R. | 151 |
| Figure 4-24. PSA Samples after 30k folding test at -20 °C. a) B70, b) B80, c) B100, d) B200, e) B1000, f) B2000, g) B8000, h) R. | 152 |

Figure 4-25. PSA Samples after 50k folding test at 60 °C/93 %RH. a) B70, b) B80, c) B100, d) B200, e) B1000, f) B2000, g) B8000, h) R. 153

Figure 4-26. a) Peel strength at high temperature (60 °C) of representative PSA samples. b) Strain recovery properties at low temperature (-20 °C) of representative PSA samples. 154

Figure 4-27. Transmittance property of the PSA samples and PET film. ... 155

Figure 4-28. A photograph showing the transparency of the PSA samples. a) B70, b) B80, c) B100, d) B200, e) B1000, f) B2000, g) B8000, h) R. 157

Chapter 1

Introduction

1. Introduction

1.1 Pressure-Sensitive Adhesives

Pressure-sensitive adhesives (PSAs) are defined by the ease of ‘low pressure’ attachment to various substrates. They can be easily detached from partner substrates without adhesion failure (Czech, *et al.*, 2009, Satas, 1989). PSAs have been used in a wide range of industrial fields, such as medical products, electronics, automobiles, and displays (Czech, 2007, Czech, *et al.*, 2012, Ishikawa, *et al.*, 2016, Maag, *et al.*, 2000, Park, *et al.*, 2016, Tan, *et al.*, 1999). PSAs are classified according to monomer type, including acrylic PSAs, rubber-based PSAs, and silicone PSAs. Among these PSAs, acrylic PSAs have been broadly used because of the availability of a wide range of acrylic monomers, their optically transparent properties, and their compatibility with high-performance ultraviolet (UV) curing systems (Decker, 1998).

Acrylic PSAs can be obtained through various polymerization processes such as the emulsion (Czech and Pelech, 2009, Pokeržnik, *et al.*, 2015), solvent-type (Micutz, *et al.*, 2016), water-borne (Hösel, *et al.*, 2013), and radiation polymerization techniques (Lee, *et al.*, 2014). However, much attention has recently been devoted to using more environmental friendly processes, such as the ultraviolet (UV) technique. PSAs may be produced using UV-curing systems through exposure to UV light in the presence of a suitable photoinitiator, which induces radical photopolymerization and promotes the conversion of the monomer to oligomers. This process has many advantages (e.g., it is solvent-free and has a low volatile organic compound content), which are important in industries such as coating, painting, and adhesive production (Czech, *et al.*, 2011, Kajtna, *et al.*, 2013, Noori, *et al.*, 2018).

1.2 Optically Clear Adhesive for Flexible Display

In modern electronic devices, the display, as a standard human-machine interface, is a core component (Jung, *et al.*, 2014, Koo, *et al.*, 2008). The display connects user feedback and machine data by visually conveying the world of bits to humans. Therefore, the display is essential for humans to understand and use the Internet of Things (IoT) technology, which leads to the 4th industrial revolution and rapidly developed (Geffroy, *et al.*, 2006, Li, *et al.*, 2016, Park, *et al.*, 2009, Zhou, *et al.*, 2006). With display technology development, PSA has been commonly used to assemble display components (Lee, *et al.*, 2016) because of the high viscoelasticity (Lee, *et al.*, 2017) and gap-filling ability of the PSA. PSA minimizes the discrepancy of the refractive index, thereby making the display image clear (Park, *et al.*, 2015). When applying low pressure, PSA adheres to the substrate and can be peeled off again without residue (Benedek, *et al.*, 2008). It is suitable to be introduced into the display assembly process since it does not require post-treatment such as solvent drying and heat treatment after bonding with pressure (Creton, 2003, Mapari, *et al.*, 2020). Depending on the composition of PSA, acrylic, silicone, and urethane compositions are typical (Benedek, 2020). Among them, transparent acrylic PSA, which does not require an additional tackifier (Barisa, *et al.*, 2014), is mainly used as an optically clear pressure-sensitive adhesive (OCA) material for display assembly. Without OCA, the light from the backlight unit is reflected at the interface between each film and the air due to the differences in the refractive index. Finally, less than 10% of light reaches to user's eyes (Tanase, *et al.*, 1998). The presence of OCA affects the clarity of the display screen because OCA between films not only holds the film together but also prevents loss of light. Also, the difference in the refractive index between layers decreases, and a similar refractive index allows the straight progress of light

without loss (Park, *et al.*, 2016). So, OCA should basically be transparent and have a low haze. It should also be optically isotropic, with less coloring and discoloration in environmental conditions (Baek, *et al.*, 2017).

The demand for thin and flexible displays (including foldable and stretchable display) is increasing as interest in small and diverse designs grows (Rajoriya, *et al.*, 2013). Therefore, the display is being studied to realize a new form factor that is wearable (Colley, *et al.*, 2020, Kim, *et al.*, 2017, Luzhnica, *et al.*, 2018) and flexible (foldable, stretchable, and rollable) for human use. Flexible displays can be distinguished by their intended use and function (Paine, *et al.*, 2005). Recently, significant progress has been made in achieving active-matrix organic light-emitting diodes with bendable and rollable displays (An, *et al.*, 2010, Jin, *et al.*, 2010, Kim, *et al.*, 2011). Perfect assembly remains challenging despite technological advances in flexible and stretchable electronic components such as flexible electrodes and OLEDs.

The structural and functional changes of flexible display bring challenges to OCA that protect vulnerable components such as the thin-film transistor, OLED, and thin-film encapsulation by stress dispersion and adjustment of a neutral plane. The foldable display is a united panel containing a variety of layers and substrates. For a flexible OLED display, it is desirable to have either an OCA that perfectly mechanically decouples the layers from each other in bending (i.e., a material with no modulus) to minimize strain on critical layers or to have an OCA that can tune the position of the neutral plane during the folding process (Campbell, *et al.*, 2017). Also, although the thickness of OCA is thinner than that of OCA for a rigid display for reducing strain caused by folding, strong adhesion, flexibility, and durability are required to withstand hundreds of thousands of bends. Several PSA properties are additionally required to create these flexible displays. Generally, OCA for flexible displays requires low shear modulus and T_g (Lee, *et al.*, 2019). The recovery and stress relaxation properties

of OCA are essential for flexible displays because a high recovery of PSA prevents it from deformation under repeated folding-unfolding conditions (Chen, *et al.*, 2000).

PSA is a viscoelastic polymer, and when a strain higher than the elastic range is applied, irreversible deformation occurs through plastic deformation. Therefore, PSA for flexible display should exhibit linear elastic behavior in the applied strain range of the device bending and excellent recovery performance when the external force is removed. Traditional acrylic PSAs are rigid and not reversible when stretched (Class, *et al.*, 1984), so developing flexible and transparent PSAs remains a vital research task for implementing flexible displays. Research shows that PSA with high modulus has high cohesion and strain recovery performance (Back, *et al.*, 2019). However, simply increasing the modulus is not the solution. Physical properties studies for applying acrylic PSA to flexible displays were actively studied (Lee, *et al.*, 2017). As a result, the trade-off relationship between peel strength and strain recovery performance was confirmed. It is necessary to overcome the trade-off relationship between peel-strength and strain-recovery properties, and to conduct novel research to develop excellent OCAs for flexible displays.

1.3 Introduction of Heterogeneous Material

1.3.1. Methods for Property Control of PSA

Acrylic PSA is a polymer polymerized with acrylic monomers, and it is vital to optimize viscosity and elasticity. The relationship between viscoelasticity and adhesion has been studied. The range of storage modulus (G') and loss modulus (G'') is suggested as a viscoelastic window (Fang, *et al.*, 2017, Gdalin, *et al.*, 2011, Satas, 1989, Tse, 1989, Tse, *et al.*, 1996). The rheological property of PSA can be controlled by controlling the monomer composition in consideration of its characteristics and compatibility. Acrylic PSA is synthesized by selecting several acrylic monomers, and they can be classified into alkyl (meth)acrylate and functional (meth)acrylate (Benedek, 2020). Also, the alkyl (meth)acrylate is divided into monomers with a low T_g and a high T_g . The acrylic monomer of low T_g has a linear carbon chain that consists of 4~17 atoms, and the monomer of high T_g has a short linear chain (1~3 carbon atoms) or bulky chemical structure such as a cyclic hydrocarbon or aromatic ring. The functional monomer has a hydrophilic functional group, such as a carboxyl group and hydroxyl group, and this gives an acrylic polymer reaction site for crosslinking and hydrophilicity to enhance adhesion and cohesion strength. The low T_g monomers are the main component of acrylic PSA, and the high T_g monomers and the functional monomers are added to adjust the characteristics of acrylic PSA. A typical acrylic PSA consists of 50~90% of the low T_g monomer, 10~40% of the high T_g monomer, and 2~20% of the functional monomer (Li, *et al.*, 2001, Satas, 1989).

In the curing process, the gel fraction, M_n , and M_c can be adjusted by changing the content of the photoinitiator and curing agent (Lee, *et al.*, 2017). As the number of functional groups of the curing agent increases, the curing

degree increases, and the modulus of the material increases. Changing the curing energy source (UV, thermal) and curing environment also affects physical properties (Decker, 1998). All these traditional physical property control methods are homogenous control that changes the physical properties of the entire material. Due to the trade-off relationship of adhesive material properties, these methods have chronic limitations in manufacturing PSA for flexible displays.

1.3.2. Elastic Property of Heterogeneous Material

Bridging microscale properties of materials with their effective mechanical behavior at the overall scope is a significant challenge in both pure and applied science fields (Xia, *et al.*, 2012), as a new attempt to overcome the limitations of homogenous materials. Many research efforts are being conducted to study the effective properties of heterogeneous systems. Composite materials, structures, and metamaterials can achieve extraordinarily effective properties, e. g., negative Poisson's ratio (Rothenburg, *et al.*, 1991) or stiffness greater than diamond (Jaglinski, *et al.*, 2007), and elegant homogenization techniques have been developed to link micro- to overall scale in elastic settings efficiently (Milton, 2002, Nemat-Nasser, *et al.*, 2013, Sanchez-Palencia, *et al.*, 1987).

The complex microstructure and various forming constituents of heterogeneous materials have long posed difficulties in studying their effective mechanical properties. Researchers have tried to understand the interaction formula of effective mechanical properties of heterogeneous systems, such as elastic modulus and thermal conductivity, based on analytical approaches (Budiansky, 1965, Garboczi, *et al.*, 1995, Hashin, 1960, Hori, *et al.*, 1975). Since the 1960s, many studies have been conducted to predict and apply the physical properties of hetero materials (Christensen, 1968, Christensen, 1969,

Hashin, *et al.*, 1962, Watt, *et al.*, 1976), and the elastic properties of nonlinear composites are especially introduced. In 1963, Hill (Hill, 1963), Hashin (Hashin, 1965), Walpole (Walpole, 1966, Walpole, 1966), etc., arranged the modulus relational expression of homogenous materials as the most straightforward approach using average stress and strain through the Voigt and Reuss bounds approach. Voigt average arises by considering the strain to be uniform throughout the composite. The Reuss average assumes equal stress throughout the aggregate. The two generalized components are expressed in the equation below for a composite of two isotropic phases.

$$M_R^* = \left(\sum_{i=1}^n \frac{v_i}{M_i} \right)^{-1} \leq M^* \leq \sum_{i=1}^n v_i M_i = M_v^*$$

M_i is the modulus of the i th phase, M^* is the actual modulus of the composite, v_i is the volume fraction of phase i , and the subscripts R and v denote the Reuss and Voigt averages, respectively. Frequently used because of its ease of computation, this equation verifies that M_v^* and M_R^* are indeed bounding on M^* , which means that optimization of the actual modulus is possible by controlling the volume fraction and local modulus of the heterogenous component.

The widely used Voigt and Reuss average can be a poor approximation for both two-phase composites and polycrystals, Hashin-Shtrikman bounds were recommended. Hashin and Shtrikman (Hashin, *et al.*, 1961, Hashin and Shtrikman, 1962) derived new variational principles that led to tighter bounds for isotropic composites than the Voigt and Reuss averages. For the typical case of a two-phase aggregated, the bulk modulus K can be written as (μ is shear modulus)

$$K_1^* = K_1 + \frac{v_2}{(K_2 - K_1)^{-1} + v_1(K_1 + \frac{1}{3}\mu_1)^{-1}}$$

Most recently, studies have been attempted to elaborately predict the effective properties of homogenous materials and apply them realistically through various modeling and deep learning by developing basic research on the elastic properties of these homogenous materials (Cheng, *et al.*, 2019, Li, *et al.*, 2019, Lilliu, *et al.*, 1999, Ni, *et al.*, 2007).

1.3.3. Adhesion Property of Heterogenous Material

It is established in the literature that elastic stiffness heterogeneities can significantly enhance the force required to peel a tape without changing the properties of the interface (He, 1989). The peeling of a stiff plate from a compliant substrate can lead to oscillations in the peeling moment in the presence of heterogeneities (Ghatak, 2010). Heterogeneities of fracture energy in 3D brittle materials have been shown to lead to similar instabilities, producing the so-called crackling noise (Bonamy, *et al.*, 2008, Måløy, *et al.*, 2001, Sethna, *et al.*, 2001). This effect considerably increases the whole scope fracture energy of brittle heterogeneous materials (Ponson, 2009, Roux, *et al.*, 2008). The modeling of heterogeneous materials, distinguished from homogenous materials, is represented as follows. The so-called Rivlin model (Rivlin, *et al.*, 1997) for the homogeneous model leads to the expression of the peeling force per unit width (F)

$$F_{hom} = \frac{G_c}{1 - \cos \theta_p}$$

This behavior is independent of the elastic properties of the material. On the contrary, the stored elastic energy varies rapidly for heterogeneous elastic properties as the peeling front crosses from a soft to a hard region. The heterogeneous materials are modeled by an inextensible heterogeneous Euler-Bernoulli beam, and its geometry as peeling proceeds is described with the angle $\theta(s)$, which the tangent to the film at a distance s from the peeling front makes with the horizontal plane of the substrate. The governing equation for heterogeneous material is (Antman, 2005, Lurie, 2010)

$$\frac{d}{ds} \left(D(s) \frac{d\theta}{ds} \right) = bF \sin[\theta_p - \theta(s)]$$

Most of the heterogenous system studies are limited to brittle adhesives. Studies on improving adhesive properties for PSA are introduced here. S. Xia (Avellar, *et al.*, 2018) show how variations of elastic or adhesive properties can significantly affect the effective peeling behavior of the adhesive at the macroscale. They uncovered the mechanism: Imposing elastic stiffness heterogeneity in the film causes force fluctuations during peeling, increasing peel strength. The system's resistance can be tuned by effectively arranging areas of high adhesion. In a structure with a mixture of two sites with different adhesions, the motion in the forward direction where peeling occurs becomes unstable, resulting in a rapid energy release, improving the overall adhesive properties. As the modulus at the point of peeling increases (changing from a soft to a stiff region), the pulling force is dissipated in the bending of the adhesive. This causes a dissipation of the pull force and an increase in the peel force. Conversely, a lower modulus at the peel point causes a sudden release of bending energy, which causes fluctuations in the peel graph. This absorption and release of bending energy causes the adhesive properties to rise (Xia, *et al.*,

2012). Figure 1-1 shows the enhancement ratio for various levels of heterogeneity.

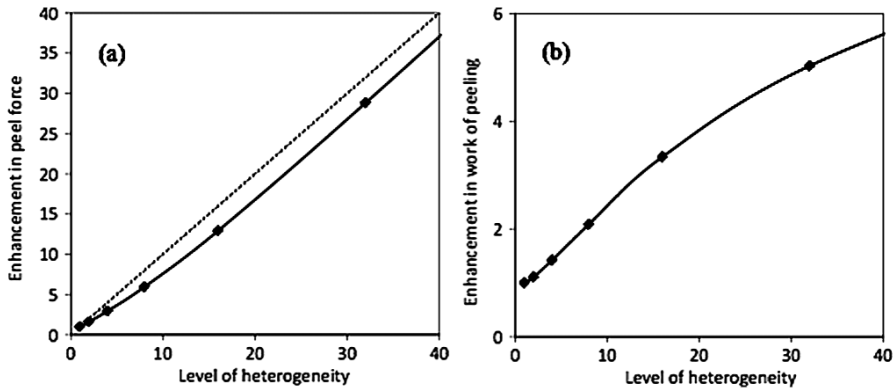


Figure 1-1. Enhancement in peel force (ratio of peel force, F_{het}/F_{hom}) for various levels of heterogeneity (ratio of bending rigidity, D_s/D_c). (Xia, *et al.*, 2013).

In addition, Avellar *et al.* (Avellar, *et al.*, 2018) also proved through theory and experimented that the apparent improvement in the peeling force of the adhesive tape imparted with non-uniformity in elastic stiffness was caused by the change in elastic bending energy. That is, fluctuations in small components of the system's overall energy can have significant macroscopic consequences (Xia, *et al.*, 2013).

1.3.4. Artificial Method of Heterogeneity

Industrially, the most widely used material patterning technique is lithography. The origin of the word lithography refers to lithography, and in modern industry, it refers to the printing technique of patterning a substrate using an energy source. Lithography is performed by selectively irradiating

energy using a mask, photo, x-ray, or electron beam or by applying a microscopic energy source (Thompson, 1983). Various sophisticated pattern shapes can be controlled quickly and intuitively using an artificial method called selective energy irradiation. Such delicate patterning is essential for applications such as semiconductor wafers (Levinson, 2005).

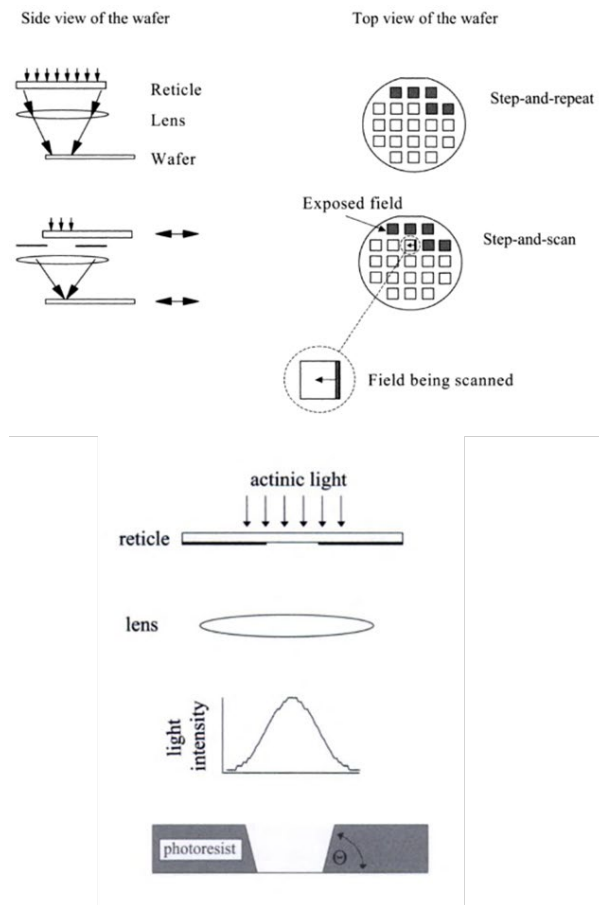


Figure 1-2. Step-and-repeat and step-and-scan configurations and light intensity of photo-masked light (Levinson, 2005).

Through selective energy irradiation, patterning with different physical properties of each part can be performed, and patterns with concavities and convexities can be manufactured through positive or negative resist developing, etching, and stripping processes. (Figure 1-3). Such lithography enables microfabrication that machines cannot physically impart and is essential to manufacturing micro-integrated circuits whose intensiveness is far superior to that of traditional materials (Levinson, 2005, Moreau, 2012).

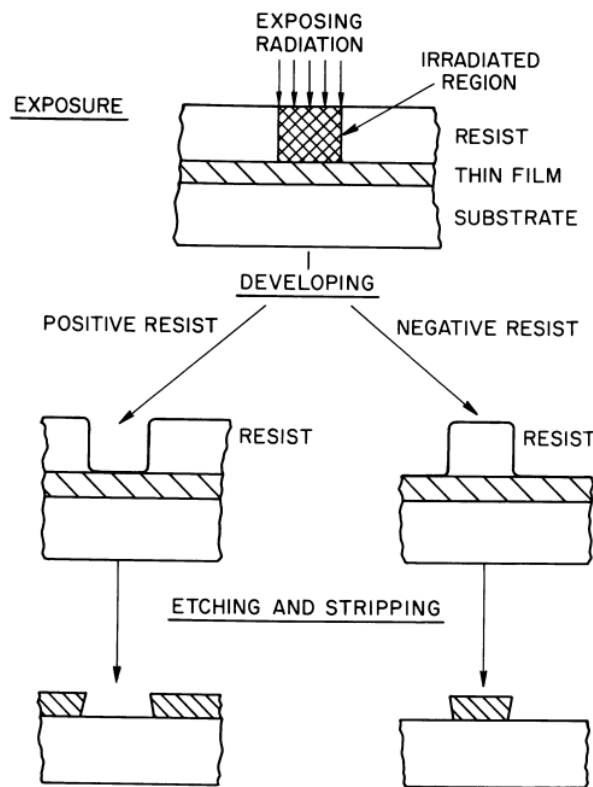


Figure 1-3. The schematic diagram showing the formation of a polymeric relief image using lithography (Levinson, 2005, Moreau, 2012).

1.3.5. Spontaneous Method of Heterogeneity

Unlike the artificial imparting process (Williams, *et al.*, 2002), which requires some energy, Spontaneous pattern formation is found in nature, from molecular assembly patterns (Barth, *et al.*, 2005, Pawin, *et al.*, 2006, Whitesides, *et al.*, 1991) and microscopic cell aggregation patterns to tissue formation (Qi, *et al.*, 2001, Shyer, *et al.*, 2017) to the skin patterns of organisms such as zebras on a macro scale. (Blagodatski, *et al.*, 2015, Kondo, *et al.*, 2010, Othmer, *et al.*, 2009) Besides biological patterns, inanimate phenomena such as the aggregation of colloidal particles (Chen, *et al.*, 2011, Malescio, *et al.*, 2003) and fluids (Bowman, *et al.*, 1998, Peng, *et al.*, 2015, Vandenbrouck, *et al.*, 1999) also exhibit spontaneous patterns. The essence of spontaneous pattern formation is the dynamic transformation of a system under perturbations to shape spatial regularities continuously. The whole process is directed toward reducing the free energy of the system. (Malescio and Pellicane, 2003, Samid-Merzel, *et al.*, 1998) Many Studies using molecular electron dopant (Ichimiya, *et al.*, 2018), transforming UV-curable emulsion (Inaba, *et al.*, 2022), and self-assembly of block copolymer (Kraus, *et al.*, 1976, Mai, *et al.*, 2012) have been attempted for this spontaneous patterning method.

1.4 Introduction of Polymerization-Induced Microphase Separation.

1.4.1 Micro phase Separation and Flory-Huggins Parameter

Micro phase separation is a phenomenon that occurs frequently in block copolymers, reflecting a delicate free-energy minimization. Block polymers are hybrid macromolecules consisting of chemically distinct polymer segments joined by covalent bonds. The covalent junction prevents the constituting blocks from separating apart even under immiscible conditions. (Bates, *et al.*, 1999) For example, A-b-B diblock polymers prefer to populate at the interface

of A- and B-selective media and behave as interfacial stabilizers by reducing interfacial tension (Shen, *et al.*, 1999, Zhang, *et al.*, 1996). In an A-selective solvent, the diblock copolymers self-assemble into micelles by separating the B block (Mai and Eisenberg, 2012). When the constituting blocks are immiscible in neat, they undergo microphase separation to form periodic nanostructures composed of discrete A and B microdomains. Their morphologies and length scales depend on the molar mass and the composition of block polymers, which can be adjusted in the synthesis step by employing controlled polymerization techniques (Bates, 1991, Blanazs, *et al.*, 2009, Thomas, *et al.*, 1988, Van Hest, *et al.*, 1995, Zhang, *et al.*, 1995). The size of most block polymer-based structures falls into the range of 1 ~ 1,000 nm. With synthetic freedom of block combination, block polymers offer a unique, versatile, and controlled route to polymeric nanomaterials and find a wide range of applications, including thermoplastic elastomers (Drobny, 2014), drug delivery vehicles (Cabral, *et al.*, 2018), lithographic templates (Kim, *et al.*, 2010), and membranes (Jackson, *et al.*, 2010, Phillip, *et al.*, 2010)

Macrophase separation (Figure 1-4, a) results when mixing thermodynamically incompatible linear homopolymers. The covalent bond between blocks in a diblock copolymer leads to microphase segregation (Figure 1-4, c). A mixed architecture of linear homopolymers and the corresponding diblock copolymer produces a surfactant-like stabilized intermediate-scale phase separation (Figure 1-4, b).

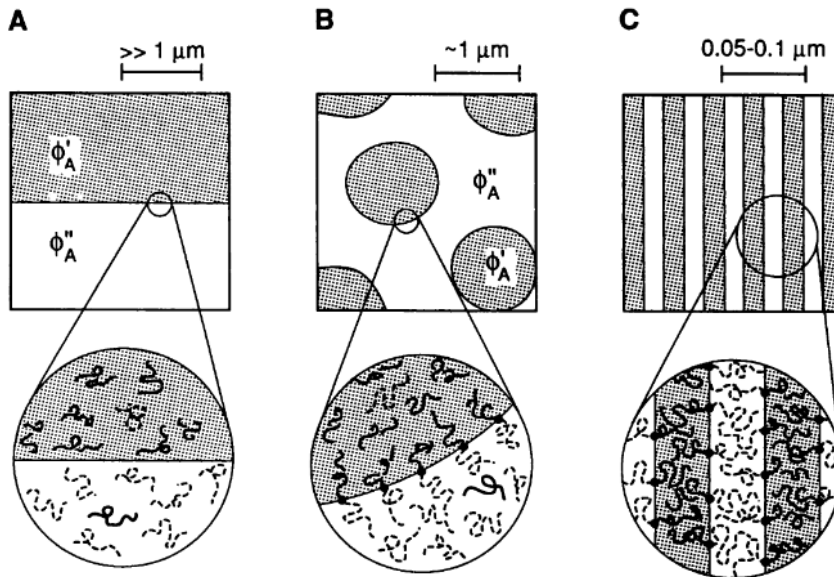


Figure 1-4. Representative polymer-polymer phase behaviors that can be realized with different molecular architectures (Bates, 1991).

Four factors control the behavior of the polymer-polymer phase at equilibrium: molecular architecture, choice of monomers, composition, and degree of polymerization. The degree of polymerization is the number of repeating units that make up the chain. The number of segments per polymer molecule is $N = \rho V X / M$, where ρ and M represent the polymer density and molecular weight, respectively, and X is Avogadro's number, V is the volume of the repeat unit. The energy of mixing is determined by the chosen pair of monomers, which determines both the sign and magnitude. This energy can be estimated using the Flory-Huggins segment-segment interaction parameter χ_{AB} , as detailed by De Gennes and Flory (De Gennes, 1979, Flory, 1953),

$$\chi_{AB} = \left(\frac{z}{k_B T} \right) \left[\epsilon_{AB} - \frac{1}{2} (\epsilon_{AA} + \epsilon_{BB}) \right]$$

where z is the number of neighbors of one repeating unit of polymers, k_B is Boltzmann constant, and ϵ_{AA} , ϵ_{BB} , and ϵ_{AB} are interaction energy between A-A, B-B, and A-B per unit molecules, respectively (Bates and Fredrickson, 1999). As χ is inversely proportional to temperature, cooling a disordered block polymer melt below the order-disorder transition temperature (T_{ODT}) can induce microphase separation for block polymers with fixed N .

1.4.2. Driving Force and Mechanism of in-situ Nano-Structuring

Microphase separation in conventional block copolymers has been achieved by controlled polymerization followed by a temperature-controlled annealing process (Khandpur, *et al.*, 1995). In contrast to these methods, a new method has been proposed to form nanostructures simultaneously with polymerization.

PIMS (Seo, *et al.*, 2012) is an in situ nanostructuring method first introduced in 2012, following the emergent of polymerization-induced phase separation (PIPS) (Lequieu, *et al.*, 2021), and polymerization-induced self-assembly (PISA) (Cao, *et al.*, 2021). Distinguished from PIPS (Yamanaka, *et al.*, 1989), where there is no covalent bonding between the growing polymer chain and the pre-existing polymer chain, and PISA (Penfold, *et al.*, 2019), which discusses micelle formation under solvent-dissolved conditions, PIMS is a method for preparing microphase separated materials in the solid phase through chain extension and crosslinking of pre-existing chains under non-solvent conditions.

PIMS have advantage of neat polymerization in the absence of a solvent converting the whole polymerization mixture into a solid monolith. PIMS provides a more straightforward route to nanostructured block polymer

thermosets through the in situ crosslink process. Recent developments have taken advantage of the compatibility of the PIMS process with various polymerization and processing techniques, such as emulsion polymerization (Park, *et al.*, 2018, Peterson, *et al.*, 2022) and 3D printing (Melodia, *et al.*, 2023), and have demonstrated the synthesis of more complex and hierarchically structured materials over multiple length scales (Jeon, *et al.*, 2018).

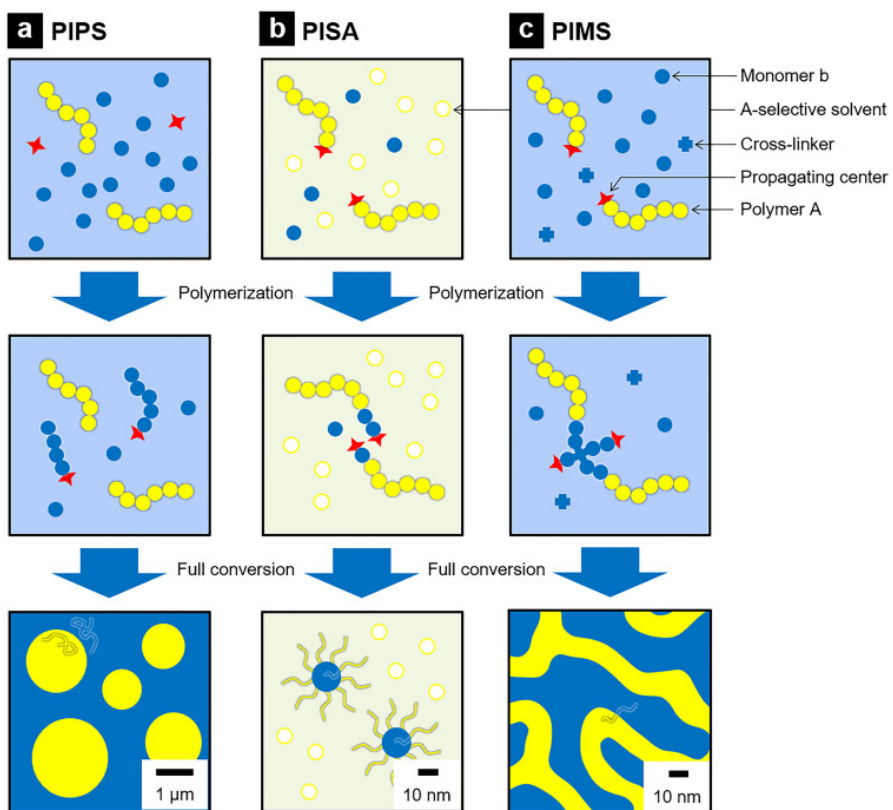


Figure 1-5. Schematic illustration of a) PIPS, b) PISA, and c) PIMS processes. (Oh, *et al.*, 2023)

PIMS does not require solvents, unlike PISA. Polymerization proceeds in a neat polymerization mixture typically containing a crosslinker as a comonomer. The mixture is converted into a monolithic solid with a disordered bicontinuous morphology composed of A and B microdomains at the nanometer length scale (Oh, *et al.*, 2023). Therefore, PIMS is the most advantageous for applying adhesive materials for displays, where nonsolvent UV curing types are required in manufacturing.

Increasing N drives the system to order, not changes in temperature or pressure, as in the pre-synthesized block polymers (Motokawa, *et al.*, 2007). The initial polymerization mixture can be considered a solution of polymer A in monomer b. Polymerization produces A-b-B diblock copolymer by consuming monomer b, continuously increasing N , f_B , and the block polymer concentration (ϕ) in the solution as a function of conversion. Assuming χ_{AB} , χ_{Ab} , and χ_{Bb} do not vary upon b polymerization, the polymerizing solution can be described by a three-dimensional phase diagram composed of f , N , and ϕ axes. Such a phase diagram is illustrated in Figure 1-6 (Huang, *et al.*, 1998). Roughly, both increases in N and ϕ facilitate microphase separation, while changes in f and ϕ allow the solution to move across various phases during polymerization (Lodge, *et al.*, 2002).

1.4.3. Factors controlling Polymerization-Induced Microphase Separation

The main factors regulating PIMS structure include crosslinker, degree of polymerization, and interaction parameters. The crosslinker copolymerization provides a means to fix the target morphology spontaneously during the chain extension process. Schulze *et al.* investigated the effect of crosslinker loading on the PLA-CTA/styrene/DVB system. They showed that the crosslinker content could determine the moment of structure arrest, spanning from disorder

to order (Schulze, *et al.*, 2017). High crosslinking density also can add additional stability to the PIMS materials.

Like conventional block polymer systems, N_c can control the domain size of PIMS materials. By varying the molar mass of macro-CTA while maintaining the weight fraction of the composition in the PIMS polymerization mixture, it is possible to control the domain size. (Seo and Hillmyer, 2012) High χ between the macro-CTA and the growing block allows the system to enter the ordered phase early and develop a narrow interface (McIntosh, *et al.*, 2015). However, preparing a homogeneous polymerization mixture would not be possible if χ is too high because the monomer would be highly incompatible with the macro-CTA.

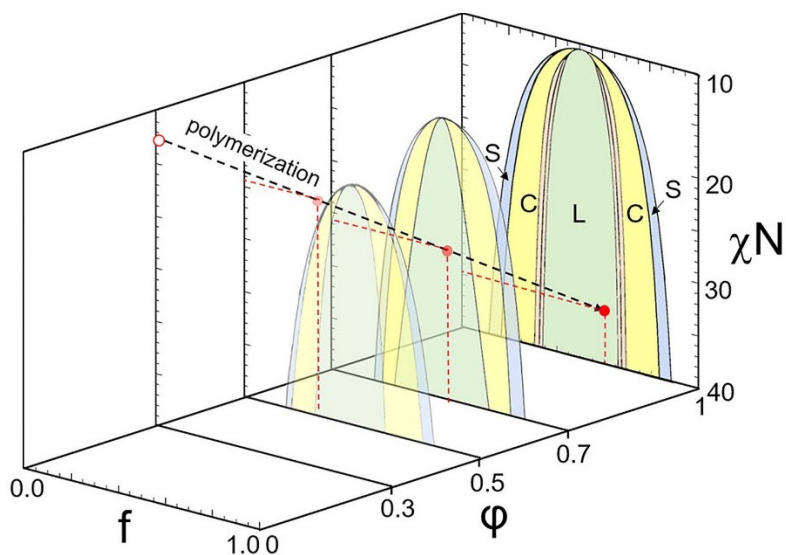


Figure 1-6. Imaginary 3D phase diagram illustrating the PIMS process starting with a polymerization mixture of polymer A in monomer b (Huang and Lodge, 1998).

2. Literature review

2.1. Mechanism of Improving Physical Properties of Heterogenous PSA

Xia *et al.* (Xia, *et al.*, 2013) studied the adhesion of thin films on rigid substrates in the presence of spatial heterogeneities. Although adhesion in homogeneous systems is relatively well understood, understanding of adhesion in heterogeneous systems is lacking. They study thin adhesive tapes with heterogeneities in elastic stiffness and show that these heterogeneities profoundly affect adhesion, increasing the effective force required to peel the film without changing the adhesive interface. The research arranged the energy (F) required to peel off the heterogeneous film as follows. (D is the distribution of bending rigidity, χ is the length fraction, θ_p is the peel angle under a peel force, G is constant.)

$$F = \left(\sum_{m=1}^M \frac{\chi^{(m)}}{D^{(m)}} \right) \frac{D_1 G}{1 - \cos(\theta_p)}$$

Especially for the case of the heterogeneous film comprising two segments ($N=2$) with different bending rigidities, D_1 and D_2 , the equation is arranged as below.

$$F_{Het} = \frac{D_1 G}{D_2 + (D_2 - D_1) \cos(\theta_1 - \theta_p) - \cos(\theta_p)}$$

The peeling force depends on θ_1 which in turn depends on the position s_1

of the interface. The force required to peel the tape depends on the maximum value of the peeling force. The maximum peeling force occurs when $D_1 > D_2$, i.e., when the bonded surface of the film has higher bending rigidity and for $\theta_1 = 0$:

$$F_{Het}^{2seg} = \frac{D_1 G}{D_2(1 - \cos(\theta_p))} = \frac{D_1}{D_2} F_{Hom}$$

Regardless of the peel angle and intrinsic adhesion energy, the peel force of the two-segment film is superior to that of the homogeneous film, and the enhancement ratio is D_1/D_2 . In other words, PSA properties can also be controlled by designing each segment's bending stiffness ratio.

2.2. Macro Scale Heterogeneous PSA by Photo Lithography

Heterogeneous patterns of macro scale can be given through selective irradiation of energy sources. Research on heterogeneous PSA through this lithography method was preceded by UV-curing patterned PSA manufactured through selective crosslinking and a UV curing system. UV curing refers to producing a semi-solid PSA sheet through a chain of radical propagation and curing reactions in which a photoinitiator is radically initiated by irradiation with UV light (Czech, *et al.*, 2012). At this time, the physical properties of the final cured PSA can appear very diverse depending on the dose and intensity of the irradiated UV (Lee, *et al.*, 2000).

Due to the characteristics of UV curing, local differential irradiation is possible using a photomask, etc., so it is possible to perform patterning in which the modulus of each part of the PSA material is cured differently. Yoo *et al.*

(Yoo, *et al.*, 2021) conducted a study to manufacture micro heterogenous PSA with a differential adhesiveness diversity using Patterned PSA using a wide variety of UV photolithography and use it for the production of silver nanowire electrodes (Figure 1-7). They performed patterning by irradiating a mercury lamp (HBO 350W/S, OSRAM) on a UV-curable adhesive with a photomask for 55 s. This study suggests that it is possible to fabricate sophisticated UV-patterned PSAs by utilizing a photomask despite the spread of light.

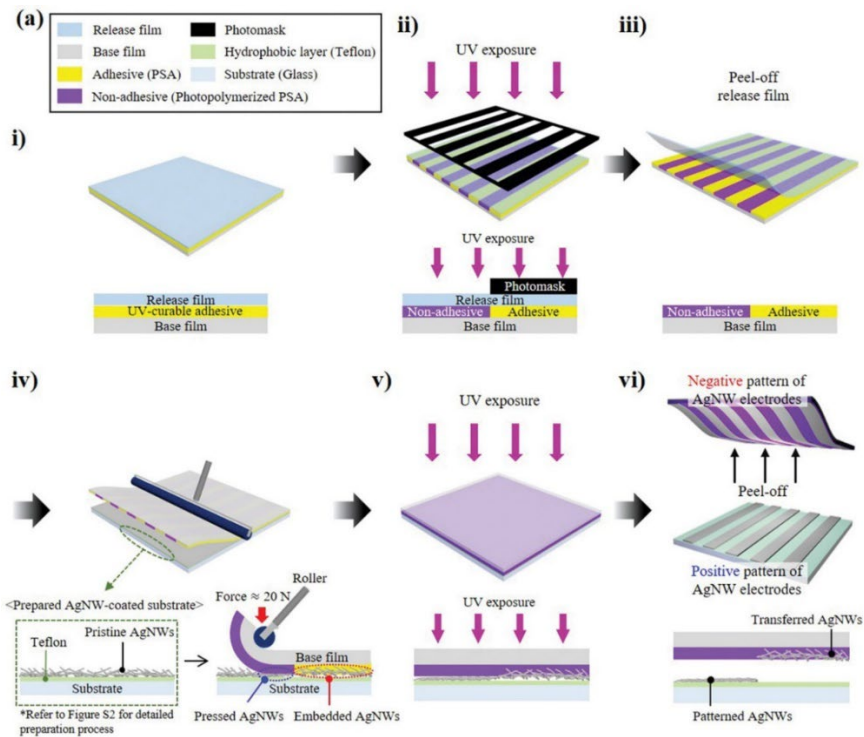


Figure 1-7. Fabrication of UV patterned PSA (Yoo, *et al.*, 2021).

Back *et al.* (Back, *et al.*, 2019) designed Acrylic PSA containing both high and low-cured regions during UV curing. This research determined that a UV-

patterned PSA with both high and low crosslinking densities in a single layer enables the optimization of both recovery and relaxation. By introducing the UV-patterned PSA, the elasticity and recovery largely deteriorated, but the stress relaxation was significantly improved compared to that of the nonpatterned PSA, and this effect was enhanced with increases in the applied strain. The recovery and relaxation were well-optimized, with values above 71% only at 300% strain. The recovery and relaxation of PSA had a positive and negative correlation with the storage modulus (Figure 1-9).

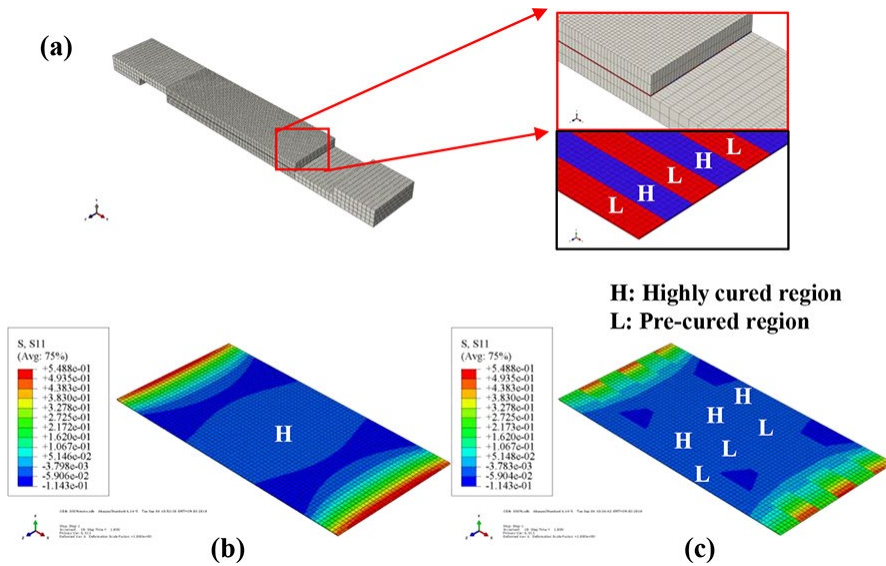


Figure 1-8. UV patterned PSA which contain both high and low cured region (Back, *et al.*, 2019).

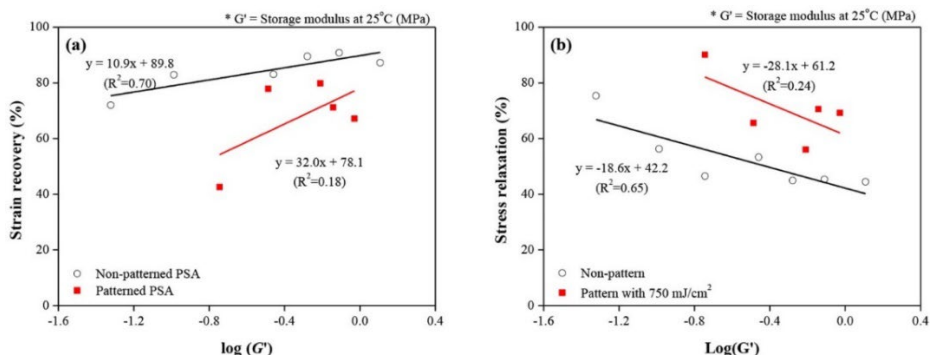


Figure 1-9. Relationship of storage modulus and flexibility of UV patterned and non-patterned PSA (Back, *et al.*, 2019).

2.3. Nano Scale Heterogeneous PSA by in-situ Nano-Structuring

In the studies that made heterogeneous PSA using spontaneous pattern formation, the method using microphase separation of the block copolymer was mainly used. Hussnain Sajjad *et al.* (Sajjad, *et al.*, 2020) used biorenewable chemicals lauryl acrylate and triacetic acid lactone (TAL) to produce PSA by polymerizing an ABA triblock copolymer with a butyl acrylate block. Lauryl acrylate, readily derived from vegetable oils, was polymerized via a reversible addition–fragmentation chain-transfer (RAFT) process to yield high-molecular weight telechelic polymers. The synthesis of triblock copolymers was accomplished by subsequent chain extension with TAL, which is available from carbohydrates via the action of genetically modified yeast. The resulting triblock copolymers exhibited excellent adhesion, with tunable peel forces up to 8 N/cm when a rosin ester-based tackifier was used. Tack forces up to 7 N/cm and no shear failure up to 100 h demonstrate the competitive performance of the potentially sustainable adhesives with a commercial commodity product.

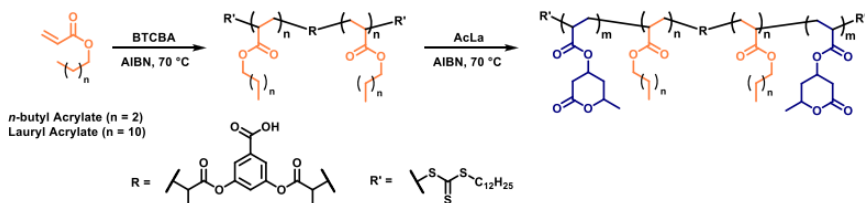


Figure 1-10. Synthesis of acrylic block PSA via RAFT polymerization (Sajjad, *et al.*, 2020).

This study produced heterogeneous PSA using block copolymer and showed that it can exhibit high physical properties such as improved adhesion through low T_g block and shear property and adhesive failure mode through high T_g block. It suggests that the overall physical properties can be improved through the synergistic effect of each phase of the heterogeneous material. However, this study had the disadvantage of requiring additives such as a tackifier to develop adhesiveness since the acrylic block copolymer itself did not express adhesiveness.

Bobrin *et al.* (Bobrin, *et al.*, 2022) designed a novel approach for fabricating materials with controlled nanoscale morphologies. This process exploits reversible deactivation radical polymerization to control the in-situ-PIMS of 3D printing resins, which provides materials with complex architectures controllable from the macro- to the nanoscale, resulting in the preparation of materials with enhanced mechanical properties.

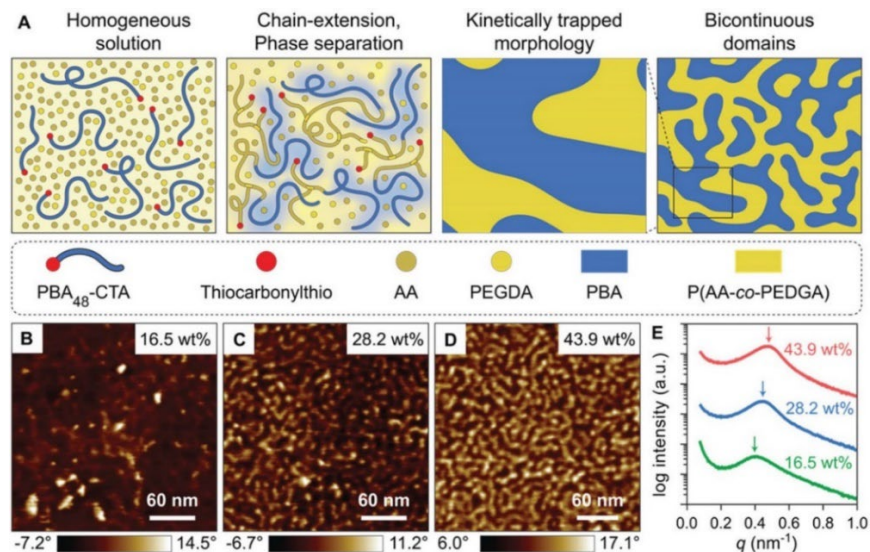


Figure 1-11. Polymerization-induced microphase separation (PIMS) mechanism and resulting materials. a) PIMS process. b - d) AFM phase images in tapping mode. e) Small-angle x-ray scattering (SAXS) profiles of the materials (Bobrin, *et al.*, 2022).

This study suggests that elongation properties and toughness can be improved through microphase separation. In addition, it is significant that the microphase separation morphology in which two microphases of high modulus and low modulus coexist was directly confirmed through AFM. They proved through AFM that the size of the soft domain increases as the M_n of the PBA block constituting the soft domain in the material increases, and the elongation property and toughness are also improved. However, in this study, as a material for 3D printing, acrylic monomers that exhibit adhesive strength were used, but it isn't easy to expect adhesive performance because AA accounts for significant content. Therefore, referring to this study, in this paper, we intend to conduct a study on PSA for flexible displays with both stretchability and durability.

3. Objectives

OCA for flexible displays is a material focused on securing: 1. the adhesive performance, 2. excellent stretching properties that do not break when stretched, and 3. elasticity that returns to its original shape. To date, many attempts have been made to reduce the modulus of the material to fulfill the above conditions. However, materials with low modulus are prone to plastic deformation, have weak elasticity to return to their original shape, and have limited adhesion performance because the cohesive force of PSA is reduced. Therefore, to overcome the obstacle, an acrylic PSA with a molecular structure similar to polyurethane, a material with both elongation and recovery regions exhibiting excellent elasticity, was studied.

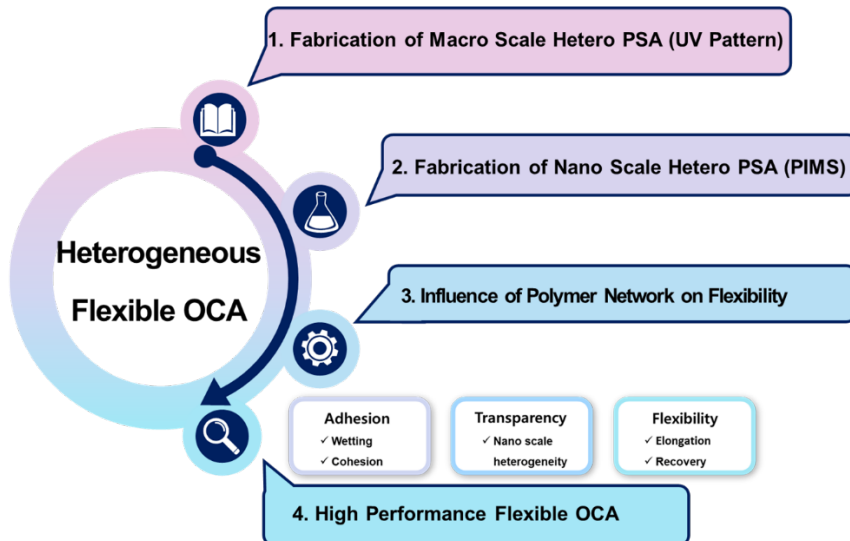


Figure 1-12. Comprehensive objectives of this study.

3.1. Understanding the Properties of Heterogeneous PSAs

It is known that heterogeneous materials, meaning that the composition of the polymer network is not uniform, can exhibit synergistic advantages over homogeneous materials by taking advantage of the strengths of each domain. In particular, from the perspective of stretching and recovery, a flexible part composed of a soft chain, when stretched by holding the two ends of the material, causes a conformational change in the polymer and stretches smoothly. Conformational change can be directly reflected as an entropic force and expressed as an elastic force that returns to the original molecular shape when the external force is removed. The hard (high modulus) domains do not move quickly and act as a skeleton to maintain the material's original structure. Since the flexible chains respond first to external forces, the hard domains do not deform and act as a skeleton to prevent plastic deformation, resulting in much better elongation and recovery performance than classical materials. The most frequently attempted method of heterogenizing PSA polymers is through photolithography. In this study, we aimed to prepare heterogeneous PSA using photolithography and check the possibility of improving the properties of heterogeneous PSA.

3.2. Fabrication of Novel Nano Structured Heterogeneous PSA

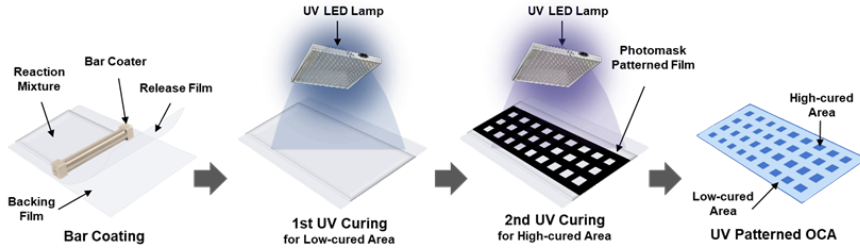
Previous studies have utilized block copolymers to study PSA with small nanoscale heterogeneous structures. Block copolymers are a representative material that can induce heterogeneous structures by spontaneous self-assembly due to differences in the compatibility of each block. However, there is a limitation that a solvent must be used to polymerize block copolymers. Non-solvent acrylic adhesives are highly utilized and preferred industrially due to their lower fire hazard, energy consumption, and facility space than solvent-

based adhesives. Therefore, in this study, PIMS, which can induce heterogeneous structures from the bulk state, was selected instead of block copolymers that require solvents. In summary, this study aims to confirm the possibility of improving the properties of heterogeneous PSA and further develop PSA for flexible displays with excellent stretching and recovery performance by utilizing PIMS.

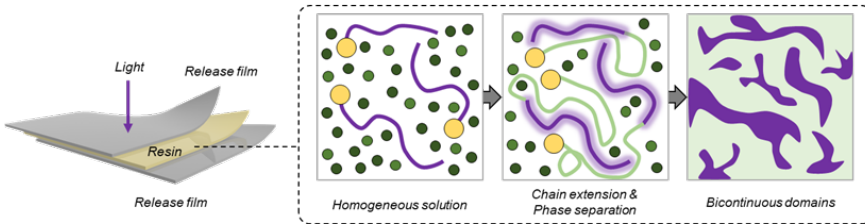
3.3. Influence of Polymer Network on Elasticity

In addition to fabricating hetero-PSAs that exhibit excellent elasticity, we explore the molecular structures responsible for the elasticity of elastomers. This fundamental understanding will significantly benefit future material design research. The length of the network chain ends was varied by varying the PBA chain length. We will examine the changes in crosslinking and entanglement and the resulting morphological, rheological, and physical properties.

1. Fabrication of Macro Scale Hetero PSA (UV Pattern PSA)



2. Fabrication of Nano Scale Hetero PSA (PIMS PSA)



3. Influence of Polymer Network on Elasticity (Macro CTA M_w Variation)

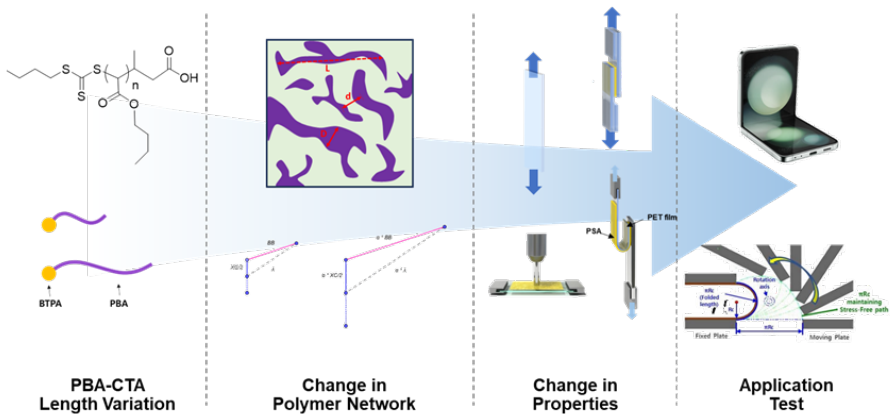


Figure 1-13. Comprehensive experimental flow of this study.

Chapter 2

*Macro Scale Heterogeneous PSA
using UV Patterning*

1. Introduction

PSA refers to a polymeric material that can be adhered to various substrates with little pressure. They are helpful in everyday life and a wide range of industrial applications and are nowadays the building blocks of advanced technologies in electrical and electronic materials (Creton, 2003).

The properties of PSA, such as adhesion force, tensile strength, elongation at break, and recovery properties, change according to the polymer design. The fundamental way to control PSA properties is to adjust the component formulation, such as changing the type and content of the monomer or adjusting the number of functional groups or content of the crosslinker. By adjusting the formulation, the T_g of the polymer material can be designed using the Fox equation, and the crosslinking density and modulus can be controlled by adjusting the crosslinker. For materials utilizing UV curing systems, adjusting the type and content of photoinitiators and the intensity and dose of the UV light source can also be used. In this study, we found that irradiating light with a higher intensity increased the initiation rate of the initiator, resulting in a higher number of propagation chains and, consequently, a material composed of more and shorter polymers. Conversely, irradiating light with a lower intensity decreased the initiation rate of the initiator, resulting in a material composed of fewer but longer polymers. The longer the length of the polymer chains, the larger the network size, the higher the gel fraction, and the stronger the cohesive force, which is favorable for recovery, while the shorter the length of the polymer chains, the smaller the network size, the weaker the cohesive force and the more favorable for wetting, which tended to increase the peel strength value. However, improving the properties by adjusting the UV curing conditions has a limitation in that various properties are inversely proportional to each other, making it challenging to show all-round superior properties.

Therefore, in this study, in addition to checking the polymer structure and properties according to UV conditions, we introduced UV patterning technology to impart inhomogeneity to the PSA molecular structure to enable even improvement of properties.

This study was conducted to improve flexibility while maintaining adhesive performance and transparency by applying a curing density pattern to the PSA sheet by selectively irradiating ultraviolet (UV) light by using a photomask with a pattern in the UV curing system (Joo, *et al.*, 2007). PSA's flexibility was analyzed regarding strain recovery and stress relaxation because the recovery performance prevents plastic deformation, and the stress relaxation performance prevents delamination due to internal cracks. The preceding research shows the relation between dynamic mechanical analysis (DMA) storage modulus and recovery/relaxation properties (Back, *et al.*, 2020). Generally, the recovery property increases as the storage modulus increases, whereas the stress relaxation property is the opposite. The recovery property and relaxation property of the PSA are in an inverse relationship. The UV patterned OCA we designed contains high-cured regions and low-cured regions according to the photomask pattern, and each cured region reveals different property respectively. Additionally, the region having a high curing density formed an overall storage modulus to the PSA and maintained resistance to external stress around the crosslinking site, thereby exhibiting excellent recovery property. The low cured region had a synergistic effect of reducing the deformation rate of the high cured region and preventing plastic deformation by exhibiting a buffering effect, as the polymer chain easily slides and stretches as it deforms from the outside.

2. Experimental

2.1. Fundamental Study on UV Curing System for Acrylic PSA

2.1.1. Materials

2-ethylhexyl acrylate (2-EHA, 99.0% purity), isobornyl acrylate (IBA, 99.0% purity), acrylic acid (AA, 99.0% purity), methyl methacrylate (MMA, 99.0% purity), and 2-hydroxyethyl acrylate (2-HEA, 99.0% purity) were purchased from Samchun Pure Chemical (Republic of Korea). Additionally, 2-hydroxy-2-methylpropiophenone (Irgacure 1173) was purchased from BASF (Germany) and used as a photo radical initiator. Poly (ethylene glycol 200 dimethacrylate) (PEG200DMA, Sartomer SR210) was purchased from Sartomer (USA) and used as a crosslinking agent.

Table 2-1. Compositions of the raw materials used for the synthesis of pre-polymers.

| Resin Composition (wt%) | |
|--------------------------------|-----|
| 2-ethylhexyl acrylate | 64 |
| Isobornyl acrylate | 19 |
| Acrylic acid | 3 |
| Methyl methacrylate | 4 |
| 2-hydroxyethyl acrylate | 10 |
| Hydroxydimethyl acetophenone | 0.3 |

2.1.2. Synthesis of the Pre-polymer

The pre-polymer was synthesized from 2-ethylhexyl acrylate, acrylic acid, isobornyl acrylate, methyl methacrylate, and 2-hydroxyethyl acrylate via bulk radical polymerization (Jiang, *et al.*, 2017). Reaction mixtures were initiated with 0.3 wt% of hydroxydimethyl acetophenone (98 % purity, Shinyoung Rad. Chem., Republic of Korea). Polymerization was performed in a 500 mL four necked flask with a mechanical stirrer, N₂ inlet, thermometer, and a light-emitting diode (LED) UV spot cure. Stirring at 100 rpm was maintained at room temperature (23 °C). After 30 min of N₂ purging under constant stirring at 100 rpm, the monomer mixtures were exposed to a UV light (20 mW/cm²), increasing the temperature by 15 °C. The chemical reaction is shown in Figure 2-1. First, the carbon double bond of the acrylate groups of the monomers are broken by the radicals generated by light induced cleavage of hydroxydimethyl acetophenone. Acrylic groups containing radicals break through the double bonds in the acrylic groups of other neighboring monomers, and a continuous chain polymerization reaction proceeds (Allen, 1996). Because of steric effects and stability of the radical, methacrylates slowly participate in the polymerization reaction (Nason, *et al.*, 2005). The added monomers are randomly located in the prepolymer. AA and MMA are also consumed, but their proportion in the prepolymer is small because of the small amount of addition.

2.1.3. UV Curing Condition controlling Polymer Structure and Property

After N₂ purging for 1 h, PEG200DMA (1 phr) as a crosslinking agent and Irgacure 1173 (1 phr) as a photo radical initiator were added to each 58 mL container. The mixture was blended using a planetary centrifugal mixer ARE-310 (Thinky, Japan) at 600 rpm for 1 min. The acrylic PSA was coated with a thickness of 50 µm between the corona-treated polyethylene terephthalate (PET) film with a thickness of 75 µm and release film with a thickness of 50 µm, and

then UV-cured with a wavelength of 365 nm with several UV intensity levels and irradiation times using UV LED curing device (OnUV, Republic of Korea). The photoinitiators absorbed UV light energy and became radical species by the photocleavage reaction. Initiated radical species attack the monomers, crosslinking agent, and crosslinking group in pre-polymers, inducing free radical polymerization resulting in a crosslinked polymer network.

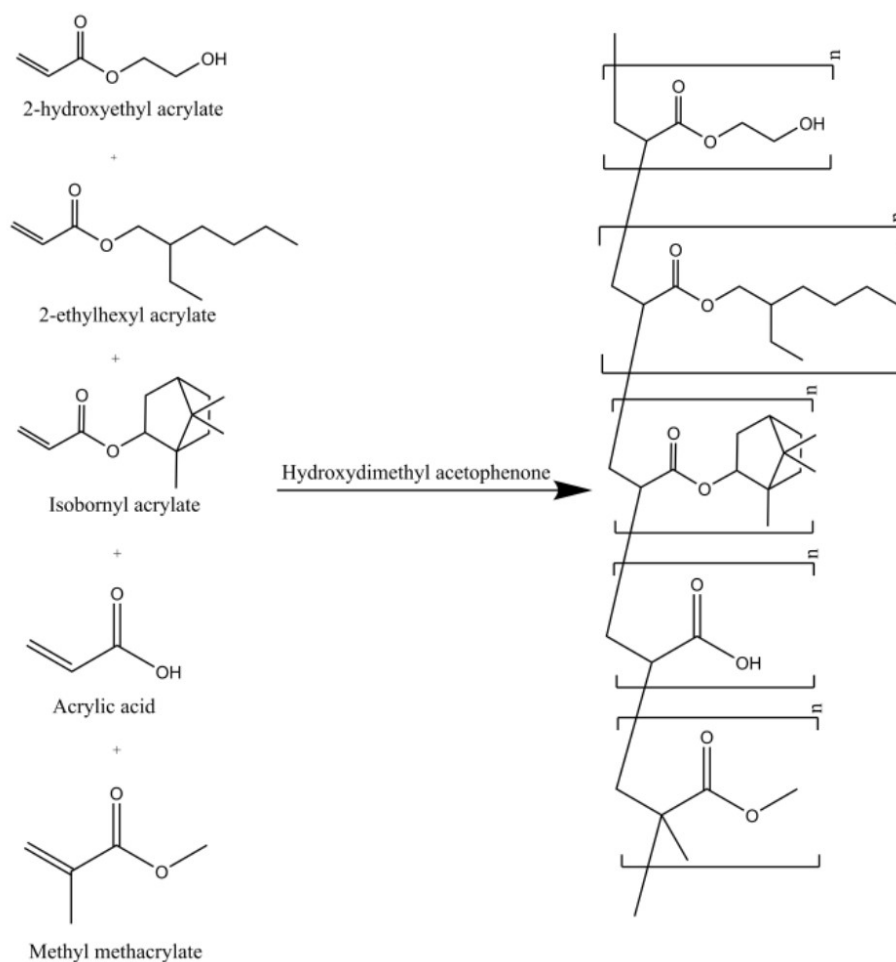


Figure 2-1. Synthesis of the OCA prepolymer.

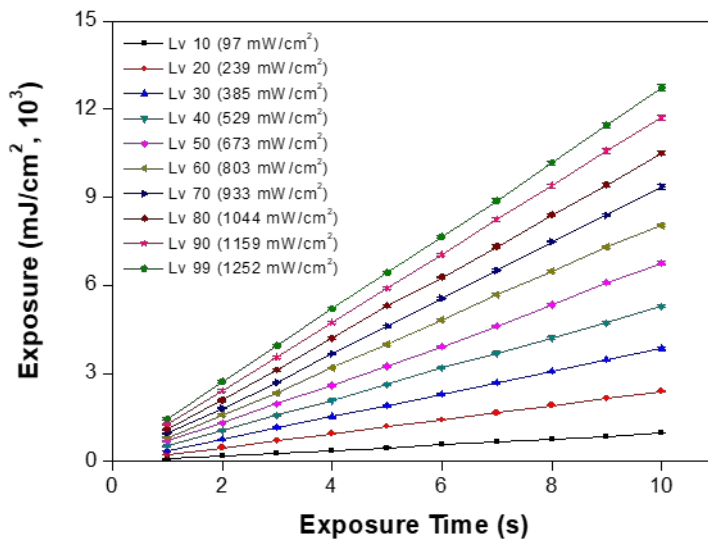
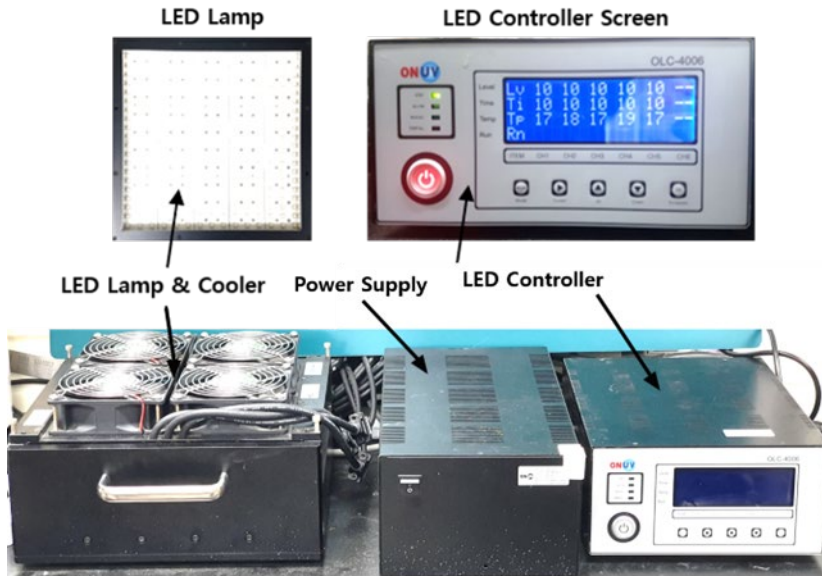


Figure 2-2. Appearance and structure of the UV LED curing device (Kim. *et al.*, 2021).

2.1.4. UV/UV Step Curing

UV-curable syrups were prepared by blending the pre-polymer with ethoxylated (3) trimethylolpropane triacrylate (EO3TMPTA, Sigma-Aldrich) and ethoxylated (9) trimethylolpropane triacrylate (EO9TMPTA, Sigma-Aldrich), at a ratio of 7:3. These are multifunctional acrylates that are commonly employed to evaluate blended binary systems.

A mixture of EO3TMPTA and EO9TMPTA was selected to decrease the UV curing rate during primary curing. They left unreacted monomers after primary curing consumed during secondary curing. Hydroxydimethyl acetophenone (Micure HP-8, Miwon Specialty Chemical, Republic of Korea) was used as the photo-initiator. The absorption ranges of this material are 265~280 nm and 320~335 nm.

PSA reaction mixtures was coated on corona-treated PET films (SKC Co. Ltd., Republic of Korea) at a thickness of 100 μm . In the primary curing steps, the coated resin was cured by passing under a black light UV-curing machine equipped with a low-pressure mercury UV lamp (20 mW/cm^2 , main wavelength 365 nm) for different durations. Light irradiance is inversely proportional to the distance of the UV lamp from the curing materials, which also changes the curing speed and behavior (Bennett, *et al.*, 2004). The UV lamp was placed 3 cm away from the coatings for primary cure. The UV irradiation dose for primary cure step was 0.3 J/cm^2 per 1 min. PSA coatings were cured for 2 ~ 5 min in the case of primary curing. The samples were cured at 0.6 ~ 1.5 J/cm^2 during the primary curing stage. Covalent bonds were formed in primary curing by suitable functional groups on the triacrylate binder molecule. Eventually, some polymer chains were crosslinked (Chattopadhyay, *et al.*, 2005).

In the secondary curing steps, the primary-cured film was passed under a conveyerized metal halide UV curing unit equipped with mercury UV light

(main wavelength of 365 nm, 154 mW/cm²). During secondary curing, the UV lamp was placed 15 cm away from the curing materials. The UV irradiation dose for secondary curing was fixed at 3 J/cm². During secondary cure step, the remained tri-acrylate molecules in the mixtures reacted with the site of the acrylate polymer to form a crosslink network. The process is shown in Figure 2-3.

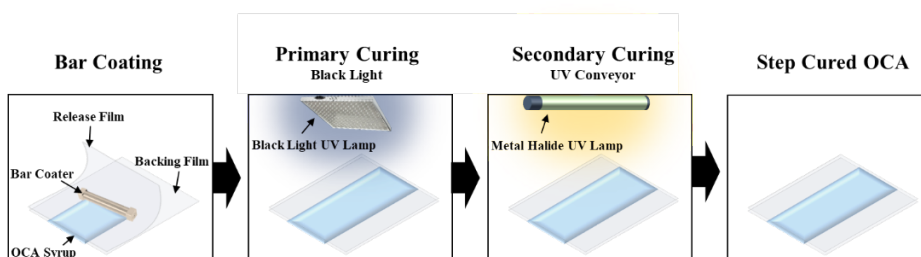


Figure 2-3. UV/UV step curing process for the acrylic PSA (Kim. *et al.*, 2019).

2.1.5. Characterization

Gel permeation chromatography

The molecular weights of acrylic PSA were measured using a YL9100 gel permeation chromatography (GPC) system (Young Lin Instruments, Republic of Korea) equipped with a YL9170 refractive index detector. GPC columns were eluted with tetrahydrofuran at 35 °C and a 1 mL/min flow rate. The sample was diluted with tetrahydrofuran to 0.5 percent concentration by weight. The number-average (M_n) and weight-average (M_w) molecular weights were calculated as 630,000 and 1,477,000, respectively, and the polydispersity index (M_w/M_n) thus equaled 2.34. The calibration curve from polymethylmethacrylate standards with molecular weight of 1660, 2580, 3480, 6780, 7800, 31600, 54500, 93300, 158000, 267000, 520000, 701000, 981000 was used for

calculation.

Gel Fraction

The gel fraction test is a convenient method for measuring the quantity of insoluble components, such as the fractions of crosslinked or network polymers. Gel fraction depends on the solubility parameter of the solvent. In this study, toluene was selected as the solvent. The gel content is a significant factor in terms of curing behavior. The gel fractions of the crosslinked adhesives were determined by soaking them in toluene at 25 °C for 24 h. The insoluble part was removed by filtration and dried at 60°C to a constant weight. The gel fraction was calculated using the equation below, where w_0 and w_1 are the weights of adhesive before and after filtration, respectively.

$$\text{Gel fraction (\%)} = \left(\frac{w_1}{w_0}\right) \times 100$$

Conversion measured by FT-IR

FT-IR analysis was carried out to determine the UV LED curing conversion of acrylic PSA. The spectra were obtained using an FT/IR-6100 (JASCO, Japan) equipped with an attenuated total reflectance (ATR) accessory composed of a diamond crystal. Spectra were collected from 4000 to 400 cm^{-1} 32 times at a resolution of 4 cm^{-1} . All spectra were corrected through CO₂ reduction, H₂O reduction, noise elimination, and baseline correction. The conversion of acrylic PSA was calculated by

$$\text{Conversion (\%)} = \frac{(A_{810})_0/(A_{1720})_0 - (A_{810})/(A_{1720})}{(A_{810})_0/(A_{1720})_0} \times 100 (\%)$$

where $(A_{810})_0$ and (A_{810}) are the intensity for 810 cm^{-1} (C=C bond) at the initial time and after curing, respectively, and $(A_{1720})_0$ and (A_{1720}) are the intensity for 1720 cm^{-1} (C=O bond) at the initial and after curing.

Real-time FT-IR

FT-IR spectroscopy followed Polymerization reactions in situ (Decker, *et al.*, 1990, Decker, 2002) by monitoring the decrease of the IR band characteristic of the reactive functional group upon UV exposure. The samples were simultaneously exposed to the UV rays, inducing polymerization, and to the infrared rays, analyzing the degree of polymerization, as shown in Figure 2-4, depicting the instrumental set-up. With the FT-IR spectrophotometer used (JASCO, Japan), up to 10 spectra can be taken per sec at a spectral resolution of 4 cm^{-1} , thus allowing high-speed polymerizations to be accurately followed in real time.

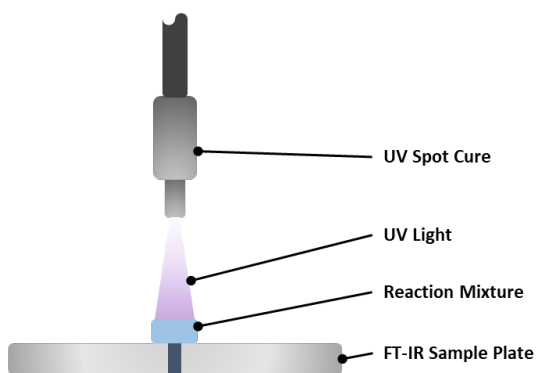


Figure 2-4. Instrumental set-up for real-time infrared spectroscopy analysis of ultrafast photopolymerizations.

Electron paramagnetic resonance

CW/Pulse EPR spectrometry (EMX plus, Bruker) was used to measure the acrylic resin's active radical concentration during the UV cure step. 0.1 M of Acrylic oligomer blends and 0.1 mM of photoinitiator were diluted in toluene. The stock solution was blended with spin trap agent, 5,5-dimethyl-1-pyrroline-n-oxide (DMPO, 0.36M), then transferred into EPR quartz tubes. The volume of the sample in the tubes was 120 μ l. The sample was deoxygenated by bubbling with argon for 2 min. The sample was immediately introduced into the spectrometer resonant cavity. Photochemistry induced by UV light is measured by in situ-ERP. The speed and concentration of the radical initiation were measured. UV spot cure (SP-9) was used as a UV light source.

Viscoelastic properties

The temperature dependence of the storage modulus and the $\tan \delta$ of the adhesives were measured using the Dynamic Mechanical Analyzer (DMA Q800, TA instruments, USA) with the film tension mode. Specimens of approximately 11 ~ 13 mm in length, 12 mm in width, and 3 mm in thickness were prepared. The test was conducted at a strain rate of 0.1% and a frequency of 1 Hz, with a heating rate of 5 $^{\circ}$ C/min within the temperature range of -60 ~ 100 $^{\circ}$ C.

Adhesion properties

The bonded specimens were prepared as 25 mm width samples. The 180 $^{\circ}$ peel strength was measured using a Texture Analyzer (TA-XT2i, Micro Stable Systems, UK). The samples were allowed to stand at room temperature for 24 h. A peeling test by crosshead speed of 300 mm/min was employed at 23 $^{\circ}$ C,

based on ASTM D3330. The force was recorded in units of N for three different runs, and the average force was recorded as a scale of N/25 mm.

The probe tack was measured by Texture Analyzer (TA-XT2i, Micro Stable Systems, UK). 5 mm diameter stainless steel probe was used. The probe tack was measured at 23 °C. The approach speed of the probe was 0.5 mm/s. After the probe contact the surface for 1 s, at a constant pressure of 100 g/cm², the debonding speed was 0.5 mm/s. Maximum debonding force was calculated (ASTM D3330).

Lap shear strength testing

Lap shear strength testing was conducted to measure the shear strain using an AllroundLine Z010 Universal Testing Machine (Zwick, Germany). Each specimen was pressed onto PET with 75 µm thickness film by two passes of a 2 kg rubber roller with an adhesion area of 25 × 25 mm². The tests were performed at a crosshead rate of 1 mm/s. The shear strain was calculated by

$$\text{Shear strain (\%)} = \frac{\Delta L}{t} \times 100$$

where ΔL is the moving distance, and t is the thickness of the PSA film.

Strain recovery testing

Strain recovery testing was conducted using a DMA Q800 (TA Instruments, USA) equipped with a tension clamp under the dynamic mechanical analysis (DMA) stress relaxation mode. Each specimen consisted of 60 µm acrylic PSA film between two polycarbonate substrates with an adhesion area of 20 × 6 mm².

The specimen was stabilized at 25 °C for 5 min under a stress of 0.001 N, and then 300% shear strain was applied for 10 min, followed by a recovery under 0.001 N for 5 min. The equation below was used to calculate strain recovery, where S_i and S_f are the initial strain at the beginning and the final strain after recovery for 5 min, respectively.

$$\text{Strain recovery (\%)} = \frac{S_i - S_f}{S_i}$$

Transmittance

The optical properties of the UV-cured acrylic PSAs was examined by UV Visible Spectroscopy (UV-2550, Shimadzu, Japan). The transmittance of two release films was measured and used as the control data. The transmittance of the OCA samples was measured with a release film on both sides. The transmittance was determined with the visible range of 400~800 nm. Acrylic OCA films were 60 μm , located between the PET release films of 60 μm .

Photo-DSC

The UV-curing reaction behavior of adhesives was measured by Differential Scanning Calorimeter (DSC; DSC Q200, TA Instruments, USA). The UV spot-cure light source (Omnicure-s2000, Excelitas, Waltham, MA, USA) utilized a 100 W of mercury lamp. The sample weighed approximately 10~15 mg. All measurements were carried out at a temperature of 25 °C.

2.2. Heterogeneous PSA using UV Patterning

2.2.1. Materials

The acrylate oligomer (2100M, Winnerschem Corp., Republic of Korea) was used as base adhesive resin (M_w : 40,653, PDI: 2.31, viscosity: 51 cP at 20°C, 200 rpm, refractive index: 1.4412 at 20°C). The glass transition temperature of uncured acrylate oligomer measured by Differential Scanning Calorimetry (DSC Q200, TA Instruments, USA) is -10°C. Polyethylene glycol 200 diacrylate (Miramer M282, Miwon Specialty Chemical Co., Ltd., Republic of Korea) was used as the crosslinking agent. Ethyl phenyl (2,4,6-trimethylbenzoyl) phosphinate (Omnirad 2100, Shinyoung Rad, Chem., Ltd., Republic of Korea) was used as the photoinitiator. A UV 365 nm LED light source was used for the curing process.

2.2.2. Preparation of UV Patterned Acrylic PSA film

An acrylic oligomer blended with 1 phr each of the photoinitiator and crosslinking agent was coated between silicon-treated PET release films (SKC Co., Ltd., Republic of Korea) by an applicator. The thickness of the coated oligomer blend was 60 μm . A UV LED lamp (area curing system, 365 nm, 7 mW/cm^2) irradiated the coated oligomer blend for primary curing. The distance between the lamp and the sample was 4 cm. The UV energy ranged from 0 to 4 J for each sample (Table 2-2). The detailed curing process is shown in Figure 2-5 a). After the primary curing is completed, photo mask film is put on the primarily cured PSA sheet, and secondary curing is performed by irradiating UV LED light. The photo mask film is placed directly on top of the release film. Figure 2-5 b) shows a schematic diagram and the size of the curing degree of the UV-pattern cured PSA. There is a variation in patterns 1–9 depending on

the difference in curing density between the island region and sea region of the pattern. The surface area of each island and sea region is composed of a 1:1 ratio. The number of radicals generated from the photoinitiator depends on the irradiated UV energy. Therefore, the number of radical reactions with the C=C double bond and the crosslinking densities of the irradiated sections vary. As a result, a UV-patterned PSA sheet composed of two sections with different crosslinking densities is manufactured.

Table 2-2. UV curing conditions of UV patterned PSA film.

| Pattern No. | UV Irradiated Energy of Sea Region (J) | UV Irradiated Energy of Island Region (J) | Energy Difference between Patterns (J) |
|-------------|--|---|--|
| 1 | 0 | 4 | -4 |
| 2 | 0.5 | 3.5 | -3 |
| 3 | 1 | 3 | -2 |
| 4 | 1.5 | 2.5 | -1 |
| 5 | 2 | 2 | 0 |
| 6 | 2.5 | 1.5 | 1 |
| 7 | 3 | 1 | 2 |
| 8 | 3.5 | 0.5 | 3 |
| 9 | 4 | 0 | 4 |

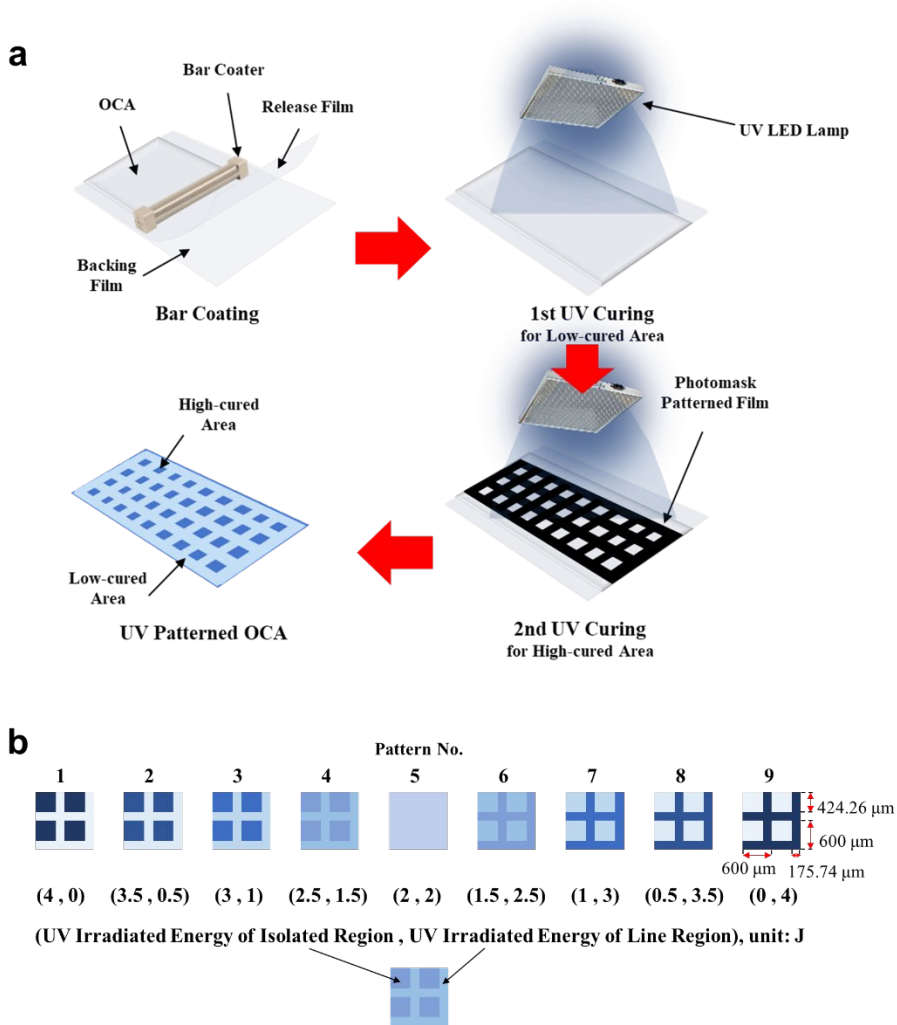


Figure 2-5. a) Process of manufacturing the UV patterned PSA film. b) Schematic diagram of the curing degree of UV patterned PSA containing quantitative size of the pattern repeating unit (Kim. *et al.*, 2021).

2.2.3. Characterization

Viscoelastic Properties

The Young's modulus (E , modulus of elasticity) of each cured section of the pattern was measured using atomic force microscopy (AFM, NX-10, Park Systems, Republic of Korea) in a pinpoint mode with pressing 0.8 V. The contact depth of the material with the probe was 10~50 nm, and the force was less than 10 nN. The AFM tip PPP-NCSTR (NANOSENSORS™, guaranteed tip radius of curvature < 10 nm, tip height 10~15 μm) was used to measure each cured region. The PSA coated onto the PET sheet was first cut into 5×5 mm samples. The PSA film was then peeled off and fixed to an AFM sample holder. The force-distance curve was measured at 10 points. The Young's modulus was calculated using the Oliver and Pharr model (Oliver, *et al.*, 1992, Pharr, *et al.*, 1992).

Viscoelastic properties of the whole PSA sample containing both low and high cured region, including storage modulus (G , modulus of shearing elasticity) and glass transition temperature, were measured using a rheometer (MCR302, Anton Paar, Austria). The oscillatory temperature sweep experiments of the samples were conducted at an angular frequency of 10 rad/s. The strain was 1%, and the preloading force was 1 N. The probe diameter was 8 mm. The measuring PSA sample diameter was 8 mm, containing both high and low cured regions.

Strain recovery and stress relaxation

DMA (Q800, TA Instruments, USA) in the tension film mode was used to evaluate the strain recovery and stress relaxation properties of the PSA sheet. The release film covering the cured PSA sheet was peeled off and the cured PSA sheet was attached between the polycarbonate substrate (IS-Optics Co.,

Ltd) cut into $3 \times 0.6 \text{ cm}^2$, with the adhesion area of $2 \times 0.6 \text{ cm}^2$. The thickness of the polycarbonate substrate was 1 mm. A constant shear strain (50%) was applied for 10 min, then the force was decreased to zero for 5 min. The PSA experienced the shear strain between the polycarbonate substrates because the strain was applied in the tensile direction. The strain recovery (%) and stress relaxation (%) were calculated using the equation below from our previous work (Back, *et al.*, 2019).

$$\text{Strain recovery (\%)} = (S_0 - S_t) / S_0 \times 100$$

$$\text{Stress relaxation (\%)} = (F_i - F_f) / F_i \times 100$$

Adhesion properties and Transmittance

Based on ASTM D3330, the bonded specimens were prepared as 25 mm width samples to measure the 180° peel strength using a Texture Analyzer (TA-XT2i, Micro Stable Systems, UK). The specimens were left to stand at 20°C 55 % RH for 24 h before testing. A peeling test crosshead speed of 300 mm/min was employed at 23°C . The force (N) was recorded for three times, and the peeling force was averaged as scale of N/25 mm. The measurement was performed five times to calculate the average value and standard deviation.

The probe tack was measured by Texture Analyzer (TA-XT2i, Micro Stable Systems, UK). The information of the probe was 5 mm diameter stainless steel probe. The approaching speed of the probe was 0.5 mm/s. After the probe contact to the surface of the PSA for 1 s, at a constant pressure of 100 g/cm^2 , the debonding speed was 0.5 mm/s. The measurement was performed seven times to calculate the average value and standard deviation.

The transmittance of the UV-cured acrylic OCAs was examined using UV-

visible spectroscopy (UV-2550, Shimadzu, Japan), with empty air as the reference.

3. Results and Discussion

3.1. UV Curing System controlling Polymer Structure and Property

3.1.1. Molecular Structure: Conversion and Gel Fraction

Gel fraction was physically measured by using the weight ratio of insoluble polymers regarding the degree of crosslinking in the cured acrylic PSAs. The acrylic PSA gel fraction was presented by using UV exposure energy from 0 to 14 mW/cm² and UV exposure intensities from Level 10 (97 mW/cm²) to Level 99 (1,252 mW/cm²), as shown in Figure 2-6 a). With increasing UV exposure intensity, the gel fraction was gradually observed to increase. The gel fraction values for Levels 10, 20, and 30 increased at 5, 4, and 3 s, respectively, which indicates that higher UV exposure intensity induces a rapid onset of PSA crosslinking. The gel fraction for each UV exposure intensity reaches the saturation point; this point was decreased from a maximum of 75% (Level 10) to below 30% (Level 50 and higher), as seen in Figure 2-6 a). Even with low gel fraction levels, the PSA samples appeared fully cured (shaped in semi-solid phase, reduced tack, and no uncured resin flow).

In previous studies, UV exposure for PSA curing was usually controlled by only the UV exposure time with a fixed UV exposure intensity using a UV mercury lamp (Lee, *et al.*, 2016, Lee, *et al.*, 2012, Lee, *et al.*, 2013, Park, *et al.*, 2016) or UV metal halide lamp (Back, *et al.*, 2019). This study studied the curing behavior over a wide range of UV intensity and exposure energy using an LED curing system. At Level 10, the gel fraction continued to increase under

a UV exposure time of 10 s. The low intensity, however, necessitated a 20 s exposure period to reliably measure the gel fraction to completion, as shown in Figure 2-6 b). Different UV exposure intensity levels resulted in different gel fraction values even at the same level of UV exposure. Therefore, UV exposure intensity and time are crucial factors in UV LED curing. Four types of UV exposure intensity (Levels 10, 15, 20, and 30) were chosen for the study because their gel fractions showed relatively significant and meaningful differences, as shown in Figure 2-6 b).

The conversion of acrylic PSAs is shown in Figure 2-7. The conversion of C=C bonds increases as the UV exposure time was increased (Lee, *et al.*, 2016). Level 10 exhibited a slower conversion to the more rapid conversion rate of Level 30. The bond conversions reached close to totality (almost 100%) in comparison with corresponding gel fraction values. The conversion values of nearly 100% indicate that C=C bonds in acrylic PSAs were fully cured by UV LED exposure. Thus, the low saturation point of the gel fraction under high UV exposure intensity could be attributed to the large number of propagation chain, resulting in smaller and more condensed crosslinked clusters.

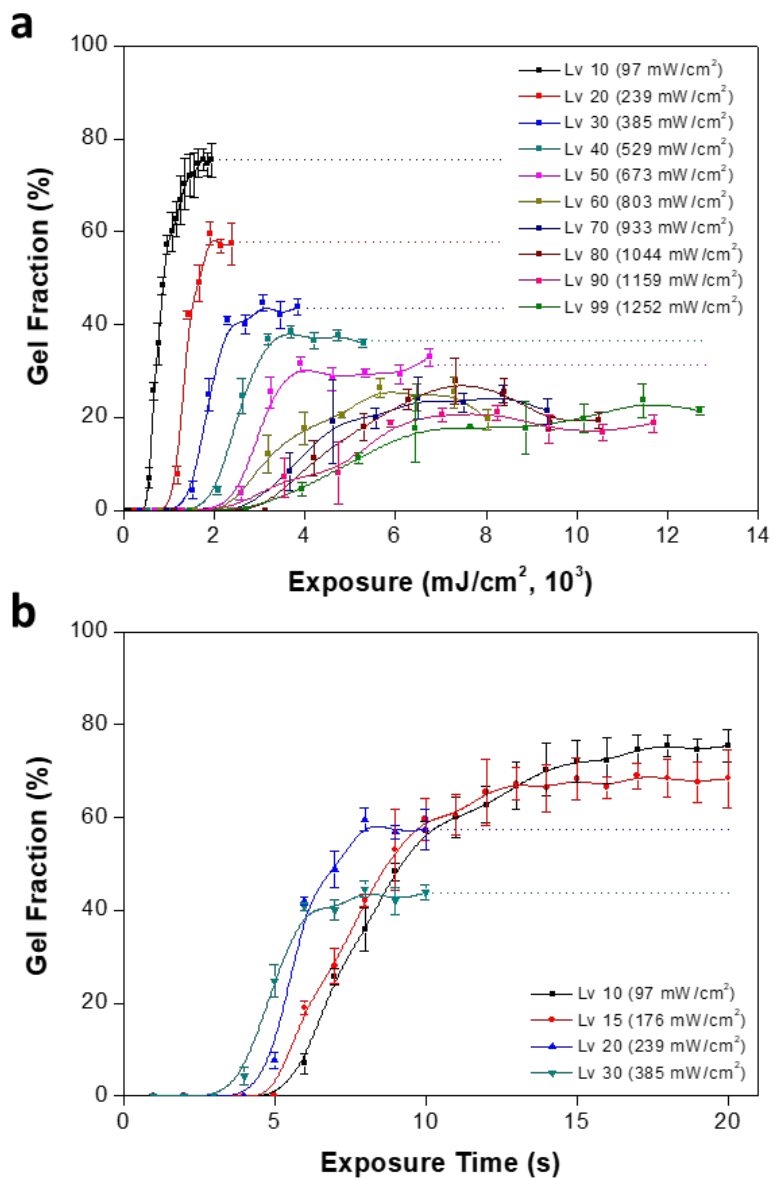


Figure 2-6. Effects of UV light intensity on the gel fraction of acrylic PSA samples as a function of a) UV exposure energy and b) exposure time. The lines are drawn for easier figure reading (Kim. *et al.*, 2021).

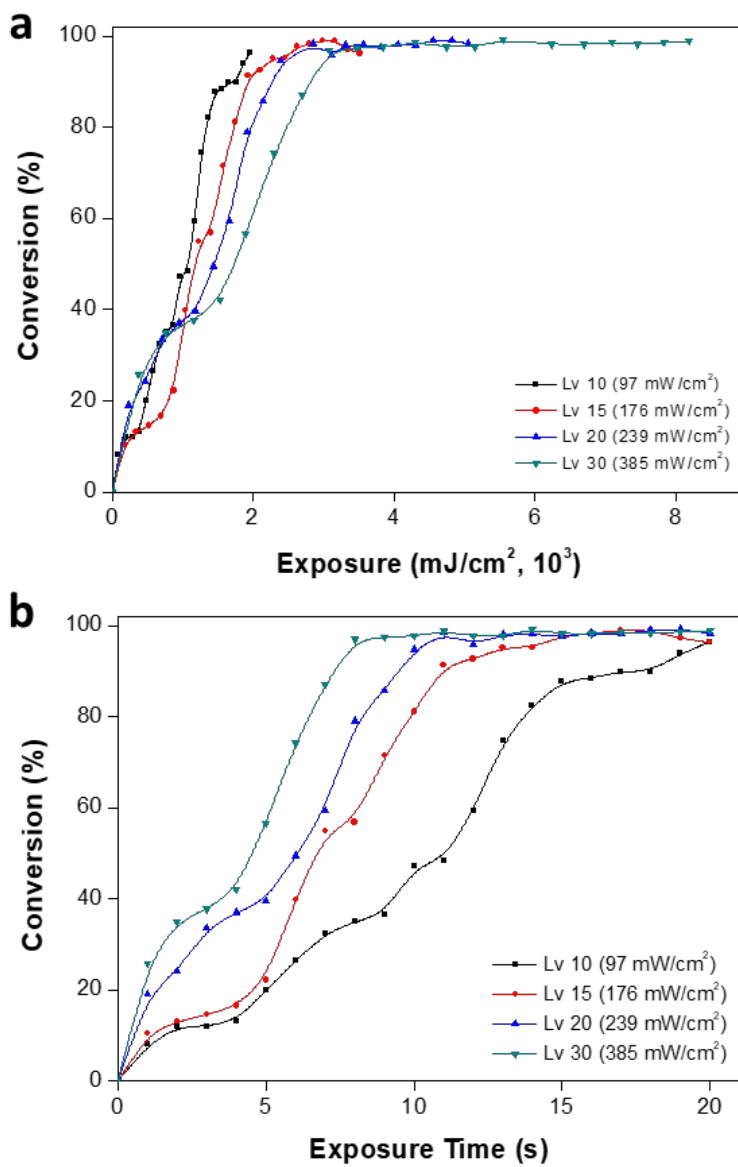


Figure 2-7. Effects of UV light intensity on the curing conversion of acrylic PSA films as a function of a) UV exposure energy and b) exposure time (Kim. *et al.*, 2021).

3.1.2. Mechanism of Structure Change: EPR and Real Time FT-IR

To understand the mechanism by which these crosslinking structures are changed, reaction observations using EPR and real time FT-IR were performed. When the concentration of initiated radicals was measured over time under UV irradiation, more radicals were initiated rapidly as the UV intensity was increased, i.e., the higher the intensity, the more initiators formed simultaneously, resulting in shorter and more numerous chains. This prevents the polymer structure from being organically linked. The reaction process is illustrated in Figure 2-10.

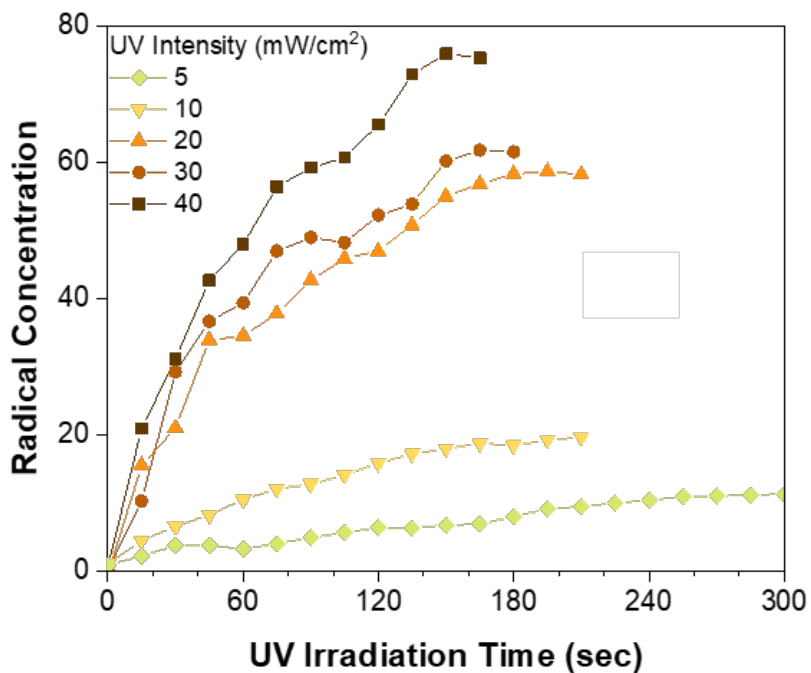


Figure 2-8. In-situ initiated radical concentration of each UV intensity measured by EPR.

There are three steps in UV curing type of polymerization: initiation, propagation, and termination. In the first stage, the initiation stage, by measuring radical initiation with EPR, we found that the amount and rate of radical initiation varies with UV intensity. Furthermore, we measured acrylic monomer's C double bond conversion under UV irradiation by real time FT-IR. The results showed that the higher the number of radicals initiated in the initiation stage, the faster the monomer is consumed in the propagation stage, i.e., more chains are propagating simultaneously. This makes a difference in whether the final polymer network structure is composed of short and many chains or few but long chains and affects the connectivity and robustness of the entire network.

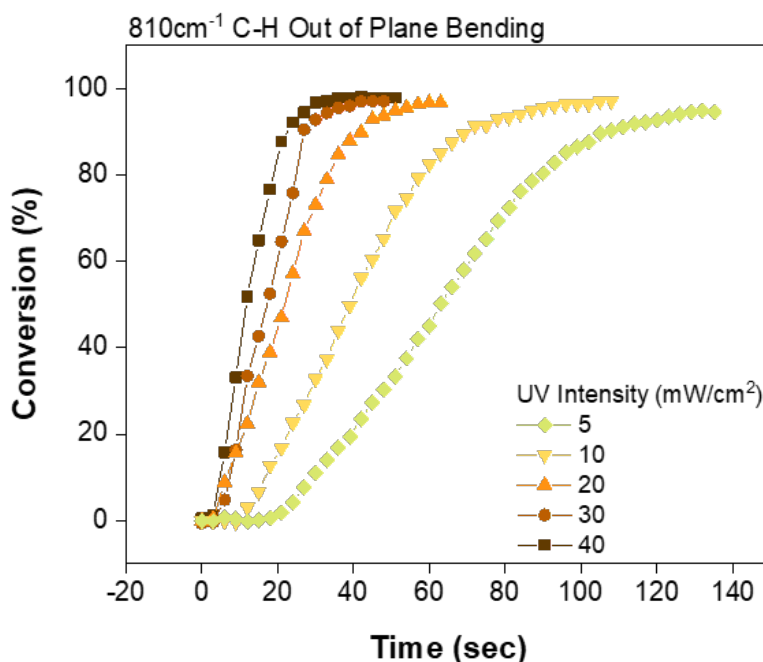


Figure 2-9. Change of C double bond conversion for each UV light intensity, measured by real time FT-IR.

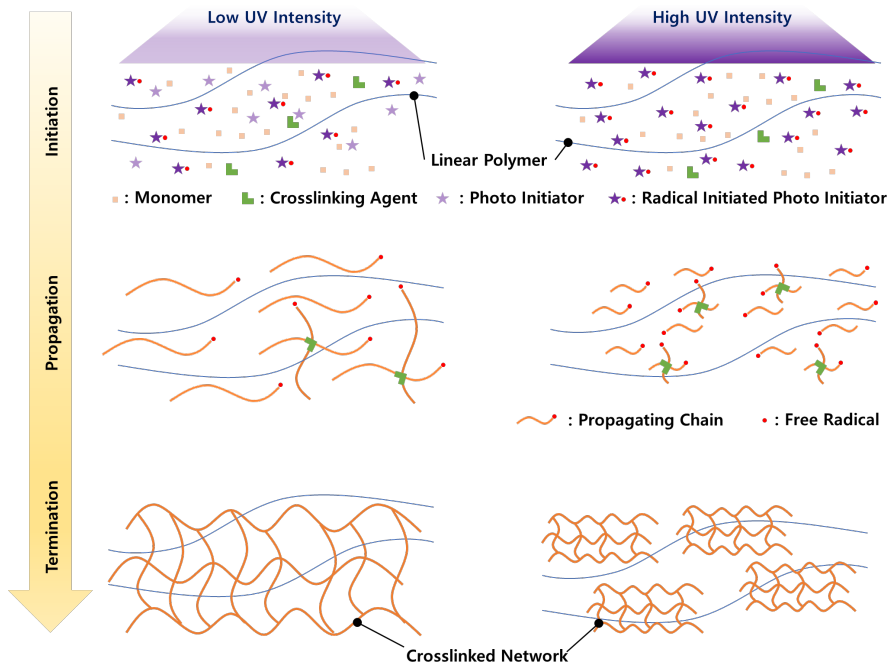


Figure 2-10. Differences in the number of propagating chains and hence differences in the final polymer network structure due to differences in the number of radicals initiated at low versus high UV intensity.

3.1.3. Mechanical Properties according to the Polymer Network Structure

As the UV dose increases, the peel strength improves as the reaction sites in the compound are exhausted. As the polymer network becomes more densely crosslinked and entangled, the adhesion properties improve until the wetting is reduced. The compositions used in this experiment have a low crosslinking agent content, meaning it does not become excessively crosslinked even when fully cured. Therefore, the adhesive properties improved with increasing UV exposure energy in the variable spectrum given in this experiment.

The lap shear strength is positively correlated with the cohesive force of the PSA. For the same UV exposure energy, the higher the intensity, the lower the

entanglement of the polymer due to the presence of more short chains in the bulk, resulting in a lower cohesive force. When the PSA sample is pulled, the sample undergoes the following processes: 1. The conformation of the polymer chain changes and stretches. 2. When the polymer chain can no longer stretch due to crosslinking or entanglement points, the polymer chain resists the applied force. 3. the polymer chain fails to resist, and some covalent bonds break, creating a yield point. 4. The entire covalent bond of the PSA breaks, and failure occurs. Therefore, as the crosslinking degree of the polymer network increases, the shear strain tends to decrease because the range of strain at which the polymer chain can stretch freely becomes shorter.

The strain recovery property is related to the adhesive force between the substrate and the PSA and the cohesive force within the PSA to withstand the shear applied during the test. Therefore, as crosslinking increases, adhesion and cohesive force increase, and so does recovery, until the adhesive properties decrease due to reduced wetting. In addition, excessive crosslinking shortens the length of strain at which the PSA does not break, so recovery generally tends to increase and decrease with crosslinking. In this experimental spectrum, the recovery tended to increase with increasing UV exposure because a small amount of crosslinker was added to prevent over-crosslinking.

In summary, in the variation given in this experiment, the increase in UV intensity at the same energy resulted in short and many chains due to the simultaneous consumption of monomers in large quantities. Therefore, conversion and cohesion decreased, resulting in decreased physical properties. At the same UV intensity, the increase in UV exposure energy resulted in the complete consumption of the reaction sites of the components, leading to an increase in crosslinking and cohesive force. This resulted in excellent adhesion and recovery but was limited to deficient shear strain. As demonstrated by Decker *et al.* (Decker, 2002), UV-curing systems are well known for their

ability to control the hardness and modulus of interpenetrating network (IPN) structures over a wide range. However, we have seen homogeneous networks have precise characteristics and limitations associated with the network structure, i.e., for balanced improvement of adhesion, elongation, and recovery properties, polymers with a uniform structure have limitations. The properties needed for modern, flexible devices can hardly be achieved with a simple change in UV conditioning. For this reason, we would like to prepare a non-homogeneous PSA in which two domains with different properties co-exist, such as the highly elastic structure of polyurethane.

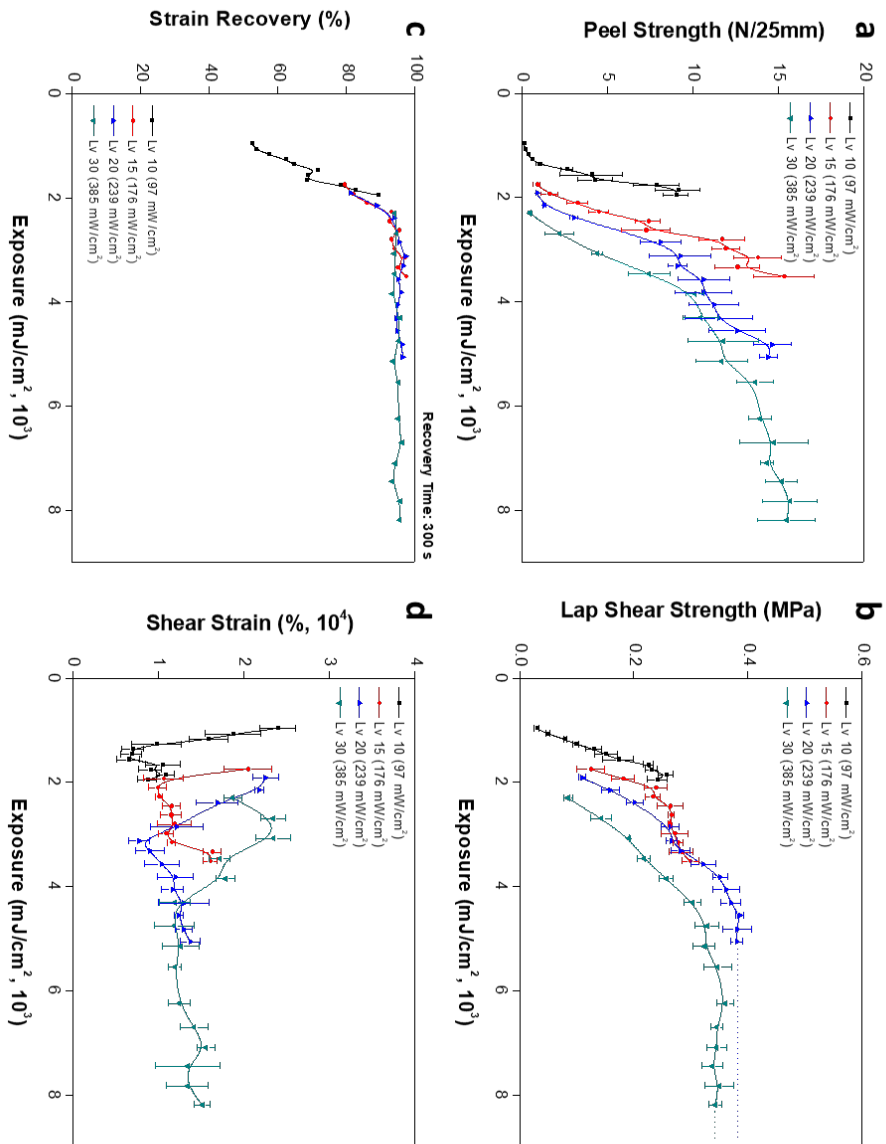


Figure 2-11. Physical properties of cured PSA film as a function of curing UV intensity. a) peel strength, b) lap shear strength, c) strain recovery, and d) shear strain (Kim. *et al.*, 2021).

3.2. UV/UV Step Curing

3.2.1. Kinetic Study for UV/UV Step Curing

We first investigated the possibility of step curing the UV curing system by photo-DSC to work on heterogeneous UV patterned PSA using photomasks. UV bulk curing is based on a chain reaction of free radicals via an initiator in the mixture. We wanted to see if it was possible to split the UV curing into two separate steps, as the radical reaction is swift and difficult to control. Reaction rate can be measured by monitoring the rate at which heat is released from a polymerizing sample, as polymerization is generally an exothermic reaction. Therefore, the profiles of the heat of reaction versus time, obtained by photo-DSC, can be used to characterize reaction kinetics and evaluate polymerization rate constants (Joo, *et al.*, 2007). The crosslinking sites that remain after primary cure cause an exothermic reaction when exposed to UV light during secondary cure. Figure 2-12 a) indicates the heat flow for UV curable resins irradiated with UV light after primary curing. Many reaction sites remained in the samples cured with 0.6 J/cm^2 UV light. The curing process resulted in a significant increase in both reaction and heat generation. The samples cured at 0.9 J/cm^2 exhibited a lower exothermic peak compared to those cured at 0.6 J/cm^2 , while the samples that were cured at 1.2 and 1.5 J/cm^2 showed almost no peak. Figure 2-12 b) indicates the remaining reaction sites and additional reactions after secondary curing. Tiny peaks were only observed at 0.6 J/cm^2 UV light exposure, while the other samples showed almost none after the second curing reaction. This suggests that, with the exception of the samples exposed to 0.6 J/cm^2 UV light energy, nearly all of the reaction sites underwent secondary curing, and no further crosslinking reactions took place.

Figure 2-12 c) and d) display the integral of photo-DSC data, which

represents the total amount of UV-induced reaction during photo-DSC measurement. This is equivalent to the number of residual reaction sites after primary and secondary curing. After primary curing, the samples cured with an illumination energy of 0.6 J/cm^2 exhibited more additional reactions compared to those cured with higher energy amounts of 0.9 , 1.2 , and 1.5 J/cm^2 . After the secondary curing process, the samples exhibited a slight reaction when exposed to an irradiation energy of 0.6 J/cm^2 . However, samples irradiated at 0.9 , 1.2 , and 1.5 J/cm^2 showed little to no reaction, indicating that they were fully cured after the secondary curing step.

Figure 2-13 displays the maximum heat flows and the approach times for primary and secondary curing step. This information is essential for describing the primary curing of the samples. As shown in Figure 2-13 a), in the case of primary curing, the heat flow values of the peaks decrease with increasing UV light exposure time. The corresponding approach times tend to increase as the amount of UV energy used in primary curing increases. This implies that during photo-DSC, the reaction rate will be faster, and the extent of the reaction will be more significant as the number of residual sites increases after primary curing. The data for samples after secondary curing, shown in Figure 2-13 b), is not particularly meaningful since there are no peaks in Figure 2-12 b). The experimental results confirmed that UV/UV step curing is possible for acrylic PSA. Based on the experimental results, we attempted to produce UV patterned PSA by secondary curing only certain areas after primary curing using a UV photomask.

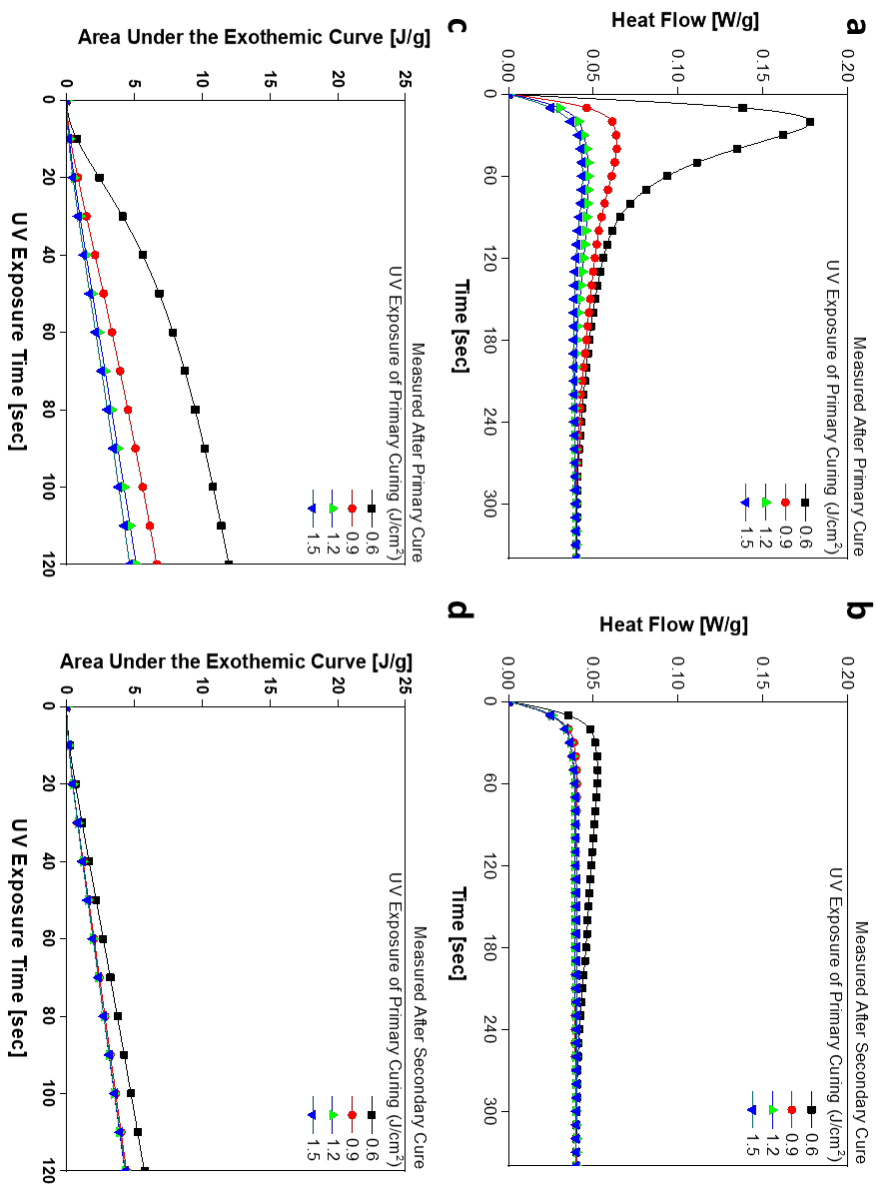


Figure 2-12. Real-time heat flow after a) primary and b) secondary curing step. Area under the exothermic curves corresponding to c) primary and d) secondary curing step (Kim. *et al.*, 2019).

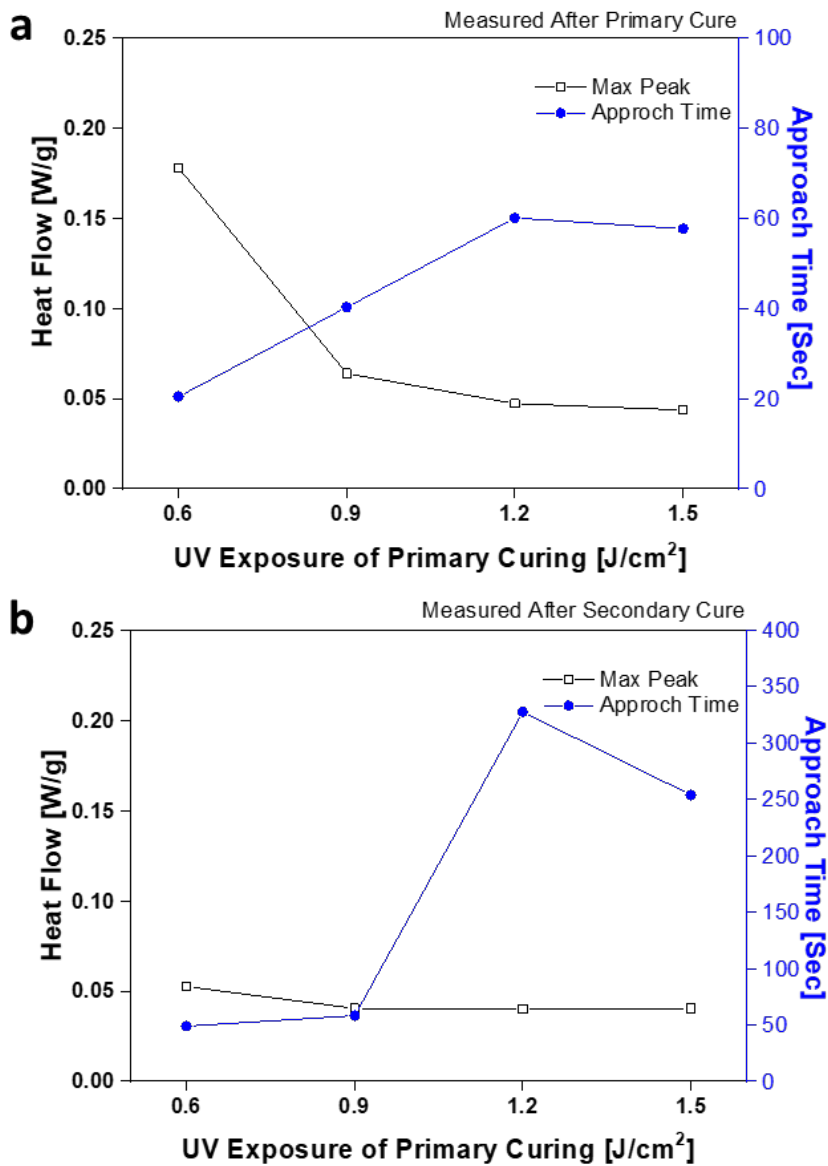


Figure 2-13. Maximum heat flows and corresponding approach times for a) primary and b) secondary curing step (Kim. *et al.*, 2019).

3.3. Heterogeneous PSA using UV Patterning

3.3.1. Identification of the UV Pattern Formation

To ensure that the inhomogeneous PSA utilizing the UV patterning technique was well prepared as intended, we wanted to verify the formation of each domain. The AFM measurement clearly confirms the formation of the curing pattern by showing a difference in Young's modulus for each high and low cured region according to the curing pattern. Each cured region of the samples showed different Young's modulus values, as shown in Figure 2-14. In the pattern 1 (Figure 2-5 b) sample, Young's modulus value of the island region was 8.6 MPa, whereas that of the sea region was 4.9 MPa. By measuring with AFM, the island and sea regions of each pattern-cured sample showed different Young's modulus values, confirming the formation of UV curing patterns. As the pattern number increased, the energy of UV irradiation to the sea region increased. As the UV irradiation energy increases, the number of radical species initiated from the photoinitiator increases, and more chain extension and crosslinking reactions proceed. An increase in storage modulus confirms the increase in the crosslinking density. As shown in Figure 2-14 a), Young's modulus of the sea region of each pattern increases with increasing UV energy irradiation and pattern number. In contrast, each pattern's modulus of the island region decreased with increasing UV energy irradiation and pattern number, as shown in Figure 2-14 b). The island and sea regions of each pattern were oppositely and separately cured according to the irradiated UV energy of each region.

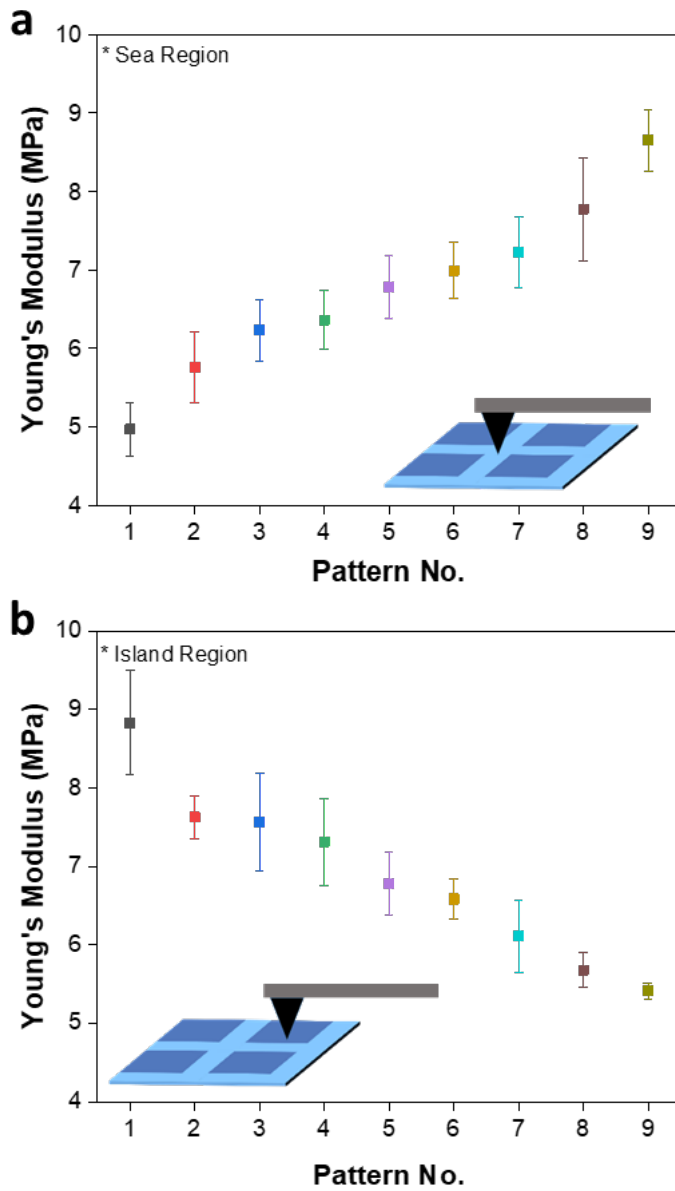


Figure 2-14. Young's modulus data of a) sea and b) island region of the UV pattern cured PSA samples (Kim. *et al.*, 2021).

3.3.2. Viscoelastic Property: Storage Modulus

The storage modulus value of the whole PSA sample containing both high and low cured regions does not show a considerable difference between samples. Still, it shows a clear trend: the storage modulus of each patterned sample (Figure 2-15) tended to increase with increasing curing density in one region. Dividing the PSA into two same-sized regions while irradiating them at different UV energies using photomask results in a higher curing density in one region over the other. Despite the differences in curing densities, the entire sample's storage modulus depends on regions with high curing density. Conversely, patterns 1 and 9 exhibited a decrease in the storage modulus of the entire sample. Both samples were cured under extreme conditions (energy of 0 J in one area and 4 J in the other), which resulted in the incomplete curing of one region, i.e., the difference in the curing densities between the regions was huge. The non-patterned sample (pattern 5) exhibited a storage modulus value of 12.8 kPa, while patterns 1 and 9 are 16.1 and 11.7 kPa, respectively. Despite their different curing densities, it is difficult to explain the similar physical properties of patterns 1, 5, and 9, as indicated by their storage moduli. The more even storage modulus was observed in patterns 6–9. Here, the PSA curing pattern was divided into a sea and island area, and the sea area had a relatively high curing density. In contrast, when the island region had a high curing density (patterns 1~4), a relatively high variability in the storage modulus value was measured. The sea regions are physically connected, which explains the sample's stable physical properties.

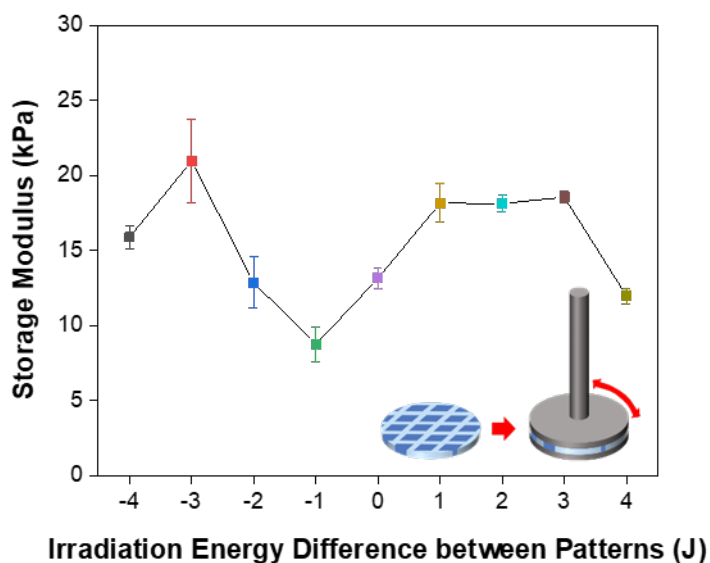


Figure 2-15. a) Storage modulus data measured by rheometer of the UV pattern cured PSA samples (25 °C, angular frequency of 10 rad/s) (Kim. *et al.*, 2021).

3.3.3. Flexibility: Strain Recovery and Stress Relaxation Properties

The difference in the roles of the sea and island areas, as determined by the different storage moduli of the sample, was also seen in the varying strain recovery properties. The patterned samples (6~8), which showed a high modulus due to the high curing density in the connected sea region, also showed better recovery performance than the non-patterned sample (pattern 5). For the sample with a highly cured connected region, the trend of the strain recovery properties followed that of the storage modulus. An increase in the storage modulus of the sample yielded excellent recovery properties (patterns 6~8) (Figure 2-16 c, R^2 is 0.9) because the physically connected line area provides

structural stability. This is the same result reported in the previous paper (Back, *et al.*, 2019). The modulus and recovery performance are determined by the interaction of molecules in each region cured non-homogeneously with different curing densities. The interconnected, high-cured sea region acts like a rope that provides firm support throughout the sample. Furthermore, the stress applied to the sample was unequally distributed throughout the sample but was concentrated at both points of the sample because of the bending modulus. However, the high-modulus sea region is linked through the whole sample, which enables the dispersion of the concentrated stress at both ends along the sea region. In addition, owing to the difference in the curing density, the samples were expected to exhibit a synergistic effect by flexibly stretching the lower cured area and buffering the plastic deformation of the highly cured area when under strain. In contrast, in patterns 1~4, which consisted of the highly cured island region and low cured sea region, the island region at both ends endured all of the concentrated stress on its own, resulting in interfacial and cohesive failure of the PSA. Therefore, no significant correlation was observed between the modulus and recovery performance of pattern 1~5 samples (Figure 2-16 d). Furthermore, the strain recovery value decreased as the difference in the curing density became larger (patterns 1 and 9), which was in agreement with the storage modulus trend.

The stress relaxation property was almost constant for moderate curing conditions (patterns 2~8). In contrast, it fluctuated under considerable differences in curing densities, i.e., it sharply increased for pattern 1 and decreased for pattern 9. Pattern 1 is characteristic of the sea region's extremely low crosslinking density and high viscosity. Therefore, there was no robust and resistant force at the crosslinking site when the sample was stretched, i.e., it stretched easily. Consequently, the polymer chains of the PSA easily moved, and the applied stress was well-dispersed, resulting in good stress relaxation

properties and low recovery performance because it nearly has the elastic force. In the case of pattern 9, the sea region was highly crosslinked and cured, which resisted the stretching of the sample, resulting in an inferior stress relaxation performance. In addition, the island region barely exhibits a recovery performance because of its extremely low crosslinking density. Thus, it can be concluded that because the strain recovery performance depends only on the sea region without synergetic effect or both regions, pattern 9 exhibits a lower recovery performance than other patterned samples (6~8).

3.3.4. Applicability to OCA: Adhesion Properties and Transmittance

Figure 2-17 a and b shows the peel strength and probe tack data. The patterns 1~4 and 6~9 samples showed similar adhesive properties to the non-patterned sample (pattern 5). Regarding peel strength, the non-patterned sample showed the highest value of 0.63 N/in. On the contrary, the patterned samples tended to decrease slightly, but maintained a similar adhesive performance (0.41~0.61 N/in) without significant deterioration (Figure 2-17 a). Regarding probe tack, except for the pattern 1 and 9 samples with the extreme curing energy difference, most of the samples (pattern 2~8) maintained similar adhesive properties between 3.1~3.7 N (Figure 2-17 b).

The representative data (pattern 8) of the measured transmittance are shown in Figure 2-17 c. All samples showed similar transparency values above 90% compared to the empty air reference. Thus, the patterned samples were transparent enough for application in an optically clear display adhesive.

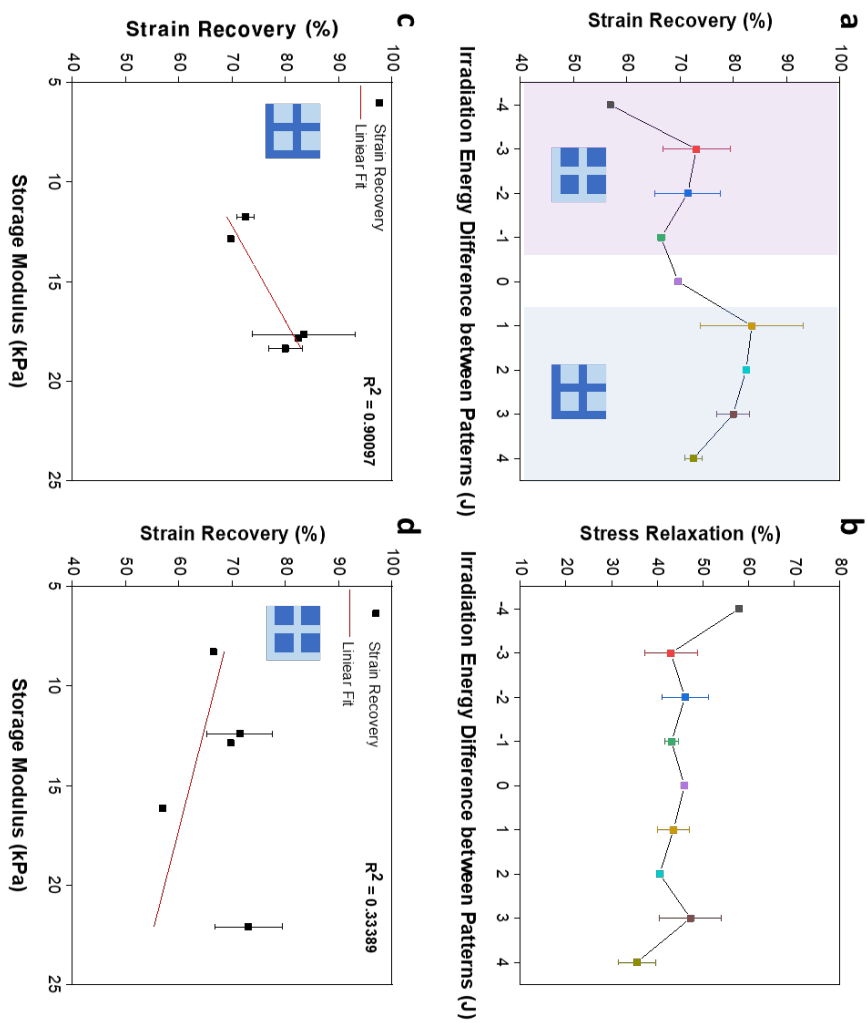


Figure 2-16. a) Strain recovery property, and b) stress relaxation property of the UV pattern cured PSA samples. The relationship between the storage modulus and strain recovery, with the trend line calculated by the least squares method, c) pattern 5 and 4~9 composed of a highly cured connected region d) pattern 5 and 1~4 composed of a highly cured island region (Kim. *et al.*, 2021).

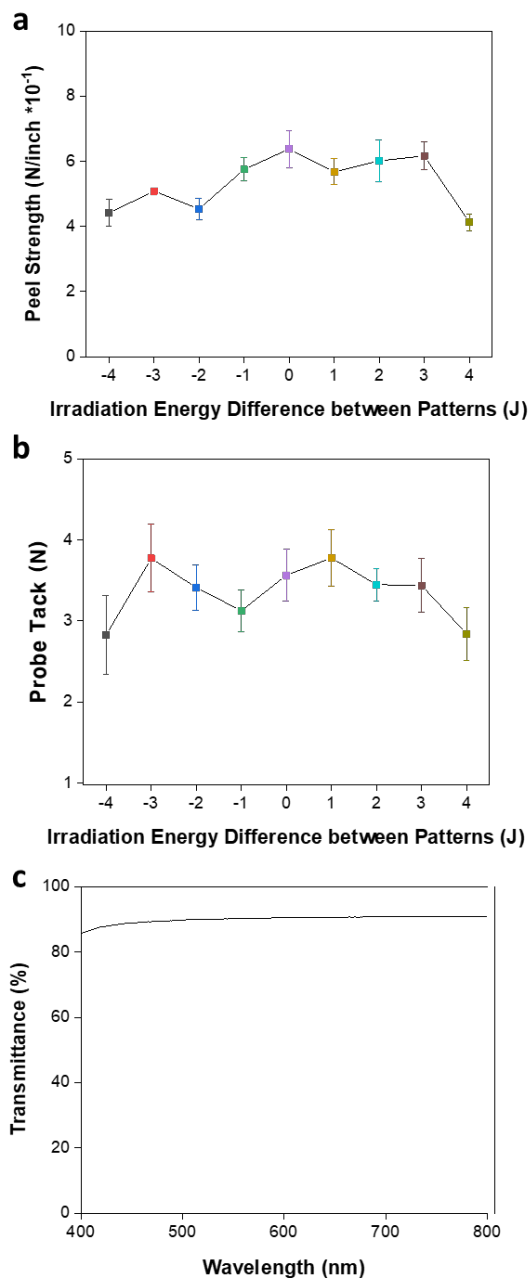


Figure 2-17. a) Peel strength, b) probe tack, and c) transmittance property of the UV pattern cured PSA samples (Kim. *et al.*, 2021).

4. Conclusions

We reported the basic molecular structure and properties of UV curing systems. We studied the structure of polymer networks and UV irradiation conditions by dose and intensity, and the limits of property control. To reach the properties required by state-of-the-art materials, we wanted to heterogenize the PSA. To confirm the feasibility of introducing UV patterning technology, we kinetically verified that dividing the acrylic UV bulk cure process into two steps is possible. Based on the feasibility of step curing, we used UV patterning technology using photomasks to produce UV Pattern PSA with compartments divided into distinct curing degrees. After confirming the UV curing pattern formation in the PSAs, the strain recovery and stress relaxation performance were measured to check their applicability in flexible displays. Compared to the non-patterned sample, the patterned sample showed a significant improvement in the recovery performance when the difference in UV curing energy between the patterns was 2~3 J. The patterned sample exhibited a relatively high modulus compared to the non-patterned sample when the energy difference was 2~3 J between the patterns. Finally, the adhesive performance of the PSA was maintained except for the sample with the most significant energy difference (4 J). Furthermore, all samples showed excellent transparency and applicability to optically clear adhesives (OCAs). In conclusion, our results show that implementing the curing density patterning technology during the UV irradiation process can maintain the adhesive properties and transparency while improving the recovery properties of the PSAs without changing the pre-polymer resin composition or additive content. However, although the adhesion performance of the heterogeneous samples was not inferior to the homogeneous samples, the expected dramatic improvement was not achieved. Reducing the domain size or designing other

forms of heterogeneous structures can compensate for this. However, UV patterning technology has limitations in further reducing the size of the domains due to the scattering properties of light. Therefore, in the following chapter, we studied the heterogeneous PSA of smaller-sized domains using living radical polymerization.

Chapter 3

*Nano Scale Heterogeneous PSA
using Polymerization-Induced
Microphase Separation*

1. Introduction

Pressure-sensitive adhesives (PSAs) can be applied to a substrate with a small amount of pressure without the solvent drying out or changing phase (Creton, 2003). Because PSAs are polymeric materials, a wide range of properties can be adjusted by polymer formulation and network design. This advantage enables PSAs to bond to different substrates, extending their applicability beyond everyday and general industrial use to the automotive, electrical, electronics, and biomedical industries (Creton, *et al.*, 2016).

The design scope of traditional polymers has been challenged with the development of flexible displays as the next generation of form factors in today's display industry. The challenge is making PSAs highly elastic, like a rubber band, while maintaining high adhesion properties. In general, the higher the storage modulus of a PSA, the denser and tighter the network, resulting in higher elasticity, but it isn't easy to withstand an extensive elongation range. In addition, as the storage modulus increases, the wetting performance of the PSA decreases, and the adhesive properties deteriorate. Therefore, designing a polymer network that exhibits good elasticity over an extensive strain range while still having high adhesion properties is the main challenge for research on PSAs for next-generation displays.

Since polymeric materials with homogeneous networks exhibit conflicting adhesive, elastic, and elongation properties depending on the nature of the network, many researchers have attempted to improve the properties by heterogenizing the polymeric network. The simplest way to inhomogenize polymers is by UV patterning (Back, *et al.*, 2019, Lee, *et al.*, 2021). While these studies reported improvements in adhesive properties or a balance of elongation and recovery properties, UV Patterning method has limitations due to the difficulty of reducing the domain size. PSA studies that have imparted small

nanoscale inhomogeneous domain sizes utilize the self-assembly phenomenon of block copolymers (Creton, *et al.*, 2005, Gallagher, *et al.*, 2016, Yamamoto, *et al.*, 2002).

In the days when rounded edges of displays were preferred, assembly was achieved by laminating pre-dried or cured semi-solid forms of adhesive materials. Nowadays, the edges of the panels have reverted to being flat, and the method of OCR applied in the form of resin, and then UV curing during the assembly process is favored due to its greater economy.

Therefore, in this study, we have chosen to use the PIMS method to design a non-homogeneous PSA that takes advantage of the self-assembly of block polymers but can be cured directly in the bulk without the use of solvents for application as an OCR. Improvements in the toughness and elongation at break (Bobrin, *et al.*, 2022, Bobrin, *et al.*, 2022), elastic modulus (Chopade, *et al.*, 2016, Chopade, *et al.*, 2017, Liu, *et al.*, 2022, Schulze, *et al.*, 2014) of heterogeneous polymeric materials using PIMS have been reported. However, its use as a PSA has not been reported. Previously reported PIMS materials are difficult to use as PSAs because of their high stiffness and lack of adhesion.

We have designed a heterogeneous PSA with excellent adhesive properties and a wide range of elastic behaviors like a rubber band. This is achieved using soft PBA domains and a matrix organically linked by a mixture of butyl acrylate and acrylic acid. In contrast to the polymerization method of conventional block copolymers, this PSA does not require solvents. It is cured in bulk by UV irradiation during self-assembly simultaneously with chain elongation. The PSA we designed exhibited linear elastic behavior with no energy dissipation in the strain range above 300%. We subjected it to cyclic testing by applying a repeated strain, and it did not show any energy dissipation for 30 repeated cycles. These innovative, highly flexible PSAs may enable the realization of flexible displays, including stretchable displays.

2. Experimental

2.1. Materials

Materials were selected based on compatibility differences, which is a driving force for self-assembly. Butyl acrylate, a hydrophobic monomer that lowers the overall T_g of the polymer and provides excellent wetting, was selected as the polymer material for the soft domain. Acrylic acid, a hydrophilic monomer that increases adhesion through hydrogen bonding in the substrate and bulk, was selected as the matrix component. PBA was designed to form the soft domain. BA and AA were crosslinked together to form the hard matrix. The followings were purchased from Sigma-Aldrich (USA): butyl acrylate (BA, >99%), poly(ethylene glycol) diacrylate average $M_n = 250$ (PEGDA, >92%), diphenyl(2,4,6-trimethylbenzoyl) phosphine oxide (TPO, >97%), aluminum oxide neutral (99%), 2,2'-azobis(2-methylpropionitrile) solution (AIBN solution, 0.2 M in toluene), acetonitrile (99.5%), and hexylamine (>96%), 2-bromopropionic acid (99%), 1-butanethiol (99%), hydrochloric acid (37% dilution). The followings were purchased from Samchun Chemicals Co., Ltd. (Republic of Korea): acetone (99.0%), tetrahydrofuran (THF, 99.9%), acrylic acid (AA, 99%). Carbon disulfide was purchased from Kanto Chemical co., inc. (Japan), and sodium hydroxide (NaOH) and DI water were purchased from Daejung (Republic of Korea).

2.2. Synthesis of 2-(butylthiocarbonothioylthio) Propanoic Acid

The synthesis method was based on a procedure described by Swift (Swift, *et al.*, 2016). Butanethiol (43.00 g, 0.47 mol) and 20 ml acetone was added

dropwise to a 90 ml sodium hydroxide solution (16.0 g, 0.40 mol) at 15 °C. The solution was stirred for 30 min, then cooled to 5 °C, at which temperature 30 ml carbon disulfide was added before being left for a further 30 min. 2-Bromopropionic acid (66.0 g, 0.43 mol) was added, followed by another 30 ml NaOH solution and 25 ml deionized water. This was left to stir for 24 h at room temperature before the orange mixture was extracted using 50 ml concentrated HCl and filtered to extract yellow solid. This was repeatedly washed with cold water, resuspended in a stirring solution, and finally recrystallized in hexane.

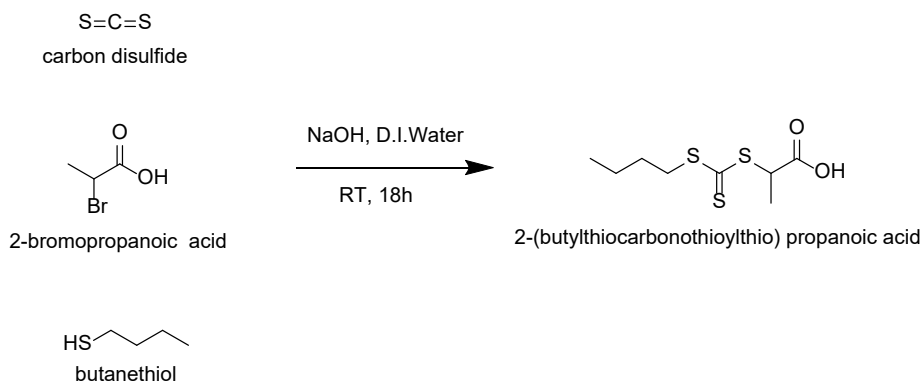


Figure 3-1. Synthesis of 2-(butylthiocarbonothioylthio) propanoic acid

2.3. RAFT Polymerization of Macro CTA (PBA₉₆-CTA)

After removing the inhibitor of BA using neutral aluminum oxide, BA (12.3 g, 96 mmol), BTPA (0.24 g, 1 mmol), and AIBN (0.02 g, 0.1 mmol) were added to Acetonitrile (30 mL). The reaction mixture was sealed with a septum before being stirred at 300 rpm and sparged under nitrogen for 60 min. The mixture was polymerized for 15 h at 60 °C. The reaction was stopped by cooling inside a freezer (-20 °C) and exposing to air. The polymer solution was concentrated by rotary evaporation and used without further purification.

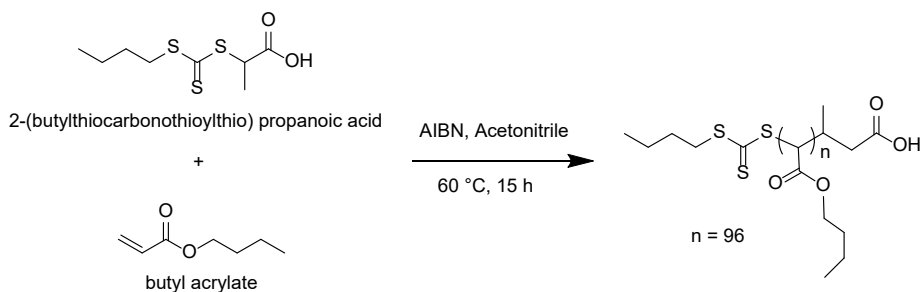


Figure 3-2. RAFT polymerization of PBA₉₆-CTA

2.4. Aminolysis of Macro-CTA

PBA₉₆-CTA (5.3 g, 8.3×10^{-4} mol) was dissolved in acetonitrile (17 mL). The solution was deoxygenated by purging with dry nitrogen for 90 min. To this solution, methyl acrylate (0.43 mL, 4.8×10^{-3} mol) was injected via a syringe, followed by the injection of hexylamine (0.42 mL, 3.2×10^{-3} mol). The reaction was allowed to react for 15 h at 22 °C. After 15 h, the yellow colour of the RAFT end group was still present, so more methyl acrylate (0.14 mL, 1.6×10^{-3} mol) and hexylamine (0.42 mL, 3.2×10^{-3} mol) were injected to the reaction solution. The reaction was allowed to react for another 5 h. The reaction solution was then concentrated by rotary evaporation, then redissolved in chloroform and washed five times with D.I. water (5×30 mL). The polymer solution was then dried over anhydrous MgSO₄, filtered, and reduced in volume by rotary evaporation. The resulting mixture was used without further purification.

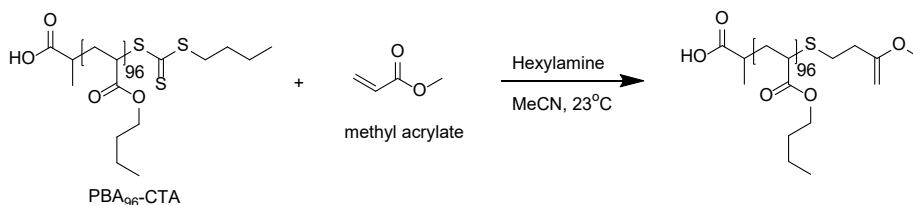


Figure 3-3. Synthesis of inert PBA₉₆ via aminolysis of PBA₉₆-CTA in the presence of methyl acrylate.

2.5. Preparation of the Nanostructured PSA Specimens

2.5.1. Homogeneous PSA

Homogeneous PSA was prepared by mixing an acrylic monomer (BA, AA) and a crosslinking agent (PEGDA). The reaction mixture was mixed for 2 min with 2000 rpm, and then defoamed for 2min, 2000 rpm. The mixture is coated between release films, and then irradiated with UV light (mercury lamp, 20mW/cm², main wavelength 365 nm) for 10 min to prepare a crosslinked polymer network. The reactants were mixed as listed in Table 3-1 to create a crosslinked network composed of random copolymers.

Table 3-1. Compositions of mixtures applied to manufacture the nanostructured PSAs. R: homogeneous random copolymer; B: micro phase separated PIMS PSA containing soft block of PBA, L: macro phase separated PSA blended with linear PBA.

| | BA | AA | PEGDA | Macro CTA | PBA₉₆ | TPO |
|-------|-----------|-----------|--------------|------------------|-------------------------|------------|
| B30 | 65 | 5 | 0.50 | 0.31 | | |
| B40 | 55 | 5 | 0.50 | 0.42 | | |
| L30 | 65 | 5 | 0.50 | | 0.31 | |
| L40 | 55 | 5 | 0.50 | | 0.42 | |
| R0 | 95 | 5 | | | | 0.5 |
| R0.05 | 95 | 5 | 0.05 | | | |
| R0.1 | 95 | 5 | 0.10 | | | |
| R0.3 | 95 | 5 | 0.30 | | | |
| R0.5 | 95 | 5 | 0.50 | | | |

2.5.2. PIMS PSA

PIMS PSA was prepared by chain extension of Macro CTA with acrylic monomer and PEGDA initiated with TPO. Macro CTA was dissolved in BA and AA monomer, then TPO was added. The reaction mixture was mixed for 2 min with 2000 rpm, and then defoamed for 2 min, 2000 rpm. The mixture is coated between release films, and then irradiated with a UV light (mercury lamp, 20mW/cm², main wavelength 365 nm) for 10 min. Finally, a crosslinked acrylic polymer network to which PBA₉₆ blocks were covalently bonded was obtained. As such, micro heterogeneous PSA was prepared using PIMS, which induces micro phase separation simultaneously with chain extension and crosslinking reactions of the polymer.

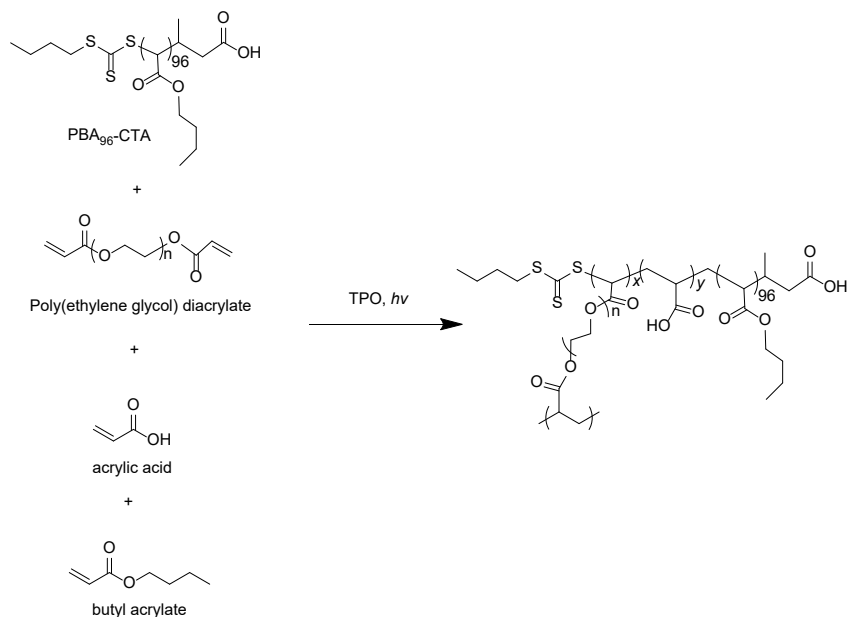


Figure 3-4. Photoinitiated RAFT copolymerization of AA, BA, and PEGDA in the presence of PBA₉₆-CTA and TPO.

2.5.3. Blend PSA

Blend PSA was prepared by blending linear PBA₉₆ block with monomers that form a network. PBA block form which BTPA has been removed through aminolysis, are mixed with BA, AA, PEGDA, and TPO. The reaction mixture was mixed for 2 min with 2000 rpm, and then defoamed for 2 min, 2000 rpm. The mixture is coated between release films, and then irradiated with a UV light (mercury lamp, 20 mW/cm², main wavelength 365 nm) for 10 min. The BA, AA and PEGDA initiated with TPO made crosslinked network, which is penetrated with PBA linear polymer, so called semi IPN network.

2.5.4. Crosslinked Polymer Matrix of Heterogeneous PSAs.

The B30 and B40 samples have a structure in which the PBA₉₆ domain and the matrix crosslinked with BA, AA, and PEGDA are covalently bonded. The L30 and L40 samples have a structure in which CTA removed PBA₉₆ linear polymer is blended in a matrix crosslinked with BA, AA, and PEGDA. In order to distinguish the T_g of the crosslinked matrix, we prepared only the matrix crosslinked with BA, AA, and PEGDA. BA 55 mol%, AA 5 mol%, PEGDA 0.5 mol%, TPO 0.5 mol% were mixed. The reaction mixture was mixed for 2 min with 2000 rpm, and then defoamed for 2min, 2000 rpm. The mixture is coated between release film, and then irradiated UV light (mercury lamp, 20mW/cm², main wavelength 365nm) for 10 min to prepare a crosslinked polymer network.

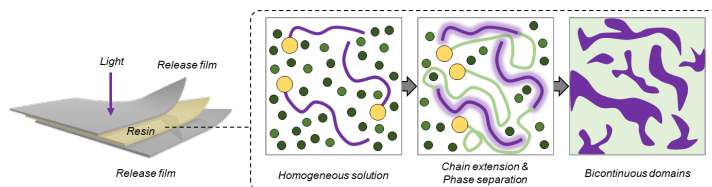


Figure 3-5. Preparing heterogeneous polymer network using PIMS.

2.6. Characterization

2.6.1. Nuclear Magnetic Resonance (NMR) Spectroscopy

A 400 MHz NMR spectrometer (JNM-ECX400, JEOL) was used to record the ^1H -NMR spectra. The operating temperature was room temperature, and tetramethylsilane ($\delta = 0$ ppm) was used as a reference to determine the chemical shift.

2.6.2. Gel Permeation Chromatography (GPC)

The molecular weight and polydisperse index of polymers were measured by gel permeation chromatography. The specific method is described in Section 2.1.5. of Chapter 2.

2.6.3. Transmission Electron Microscope (TEM)

Ultrathin sections (100 nm) of PSAs were microtomed at room temperature using ultramicrotome (EM UC7, Leica). Sections were picked up on 200 mesh carbon supported copper grid films (EMS) and double liquid stained. Stain 1: with 2% uranyl acetate for 20 min at 20°C. Stain 2: with 3% lead citrate, for 5min, at 20°C. TEM measurement were carried out in the bright field mode on an energy-filtering transmission electron microscope (EF-TEM, LIBRA 120, Carl Zeiss) operated at 120 kV.

2.6.4. Wide Angle X-ray Scattering (WAXS)

Wide-angle x-ray scattering data were collected using a XEUSS2.0 in the θ range of 5~50°. The distance was 80 mm and the wavelength was 1.542 Å. The thickness of the specimen was a film of 50 μm .

2.6.5. DSC Measurement

The T_g of the nanostructured PSAs were measured by loading each PSA (15–18 mg) onto a sample pan (Tzero Pan, 901683.901, TA Instruments) and applying Differential Scanning Calorimetry (DSC, Q200, TA Instruments). After being heated to 100 °C at a rate of 10 °C/min, and jump to -80 °C, the temperature of each specimen was maintained for 15 min. The DSC curve was recorded as the specimen was heated to 100 °C at a rate of 2 °C/min. All steps were carried out under dark conditions.

2.6.6. Storage Modulus and T_g

The temperature-dependence of the dynamic storage modulus and the tangent delta values of the adhesives were evaluated using a Dynamic Mechanical Analyzer (DMA Q800, TA instruments, USA) in the film-tension mode. Specimens of approximately 9~11 mm length, 12 mm width, and 1 mm thickness were prepared. The test was conducted at a strain rate of 0.1% and frequency of 1 Hz, with a heating rate of 5 °C /min within the temperature range of -60 °C to 150 °C. The Frequency-dependence of the storage modulus and the tangent delta of the adhesives were measured by frequency sweep test. The frequency range was 100 to 0.01 Hz with iso-temperature of 25 °C.

2.6.7. Tensile Test and Cyclic Stretching-Recovery Property

The tensile tests of the PSAs were conducted using a Texture Analyzer (TA-XT plus, Stable Micro System) with a 6 mm/min crosshead rate at 25 °C. The size of the sample is 15 mm in length, 1 mm in thickness and 12 mm in width, and the distance between the fixtures securing the top and bottom of the sample is 10 mm. The cyclic tensile test involved stretching the sample at a speed of 6 mm/min up to 300% strain, then returning it back to 0% at a same speed,

repeated for 8 cycles.

2.6.8. Adhesion Property

Based on ASTM D3330, the bonded specimens were prepared as 10 mm width and 3 μm thickness samples to measure the 180 ° peel strength using a Texture Analyzer. The specific method is described in Section 2.1.5. of Chapter 2.

2.6.9. Stress Relaxation Test

DMA (Q800, TA Instruments, USA) in the tension film mode was used to evaluate the strain recovery and stress relaxation properties of the PSA sheet. The release film covering cured PSA sheet was peeled off and the cured PSA sheet was attached between the poly(methyl methacrylate) substrate (IS-Optics Co., Ltd) cut into $2 \times 0.6 \text{ cm}^2$, with the adhesion area of $1 \times 0.6 \text{ cm}^2$. The thickness of the poly(methyl methacrylate) substrate was 1 mm. A constant shear strain (100%) was applied for 10 min, and then the force was removed to zero for 5 min.

3. Results and Discussion

3.1. Results of Synthesis and Polymerization

3.1.1. Synthesis of 2-(butylthiocarbonothioylthio) Propanoic Acid

The yield of the synthesized 2-(butylthiocarbonothioylthio) propanoic acid was 82.1%. The chemical structure was defined by the $^1\text{H-NMR}$ spectrum (Figure 3-6). It was confirmed that the starting materials, 2-bromopropanoic acid, and butanethiol did not exist in the compound through the absence of doublet near 1.92 ppm (corresponding to methyl group of 2-bromopropanoic acid), and triplet near 2.53 ppm (corresponding to methylene of butanethiol).

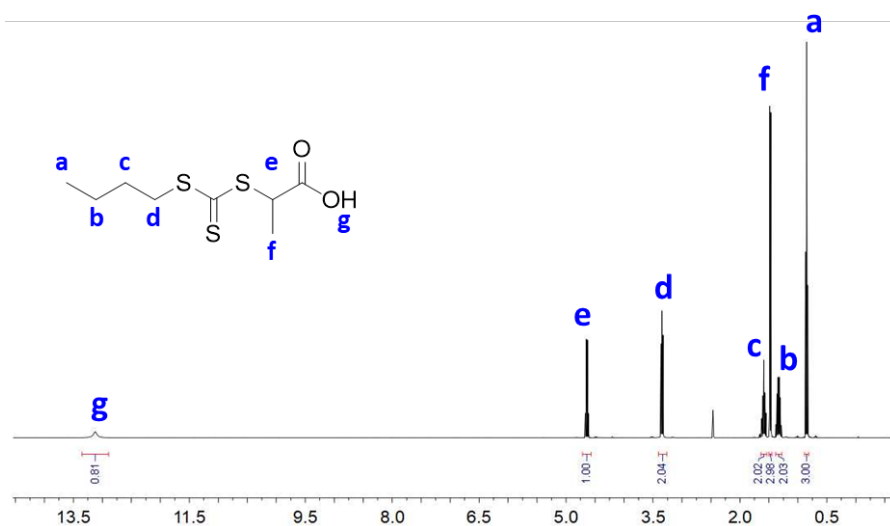


Figure 3-6. $^1\text{H-NMR}$ result of BTPA synthesized.

3.1.2. RAFT Polymerization of Macro-CTA

The yield of the synthesis of Macro-CTA was 79.6%. The molecular weight of the macro-CTA measured by GPC is 13,800, which is adjacent to target M_n . The M_w by GPC was 16,400 and the PDI was 1.1888. The chemical structure was defined by the $^1\text{H-NMR}$ spectrum. The degree of polymerization (DP) of butyl acrylate calculated by NMR was 92. The molecular weight calculated by NMR result was 12,075.

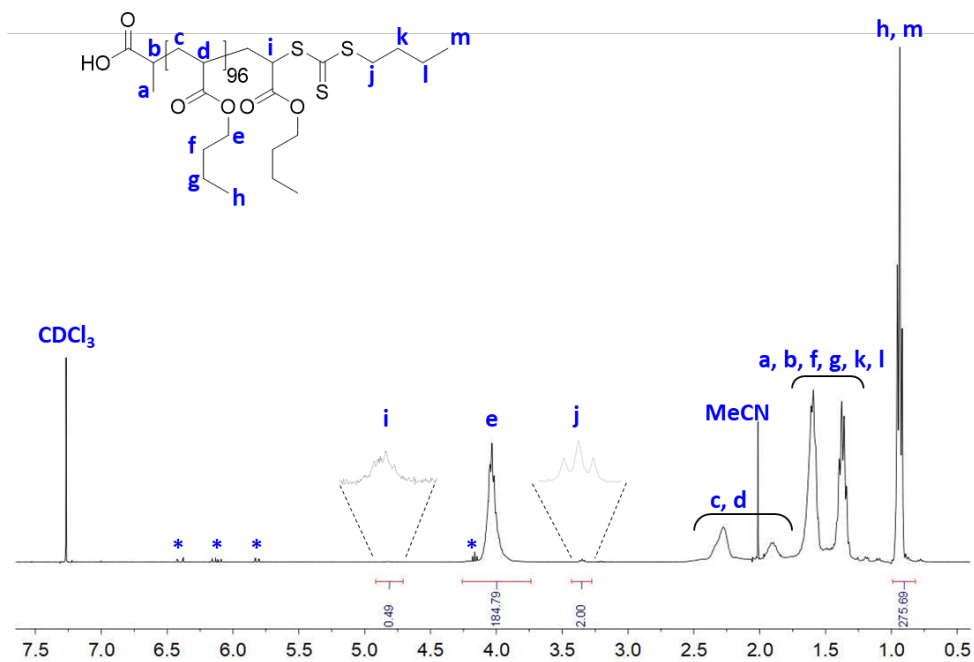


Figure 3-7. $^1\text{H-NMR}$ result of RAFT polymerized $\text{PBA}_{96}\text{-CTA}$. *: residual BA monomer.

3.1.3. Aminolysis of Macro-CTA

The yield of the PBA chain with a CTA removed by aminolysis was 42.3%. The chemical structure was defined by the $^1\text{H-NMR}$ spectrum. The by-product, methyl 3-(hexylamino) propanoate was detected together (Figure 3-8)

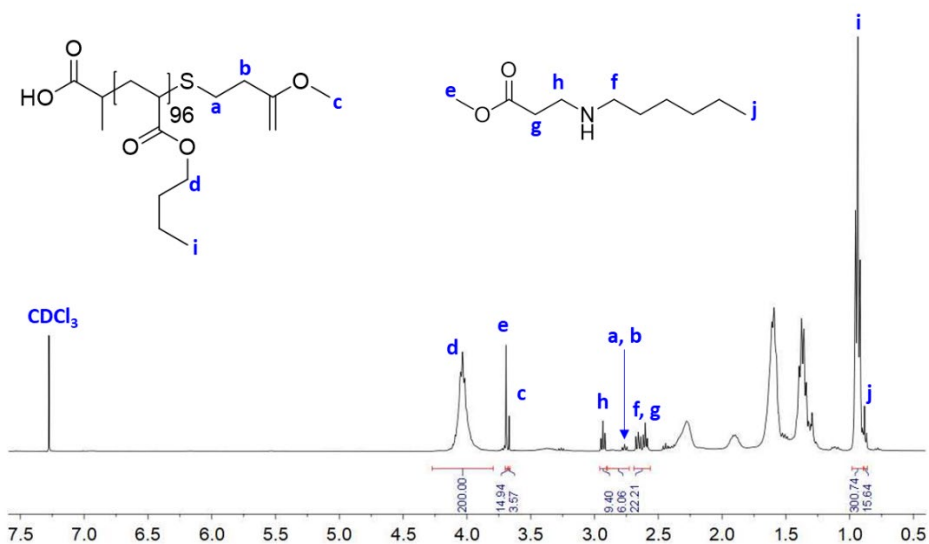


Figure 3-8. $^1\text{H-NMR}$ result of inert PBA_{96} linear polymer chain which is removed BTPA by aminolysis. The by-product, methyl 3-(hexylamino) propanoate was detected.

3.2. Confirmation of Heterogeneous Structure

3.2.1. TEM Image

In TEM images of Figure 3-9, the dark regions where heavy metals are chelated to AA, represent areas with a high concentration of AA. The homogeneous PSA (a and d) exhibits a uniform morphology, while the B40 (b and e) displays heterogeneous morphology. The formation of such heterogeneous domains indicates the successful manifestation of micro phase separation through the method using PIMS. Here, the size of the bright soft domains of the PBA₉₆ block which is covalently bonded to matrix is estimated to be approximately 200~400 nm. L40 (c and f), where linear PBA₉₆ polymer is penetrated a crosslinked network structure, also exhibits heterogeneous morphology.

3.2.2. WAXS

The peak area of the WAXS curve represents the degree of crystallinity (Townsend, *et al.*, 2005). B30 and B40 have an increased peak area than R0.5. In other words, it shows the result of a slight increase in crystallinity due to the influence of the microphase separation induced by PIMS. L30 and L40 show much higher crystallinity than PIMS PSA. This indicates that the separation between the matrix and the PBA₉₆ domain is more intensified because the linear PBA₉₆ and the crosslinked matrix do not bond chemically.

The peak position of the curve also indicates a crystalline structure. Random copolymerized R0.5, PIMS B40 and B30, and linear PBA blended L40 and L30 showed a peak shift to the right sequentially, indicating a difference in the polymer microcrystal structure.

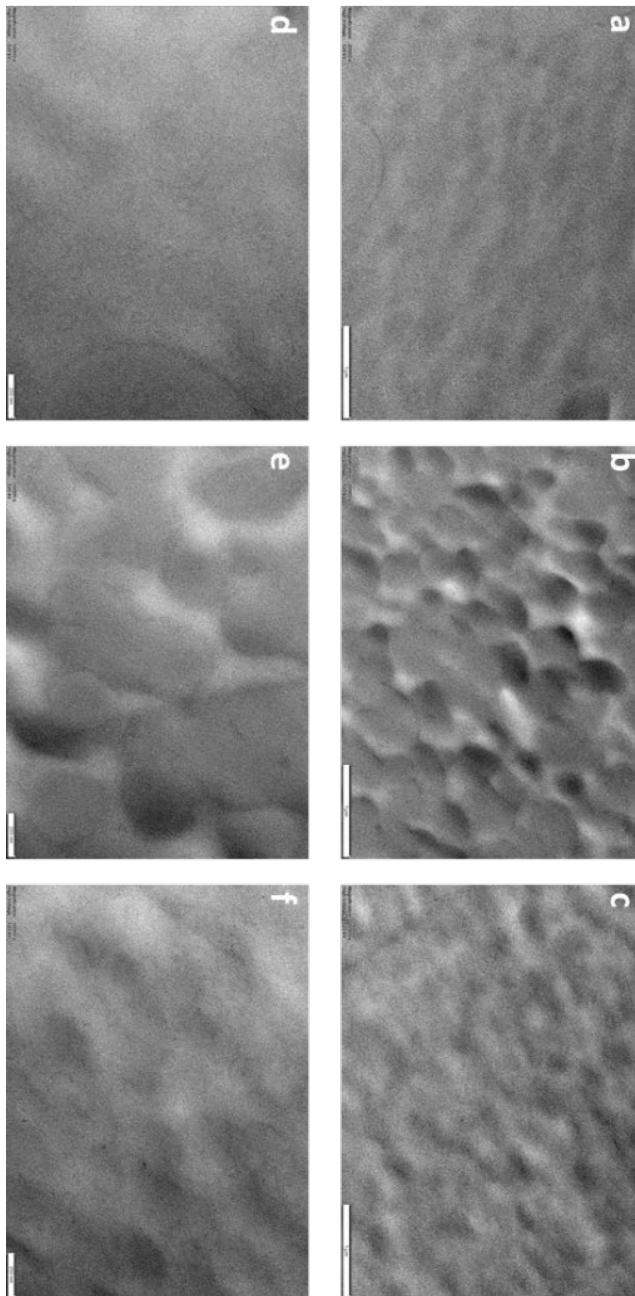


Figure 3-9. TEM images of the cured PSA. a, d) R0.5; b, e) B40, and c, f) L40, magnification: a, b, c) 20,000 x, d, e, f) 50,000 x

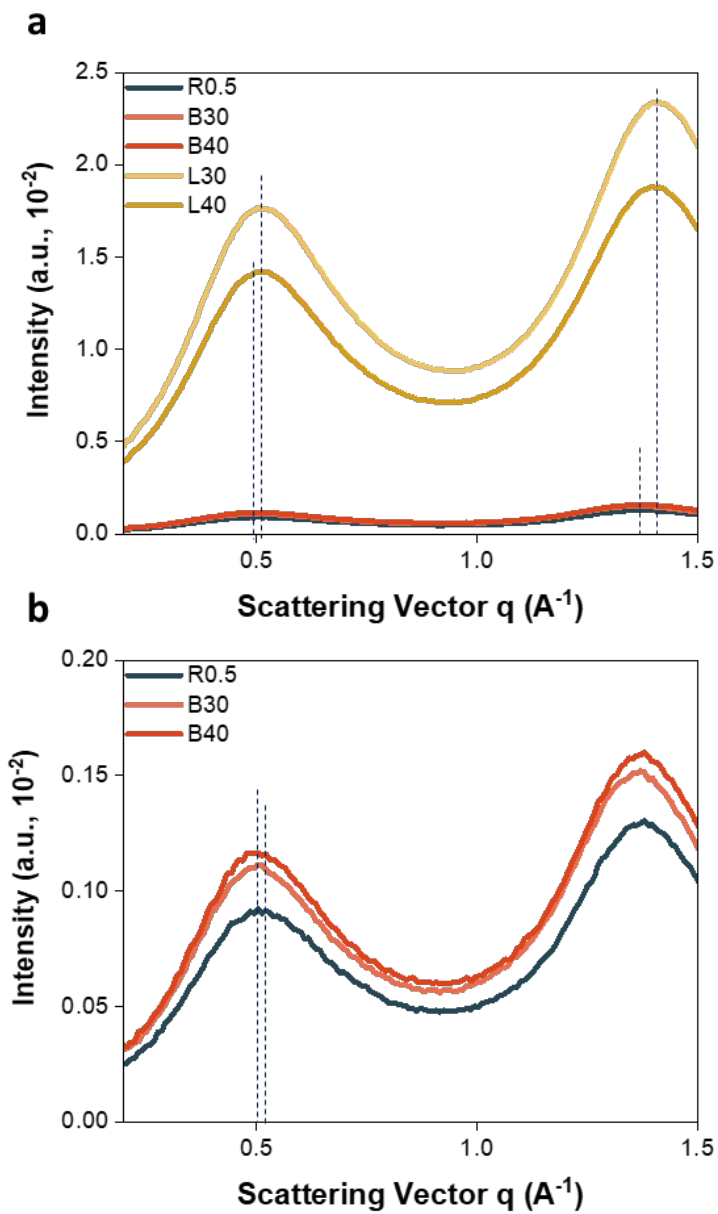


Figure 3-10. a) WAXS data of the homogeneous (R0.5), microphase separated (B30, B40), and macro phase separated PSA (L30, L40). b) Graph scaled from 0 to 0.2

3.2.3. Glass Transition Temperature of Heterogeneous PSAs

The separation of the glass transition temperatures (T_g) is indicated by the splitting of the peaks in the tan delta curve in Figure 3-12 b. The T_g of the PSA measured by the DSC and DMA shear sandwich mode is shown in Table 3-2. Homogeneous PSA of R series showed single T_g ranges from -5.9 to -3.6 °C. Microphase separated PSA manufactured using PIMS, B30 and B40 showed two separated T_g s. Semi-IPN PSA containing crosslinked matrix and linear PBA96 also showed two separated T_g s. The T_g of the crosslinked matrix showed an increase when the PBA was blended (L40) because the soft PBA moved and deformed first to the oscillation of the external force. On the other hand, when PBA is not simply blended but rather covalently bonded to the matrix (B40), the polymer chains are more interconnected, resulting in better transmission of forces through the PBA blocks. Consequently, the mobility of the crosslinked matrix is reduced, requiring greater force to induce movement. This ultimately led to a significant increase in T_g of crosslinked matrix. The separation of glass transition temperature is evidence of phase separation.

Only the low-temperature portion of the two T_g was detected by DSC. Typically, the T_g measured by DSC is lower than that of DMA. The value measured with DSC in this research is about 40 °C lower than that of DMA, but the trend was maintained. Shown by b in Figure 3-12, the high temperature T_g peak of the PIMS PSA is very broad, indicating a wide molecular weight distribution. Since it contains a wide variety of structures, it is likely that the T_g of the structure was not detected by the DSC method.

Table 3-2. T_g (°C) measured with DSC and DMA shear sandwich mode.

| | DSC | DMA Shear Sandwich | |
|-------|-------|--------------------|------|
| R0 | -43.7 | -5.9 | - |
| R0.05 | -43.4 | -4.7 | - |
| R0.1 | -43.1 | -4.6 | - |
| R0.3 | -42.6 | -5 | - |
| R0.5 | -42.2 | -3.6 | - |
| B30 | -43.8 | -4 | 52.7 |
| B40 | -44.2 | -3 | 53.8 |
| L30 | -45.8 | -7.6 | 9 |
| L40 | -44.8 | -7.7 | 9.8 |

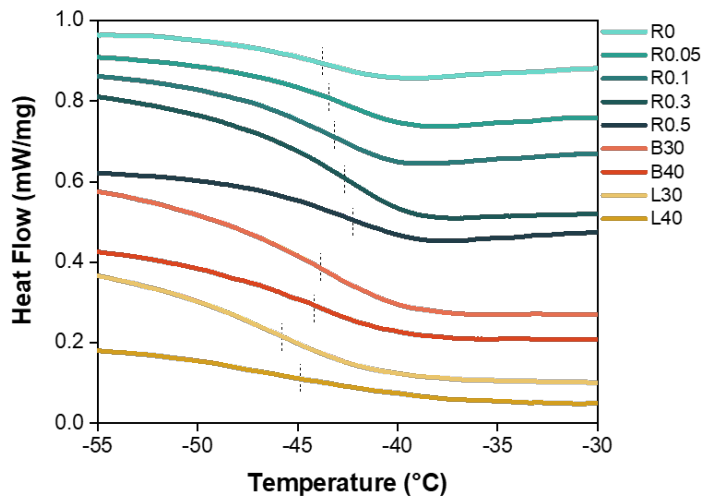


Figure 3-11. Heat flow curves of homogeneous (R), microphase separated (B30, B40), and macro phase separated PSA (L30, L40) measured by DSC measurements.

3.3. Rheological Properties according to Heterogeneous Structure

3.3.1. Rheological Properties

The appearance of a rubbery plateau at high temperature is the result of entanglements or crosslinks. Both the width of this region as well as the property values in this region depend on the molecular weight between entanglements (M_e) or crosslinks (M_c). In Figure 3-12 a, PIMS PSA (means B30 and B40) exhibits a low rubbery plateau modulus, indicating a low pseudo-equilibrium elastic modulus of the network. In other words, according to equation below (Ferry, 1980), the M_c is high.

$$M_c = RTd / G'_{\text{rubbery}}$$

At high temperature, in the R series, an increase in crosslinking density led to an increase in G'_{rubbery} . However, for L30 and L40, their G'_{rubbery} were lower than that of R0.5, with B40 having the lowest G'_{rubbery} . In the case of L30 and L40, where there is free PBA chain, they exhibited lower moduli below 0 °C.

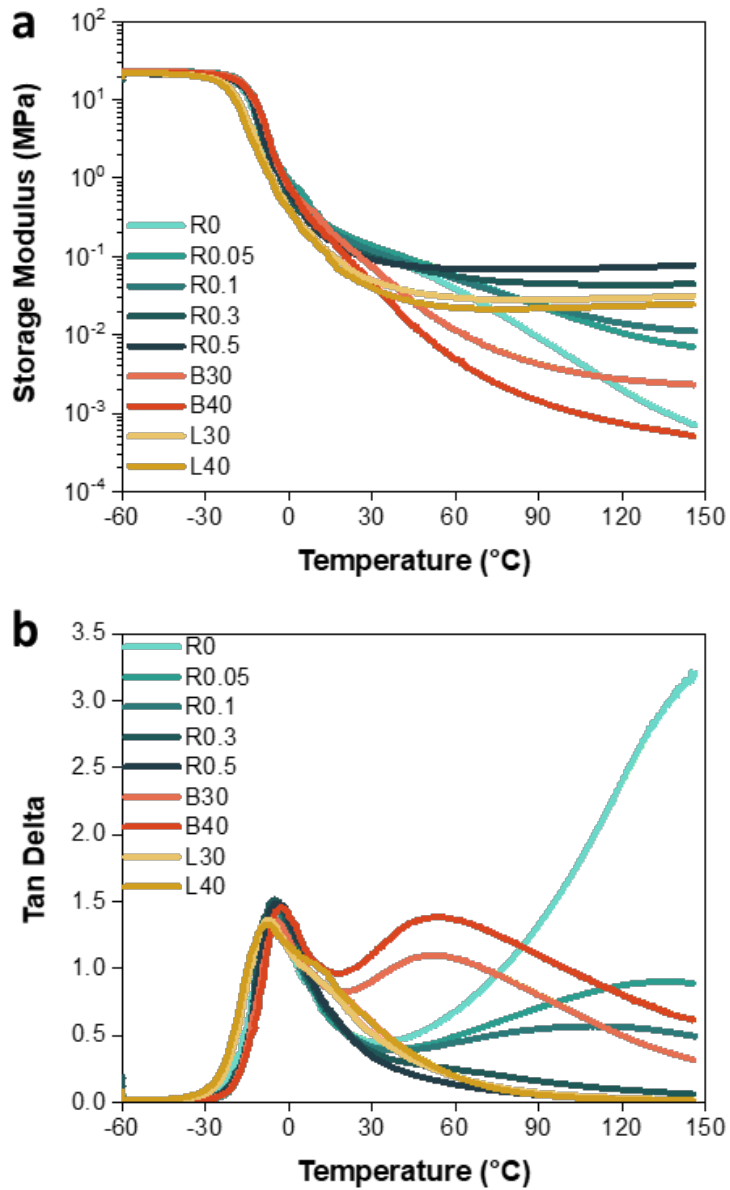


Figure 3-12. a) Storage modulus and b) tan delta curves of homogeneous (R), micro phase separated (B30, B40), and macro phase separated PSA (L30, L40), measured by temperature sweep test.

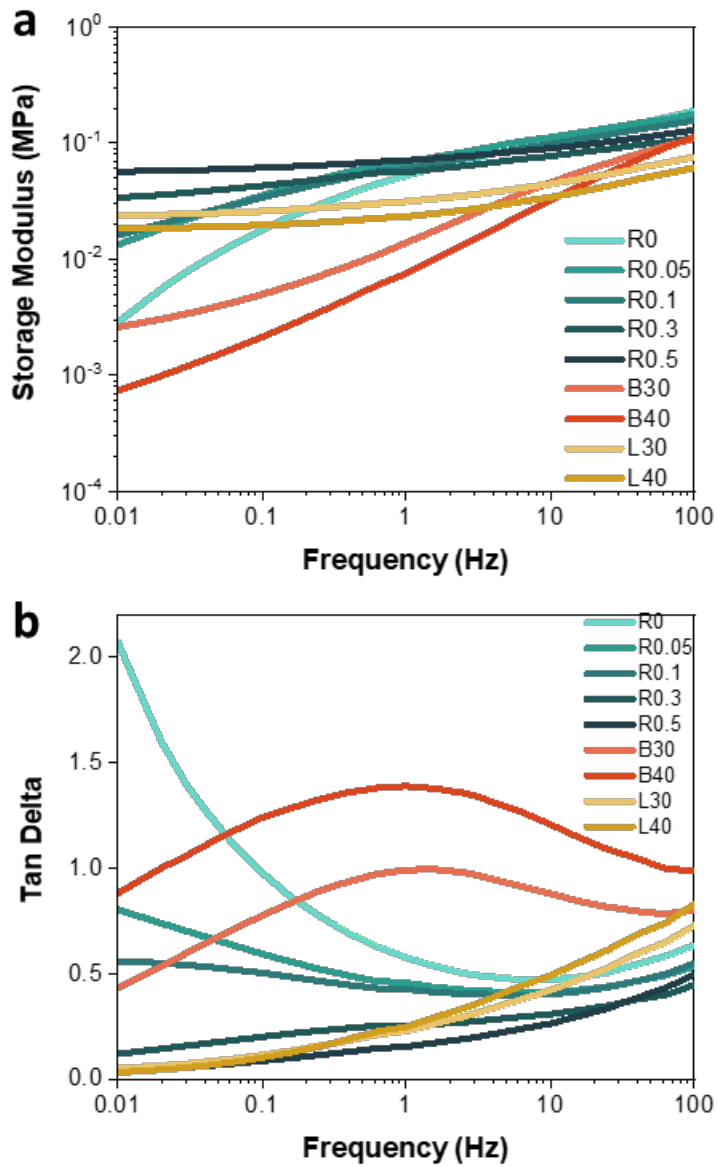


Figure 3-13. a) Storage and b) tan delta curves of homogeneous (R), micro phase separated (B30, B40), and macro phase separated PSA (L30, L40), measured by frequency sweep test.

3.3.2. Tensile Test

The tensile test results revealed a trend in the homogeneous copolymer series R, where an increase in the crosslinking density led to increased hardness and brittleness. R0 exhibited weak and substantial elongation with easy plastic deformation, while R0.3 had the highest tensile strength and R0.5 had the highest Young's modulus and the shortest elongation at break.

In contrast, the heterogeneous PIMS PSA (B30 and B40) exhibited an entirely different behavior compared to the homogeneous R series. When compared to R0.5 which have the exact same composition, PIMS PSA showed higher elongation at break and a lower Young's modulus. The crucial point here is the significantly long strain at the elastic limit, indicating that linear elastic deformation occurs without plastic deformation. These differences in properties are thought to originate from the heterogeneous molecular structure of PIMS PSA.

PIMS PSA consists of a crosslinked rigid matrix that barely moves and a soft PBA domain that is covalently bonded. When subjected to external forces, the PBA domain undergoes a chain conformational change, extending and moving first. This deformation is not a plastic deformation involving chemical bond breaking but rather an elastic deformation restored by the entropy elasticity of polymer due to the conformational change in the chain. The crosslinked matrix maintains the original structure of the material without breaking, allowing the extended PBA to easily return to its original state through entropy elasticity. Additionally, the characteristic high M_c of PIMS PSA is thought to increase chain entanglement at the long chain ends, making PBA's structure even more elastic than linear state.

Semi-IPN PSA (L30 and L40) lacks connections between linear PBA and the crosslinked matrix. Therefore, despite PBA moving first, without supportive

crosslinking points, the material can easily undergo destruction. The force applied to the matrix cannot be efficiently transmitted through PBA, leading to simultaneous plastic deformation and destruction of the matrix. As a result, semi-IPN PSA exhibited lower tensile strength and elongation compared to Homogeneous PSA.

3.3.3. Cycle Test

The experiment involved cyclically applying deformation up to 300% strain and then returning the material to its original state. For PIMS PSA (B40), deformation strain within the elastic limit, as indicated by the linear curve, did not truly experience plastic deformation. The calculated energy dissipation during the cycles was nearly negligible. While L40 and R0.5, both sharing the same composition with B40 but having different polymer structure, fractured when subjected to 300% strain.

The experiment with R0.1, having a suitable modulus to prevent fracturing, showed that some covalent bonds broke during each cycle, leading to plastic deformation and energy dissipation. This indicates that despite having the same composition as homogeneous PSA, the PSA designed with a heterogeneous molecular structure of microphase separation exhibited excellent recovery performance.

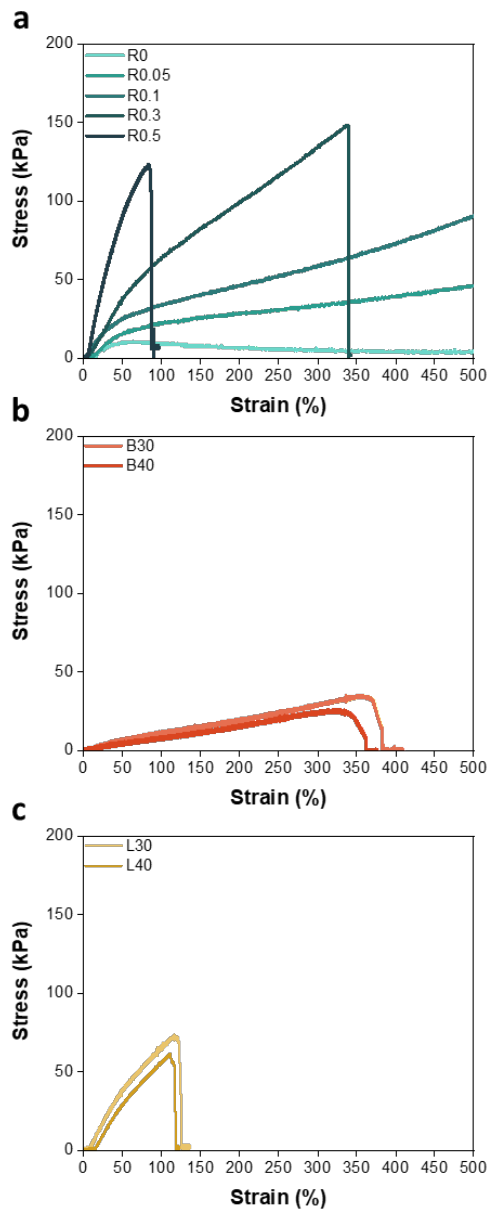


Figure 3-14. Stress-strain curve of tensile test. a) Homogeneous PSA (R), b) micro phase separated PSA (B30, B40), and c) macro phase separated PSA (L30, L40).

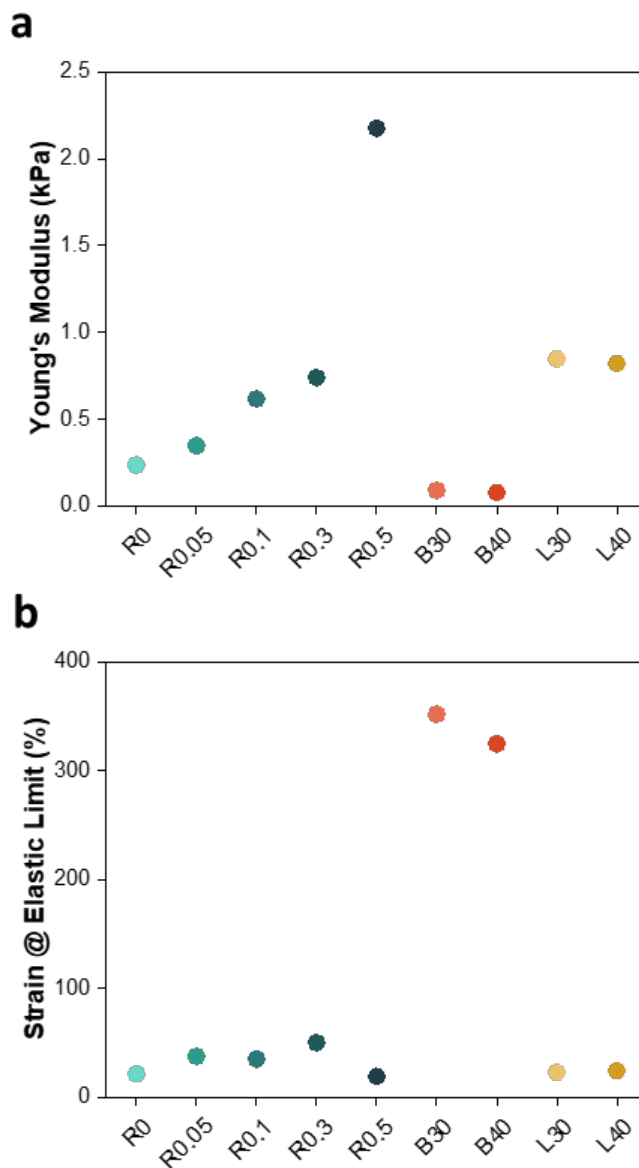


Figure 3-15. a) Young modulus and b) strain at elastic limit of homogeneous PSA (R), micro phase separated PSA (B30, B40), and macro phase separated PSA (L30, L40).

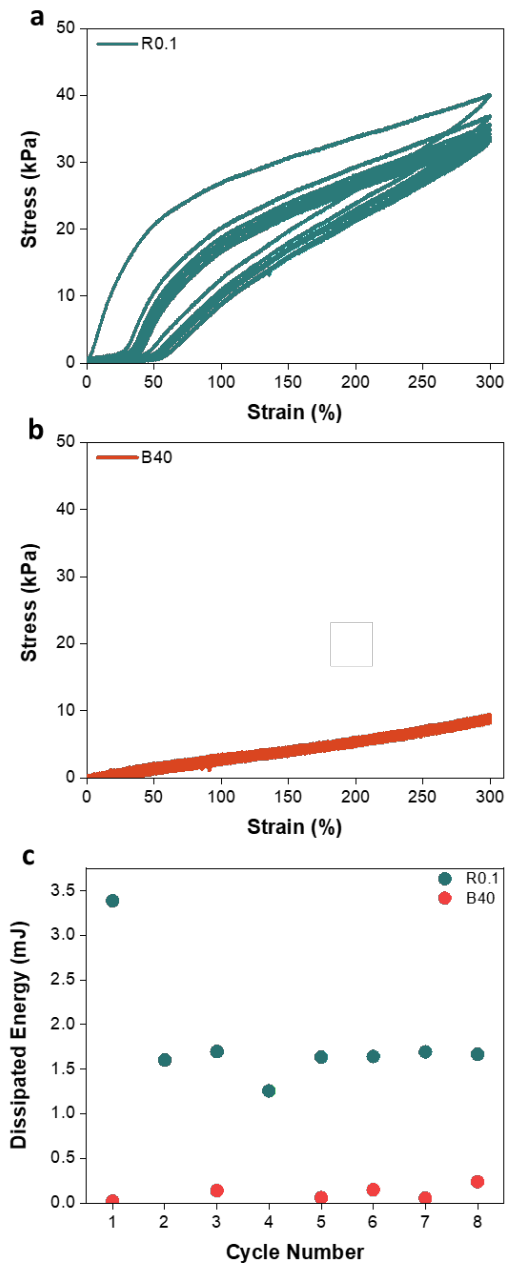


Figure 3-16. Load and unload stress-strain curves of a) R0.1, b) B40, c) Net dissipated energy per each cycle.

3.4. Mechanical Properties according to Polymer Network Structure

3.4.1. Stress Relaxation Test

The excellent recovery capability of B30 and B40 is well evident in the stress relaxation test. These samples demonstrated superior strain recovery of over 96%. In the stress curve, not only was the initial stress very low, but the stress dissipation was also minimal. This is a highly favorable result when compared to the L series, which experiences destruction, or the R series, which has strain recovery of less than 76%. In the case of R0.3, strain recovery exceeds 91%, but its peel strength is very low, making it difficult to apply as a PSA.

The increase in crosslinking density leads to a well-known trade-off relationship: as crosslinking density increases, wetting decreases, causing a reduction in adhesive properties, while bulk cohesion increases, leading to enhanced recovery properties. PIMS PSA represents a new development strategy to overcome these longstanding challenges.

3.4.2. Adhesion Properties

The R sample showed a decrease in wetting with increasing crosslinking density, resulting in lower peel strength. Comparing samples with the same composition, the B30 and B40 samples showed better adhesive properties than R0.5, breaking the problematic inverse correlation between recovery performance and adhesive properties. The PIMS-made heterogeneous PSA achieved both excellent recovery and adhesive properties.

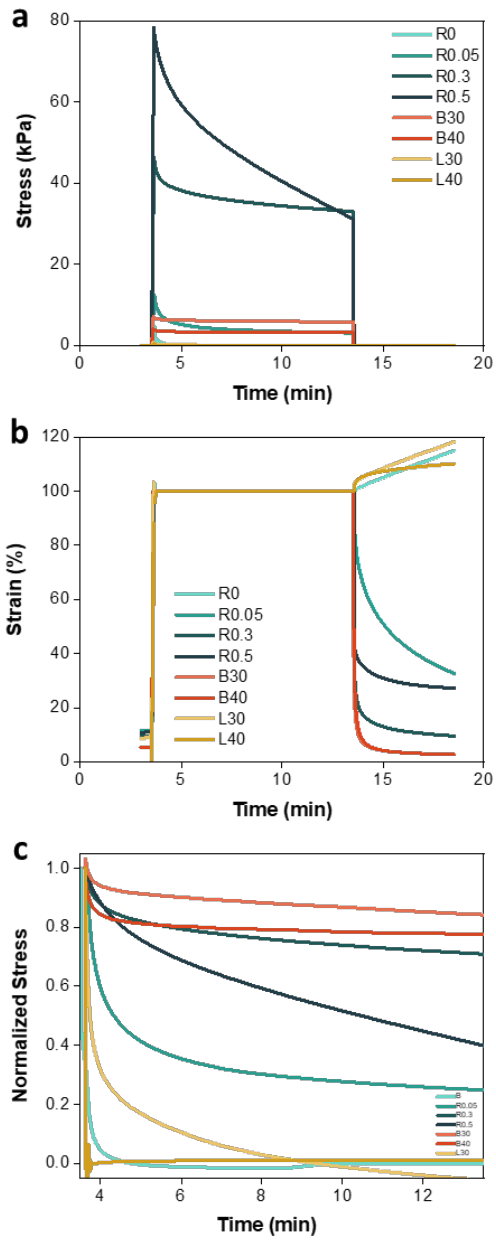


Figure 3-17. a) Stress relaxation, b) strain, c) normalized stress curve of the PSAs.

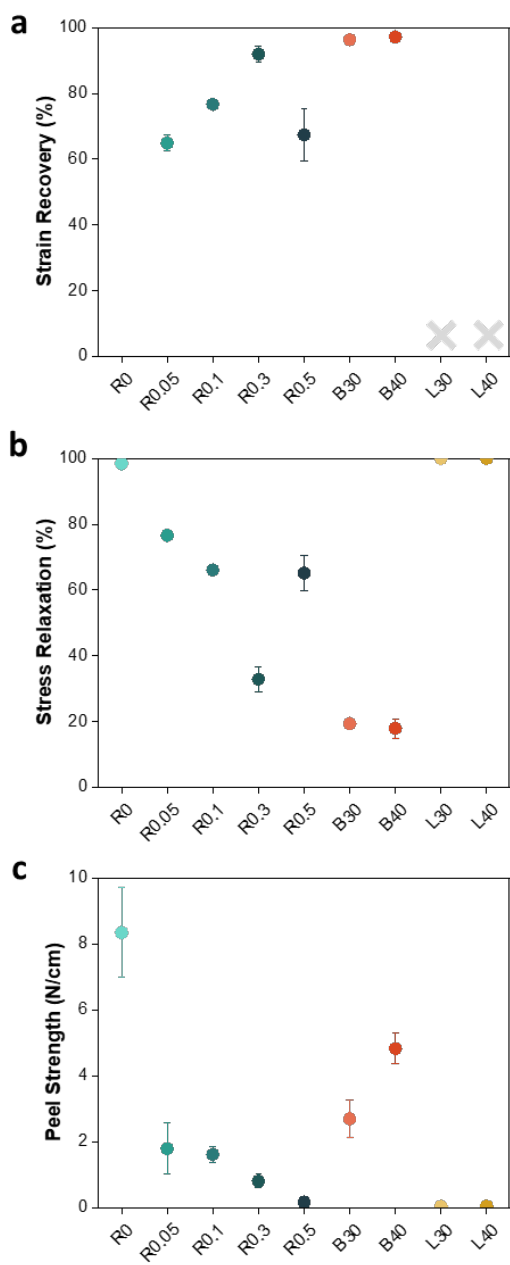


Figure 3-18. Calculated values of a) strain recovery and b) stress relaxation properties, c) Peel strength of PSAs.

4. Conclusions

Utilizing PIMS, we have successfully manufactured micro phase separated heterogeneous PSAs. PIMS PSAs exhibited remarkable properties including very low modulus, elongated elastic region, excellent recovery properties, and superior adhesive properties, despite having the same composition as homogeneous materials. The fact that these distinct properties emerged solely from changes in chemical structure, while maintaining the same composition, holds significant significance in the field of PSA material research.

This dramatic improvement in properties is not due to the presence of linear PBA in the matrix. L30 and L40 samples with blended inert PBA chains did not show a significant improvement in properties. This study is the first to fabricate heterogeneous PSA by using PIMS and provides clues to solving the long-standing challenge of PSA properties for application of flexible displays.

Chapter 4

*Influence of PBA Chain Length of
Polymerization-Induced
Microphase Separated PSA
on Molecular Structures and Properties.*

1. Introduction

Today, PSAs for flexible displays require high adhesion property along with high elasticity. This has been difficult to achieve by conventional method for modifying the properties of PSAs, leading to the need to design new networks. Polymer structures that contain a large amount of short chains, such as bottle brush polymers, can be expected to have a lower modulus, which allows for excellent stretching, and improved adhesion due to better wettability to the substrate. The network structure of a polymer is the underlying principle of the materials properties. Depending on how the polymer structure is designed, materials with the same composition could have a wide range of controlled properties.

In our previous work, we utilized PIMS to fabricate highly elastic, highly adhesive materials. PIMS PSA has a network structure with PBA chains covalently attached to chain ends of the crosslinking matrix. The excellent properties of PIMS PSA are attributed to the absorption of by the free conformational change of the soft PBA blocks and the excellent elasticity of the organically crosslinked and entangled matrix. The size and extent of the micro phase separation domains of PIMS PSA and the physical entanglement of the linear PBA can act as controlling factors for the expression of adhesive material properties and are influenced by the chain length of the PBA blocks present in the network. Therefore, in this study, we studied the effect of micro phase separation morphology such as soft domain size and physical entanglement of linear chains on the properties by varying the chain length of PBA comprising Macro-CTA, which is a precursor to PIMS. Through this study, we identified the mechanisms that control the properties of adhesive films depending on the PBA chain length and understood the most desirable network design direction to express the excellent properties for flexible displays.

2. Experimental

2.1. RAFT Polymerization of Macro CTA with M_n Variation

After removing the inhibitor of BA using neutral aluminum oxide, the exact amount of BA, BTPA, and AIBN were added to acetonitrile. The amount of BTPA was adjusted according to the target DP of PBA. The amount of BTPA was calculated by dividing the amount of BA monomer by the target DP. AIBN and BTPA were mixed in a 1:10 ratio. The reaction mixture was sealed with a septum before being stirred at 300 rpm and sparged under nitrogen for 60 min. The mixture was polymerized for 15 h at 60 °C. The reaction was stopped by cooling inside a freezer (-20 °C) and exposing to air. The polymer solution was concentrated by rotary evaporation and used without further purification.

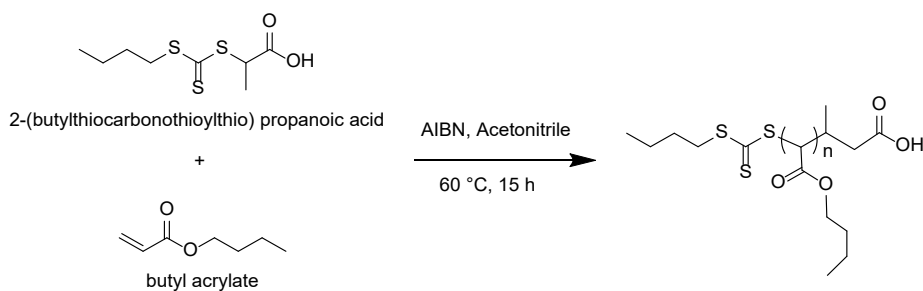


Figure 4-1. RAFT polymerization of Macro CTA with M_n variation. $n = 70, 80, 100, 200, 1000, 2000, 8000$.

2.2. Preparation of the PIMS PSA Specimens

Micro phase separated PSA was prepared by chain extension of Macro CTA with acrylic monomer and PEGDA initiated with TPO. Macro CTA was dissolved in BA and AA monomer, then TPO was added. The reaction mixture was mixed for 2 min with 2000 rpm, and then defoamed for 2 min, 2000 rpm. The mixture is coated between release films, and then irradiated with a UV light (mercury lamp, 20 mW/cm², main wavelength 365 nm) for 10 min. Finally, a crosslinked acrylic polymer network to which PBA₉₆ blocks were covalently bonded was obtained. As such, micro heterogeneous PSA was prepared using PIMS, which induces micro phase separation simultaneously with chain extension and crosslinking reactions of the polymer.

To achieve the intended structure, the chain extension reaction of BTPA only extends one chain due to differences in bond energy. The radical stabilization energy (RSE) of $\cdot\text{CH}(\text{CH}_3)\text{COOH}$ secondary radical present in BTPA is 41.3 kJ/mol, substantially exceeding the RSE of the butyl group at 13.5 kJ/mol, rendering it dominant in separation and facilitating unidirectional propagation reaction (Shanmugam, et al., 2018). In the case of the propagation chain, the RSE of the acrylic radical is about 42 kJ/mol, resulting in sole unidirectional propagation (Hioe, et al., 2010).

Table 4-1. Compositions of bulk mixtures applied to cast the PIMS PSAs (mol%)

| | BA | AA | PEGDA | PBA _n -CTA | TPO |
|-------|----|----|-------|-----------------------|-----|
| B70 | 55 | 5 | 0.5 | 0.57 | 0.5 |
| B80 | 55 | 5 | 0.5 | 0.5 | 0.5 |
| B100 | 55 | 5 | 0.5 | 0.4 | 0.5 |
| B200 | 55 | 5 | 0.5 | 0.2 | 0.5 |
| B1000 | 55 | 5 | 0.5 | 0.08 | 0.5 |
| B2000 | 55 | 5 | 0.5 | 0.04 | 0.5 |
| B8000 | 55 | 5 | 0.5 | 0.01 | 0.5 |

2.3. Characterization

NMR, GPC, WAXS, DSC, DMA, and tensile test were measured in accordance with the procedures detailed in Section 2.6. of Chapter 3.

2.3.1. Transmission Electron Microscope (TEM)

Ultrathin sections (60 nm) of PSAs were micro-sectioned at cyro temperature using ultramicrotome (Powertome, RMC). Sections were picked up on 400 mesh uncoated copper grids and stained with the vapor from a ruthenium tetroxide (RuO_4) metal solution for 1 times for 1 h. TEM measurement were carried out in the bright field mode on energy-filtering transmission electron microscope (JEM-ARM 200F, NEOARM).

2.3.2. Stress Relaxation Test

DMA (Q800, TA Instruments, USA) in the tension film mode was used to evaluate the strain recovery and stress relaxation properties of the PSA sheet. The specific method is described in Section 2.6. of Chapter 3. Stress relaxation properties were measured at $-20\text{ }^\circ\text{C}$, $25\text{ }^\circ\text{C}$, and $60\text{ }^\circ\text{C}$ each.

2.3.3. Adhesion Property

Based on ASTM D3330, the bonded specimens were prepared as 25 mm wide and $60\text{ }\mu\text{m}$ thickness samples to measure the 180 ° peel strength using a Texture Analyzer. The specific method is described in Section 2.1.5. of Chapter 2. For measuring the peel strength of $60\text{ }^\circ\text{C}$, UTM(Z010, Zwick) was used and the specimens were placed in $60\text{ }^\circ\text{C}$ for 10 min and then tested.

2.3.4. Swelling Test

The gel content and molecular weight between crosslinking of polymer networks was calculated by swelling in acetone at room temperature for 24 h, followed by drying in an oven at 60 °C for 24 h.

2.3.5. Folding Test

A dynamic folding test was used to evaluate the folding stability of the prepared PSAs. The samples were developed with respect to the actual folding display structure (Figure 4-5), which is widely used in the folding display industry (Campbell, *et al.*, 2017). In this sample setup, clear polyimide (CPI, 50 µm) and yellow polyimide (PI_f, 50 µm) films were used, and our PSA were positioned between the CPI and yellow polyimide (PI_f) films. The size of the test specimen was 160 mm x 20 mm. The following autoclaving conditions were used for reducing air bubbles of laminated PSA: equipment (L-series, M tool), temperature (50°C), pressure (5 bar) and time (40 min).

Customized equipment (Foldy-200, FlexiGO) was used to perform the dynamic folding test (Figure 4-6). Folding was performed in the in-fold direction and the frequency/bending radius was set to 0.5 Hz/1.5 mm. Three different test conditions were used to evaluate the folding stability as follows;

- Room temperature: 25 °C, 200,000 cycles
- Low temperature: -20 °C, 30,000 cycles
- High temperature/high humidity: 60 °C/93 %RH, 50,000 cycles

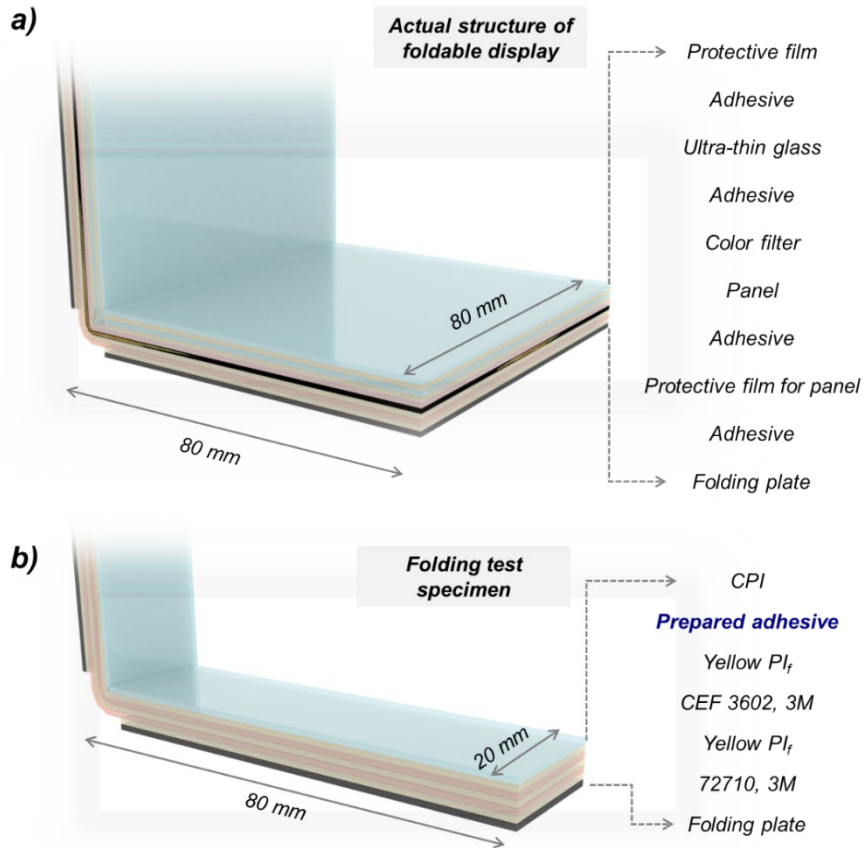


Figure 4-4. Structure of a) the actual foldable display and b) the test specimen used for folding test (Back, *et al.*, 2022).

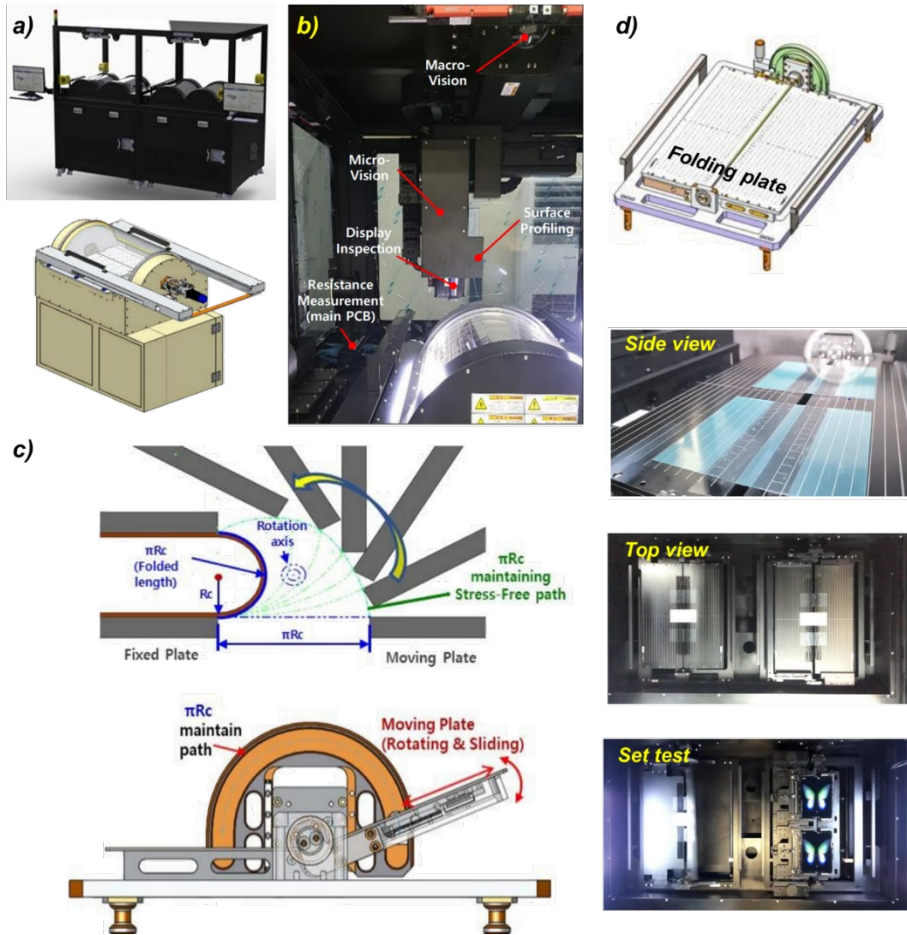


Figure 4-5. a) Outside and b) inside view of the equipment for the dynamic folding test. c) Scheme for the in-fold test procedure. d) Pictures of the folding plate (w/o specimen, side view, top view, and set test view) (Back, *et al.*, 2022).

3. Results and Discussion

3.1. Results of Synthesis and Polymerization

3.1.1. Synthesis of 2-(butylthiocarbonothioylthio) Propanoic Acid

The yield of the synthesized 2-(butylthiocarbonothioylthio) propanoic acid was 82.1%. The chemical structure was defined by the ¹H-NMR spectrum (Figure 3-6). It was confirmed that the starting materials, 2-bromopropanoic acid, and butanethiol did not exist in the compound through the absence of doublet near 1.92 ppm (corresponding to methyl group of 2-bromopropanoic acid), and triplet near 2.53 ppm (corresponding to methylene of butanethiol). The analysis of the NMR spectrum is as follows. The NMR spectrum of the synthesized compound is omitted in this chapter.

3.1.2. Synthesis of Macro-CTA

Macro CTA with a PBA chain length variation was synthesized using RAFT polymerization. The chemical structure was defined by the ¹H-NMR spectrum. NMR spectra of Figure 4-7 normalized by a resonance at 4.03 ppm. The degree of polymerization (DP) of PBA-CTAs was calculated based on the integral value at 4.05 ppm (the peak a in Fig. 4-7). Molecular weight (MW) was calculated by using equation of $MW(\text{PBA-CTA}) = DP(\text{PBA}) \times MW(\text{BA}) + MW(\text{BTPA})$. DP and MW of the macro-CTA was summarized in Table 4-2.

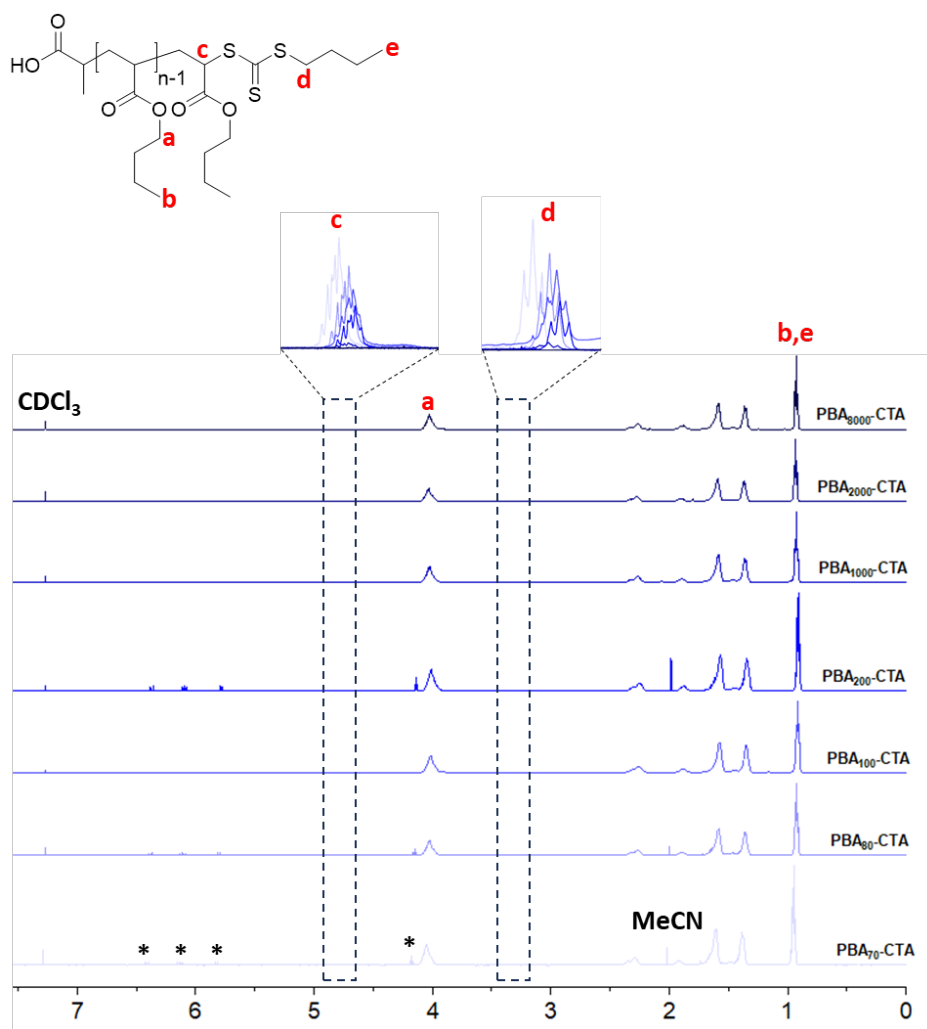


Figure 4-6. NMR spectra of RAFT polymerized PBA_n-CTAs. *: residual BA monomer. The spectra normalized by a resonance at 4.03 ppm.

Table 4-2. Characterization of macro-CTAs synthesized by RAFT-mediated polymerization of butyl acrylate in acetonitrile. Round the number to the nearest hundred.

| | DP | M_n (g/mol) |
|--------------------------|-----------|---------------------------------|
| PBA ₇₀ -CTA | 70 | 9,800 |
| PBA ₈₀ -CTA | 90 | 12,100 |
| PBA ₁₀₀ -CTA | 100 | 13,200 |
| PBA ₂₀₀ -CTA | 200 | 28,000 |
| PBA ₁₀₀₀ -CTA | 1,000 | 132,800 |
| PBA ₂₀₀₀ -CTA | 1,800 | 237,300 |
| PBA ₈₀₀₀ -CTA | 8,200 | 1,053,600 |

3.2. Morphology of Heterogeneous PSA

3.2.1. TEM

To obtain a clear visual image that would allow us to see the change in morphology along the length of the PBA chain, we changed our methodology for precise TEM measurements. Microtome was performed at cryo-temperature to ensure proper flaking of the soft PSA sample, and metal staining was performed using vapor. We were able to obtain high-resolution images with STEM.

The STEM images taken are shown in Figures 4-8 and 4-9. The AA rich phase appears dark and the PBA rich phase appears light because the staining metal molecules chelate with acrylic acid and are located near the AA. The R sample, which contains no PBA domains, also showed an even distribution of light and dark areas in the TEM images. The B80 sample prepared with PBA80-CTA starts to show a PBA rich bright domain. The PBA rich phase is dense, with many small stems, and is distributed over the entire area of the material. These PBA rich domains become progressively thicker and more interconnected as the length of PBA-CTA used increases from 80 to 8000. The presence of these distinct light and dark domains provides strong evidence for the microphase separation of PIMS PSA in the TEM images. In the case of B100, which is unique among hetero-PSAs, the PBA does not appear to form its own stems, but instead fuses with the matrix throughout the material.

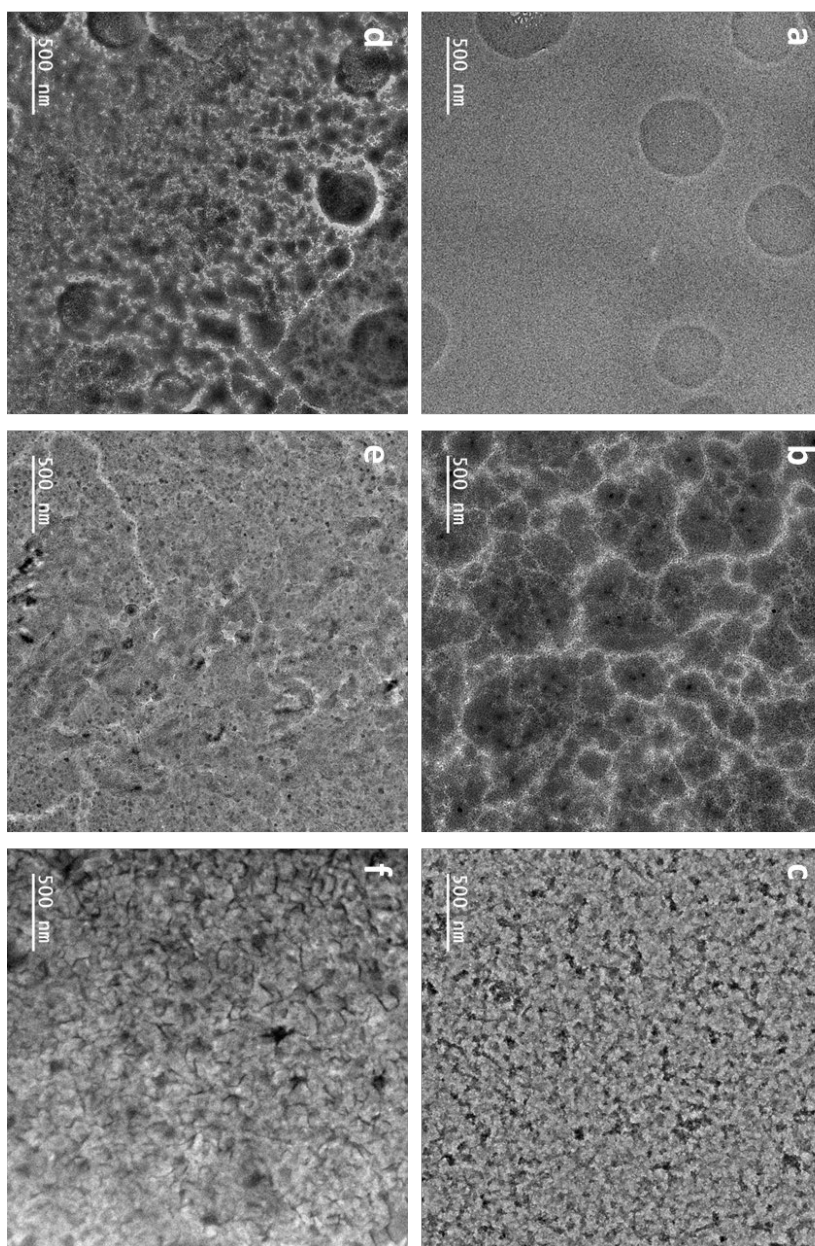


Figure 4-7. STEM images of a) homogeneous PSA and PIMS PSA samples prepared with b) PBA₈₀-CTA, c) PBA₁₀₀-CTA, d) PBA₂₀₀-CTA, e) PBA₂₀₀₀-CTA, f) PBA₈₀₀₀-CTA. (Magnification: 10k)

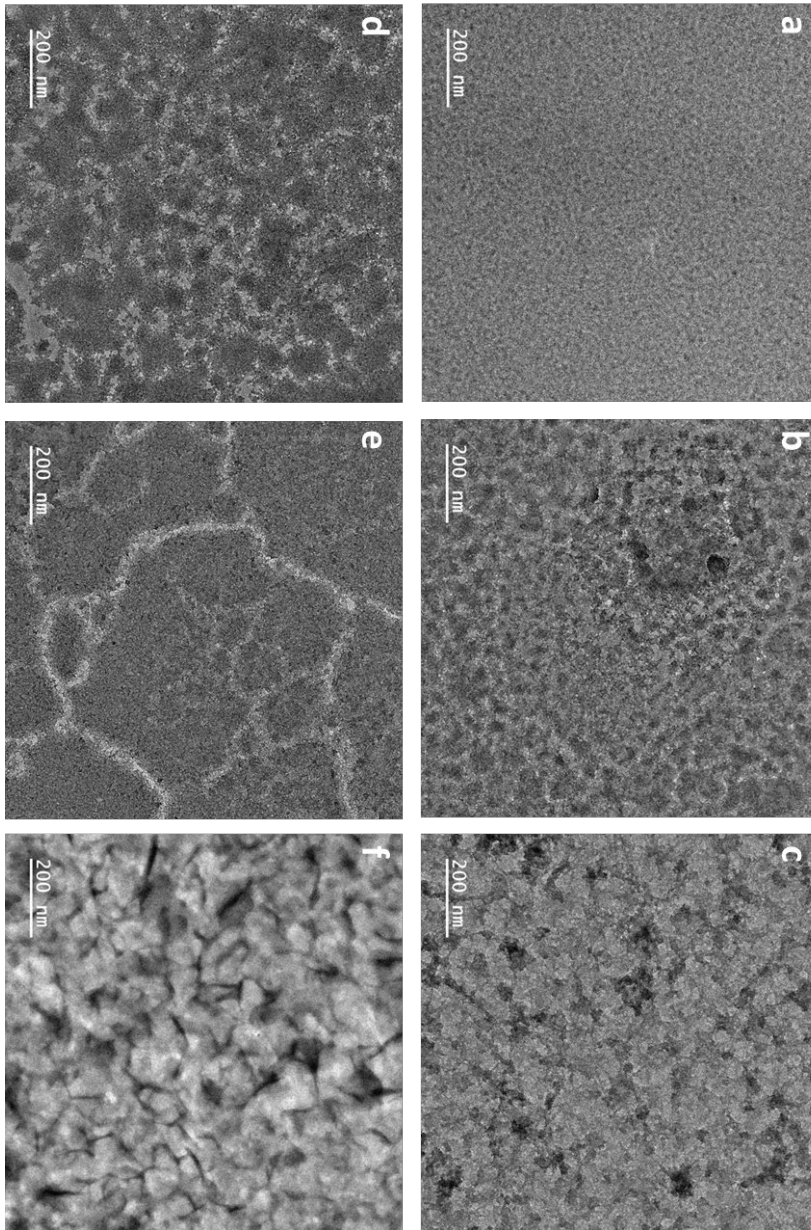


Figure 4-8. STEM images of a) homogeneous PSA and PIMS PSA samples prepared with b) PBA₈₀-CTA, c) PBA₁₀₀-CTA, d) PBA₂₀₀-CTA, e) PBA₂₀₀₀-CTA, f) PBA₈₀₀₀-CTA. (Magnification: 25k)

The images have been analyzed using the Image J software for TEM images at a magnification of 25k. The PBA in the material is not contained in the R sample and 40% in the PIMS samples. Therefore, based on the brightness, a threshold of 40% was set as the area corresponding to PBA. The structures that could be identified within the set area were analyzed and the size and length of the PBA domains in each image and the distance between the PBA domains were measured. The processed image is shown in Figure 4-10. The measured quantitative morphology values are shown in Table 4-2.

In the previous study (Bobrin, *et al.*, 2022), materials containing PBA₂₄ or PBA₄₈ showed globular domains, elongated domains with PBA₉₄, and bicontinuous morphology with PBA₁₈₀ and above. In this study, unlike previous studies, the crosslinked matrix contains both BA and AA, so the difference in the interaction parameters of PBA and crosslinked network is not large. Therefore, it is understood that the two phases have morphological features that are not sharply distinguished.

In addition to visualizing by using TEM, we were able to quantitatively measure the morphological changes of the PBA domains through image analysis. As summarized in Table 4-2, the domain size in the PBA-rich phase did indeed tend to become thicker and longer with increasing PBA chain length. The spacing of the PBA domains also increased, which is consistent with previous studies (Leguizamon, *et al.*, 2021, Shi, *et al.*, 2023).

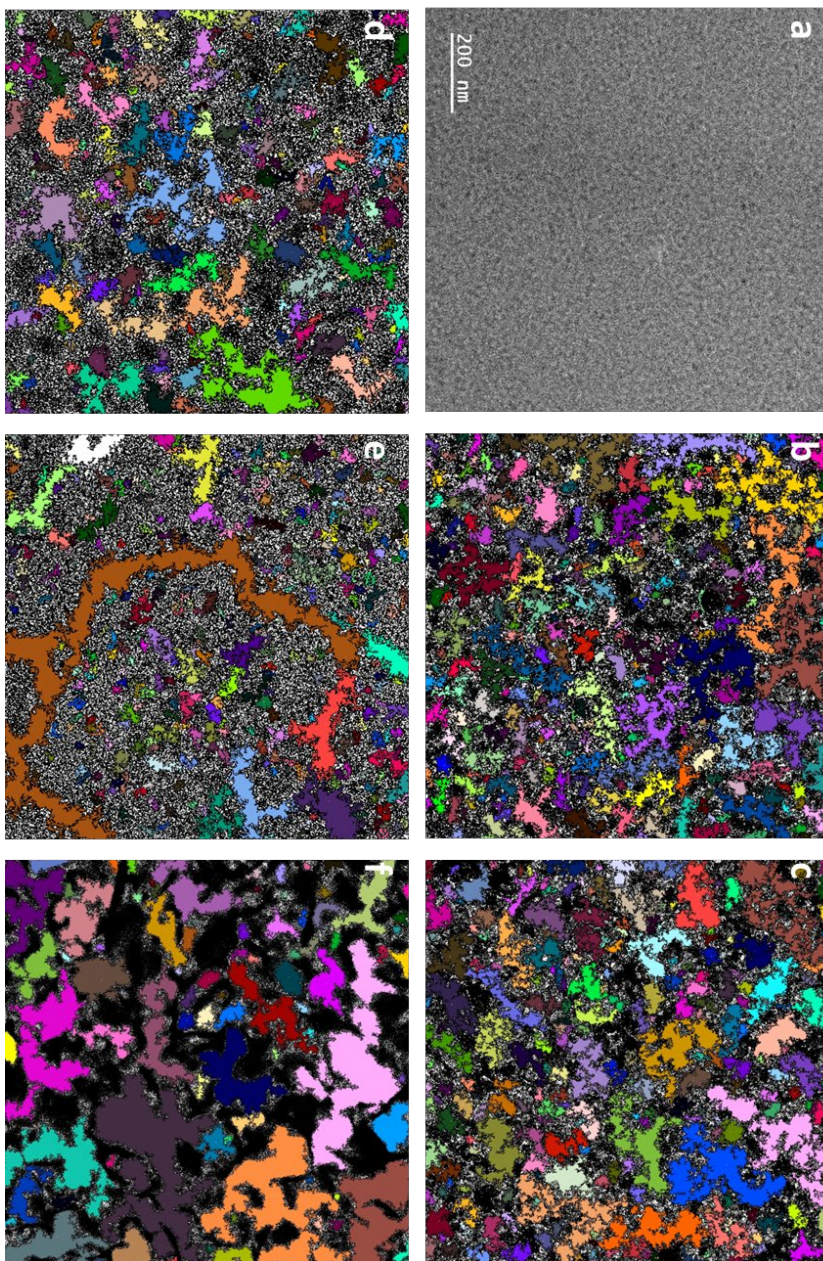


Figure 4-9. STEM images of a) homogeneous PSA and PIMS PSA samples prepared with b) PBA₈₀-CTA, c) PBA₁₀₀-CTA, d) PBA₂₀₀-CTA, e) PBA₂₀₀₀-CTA, f) PBA₈₀₀₀-CTA. (Magnification: 25k)

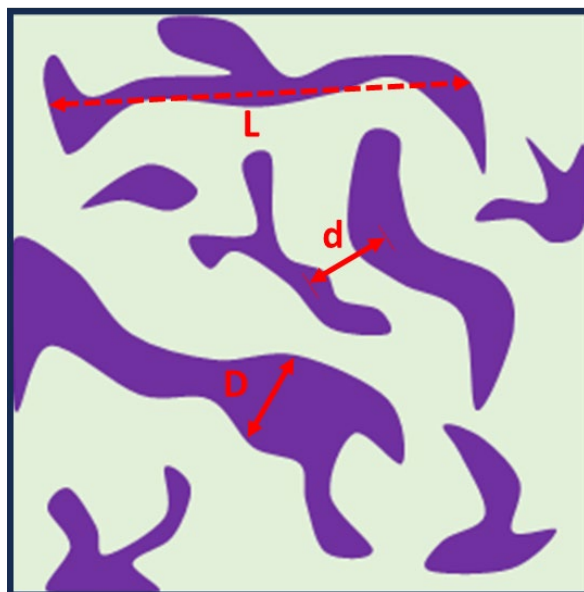


Figure 4-10. Schematic illustration of microphase separated morphology. PBA domains are shown in purple; crosslinked P(BA-stat-AA-stat-PEGDA) domains are shown in green. D_{TEM} : PBA domain width, L_{TEM} : PBA domain length, d_{TEM} : domain spacing.

Table 4-3. Summary of morphology characterization for homogeneous (R) and heterogeneous (B80, B100, B200, B2000, B8000) materials.

| | Morphology | D_{TEM} (nm) | d_{TEM} (nm) | L_{TEM} (nm) | PBA Area (%) |
|-------|-------------------|----------------------------------|----------------------------------|----------------------------------|---------------------|
| R | Homogeneous | - | - | - | - |
| B80 | Bicontinuous | 12 ± 4 | 53 ± 11 | 129 ± 37 | 29 |
| B100 | Bicontinuous | 40 ± 9 | 73 ± 21 | 186 ± 59 | 30 |
| B200 | Bicontinuous | 37 ± 11 | 111 ± 25 | 181 ± 81 | 24 |
| B2000 | Bicontinuous | 46 ± 10 | 126 ± 46 | 234 ± 168 | 22 |
| B8000 | Bicontinuous | 63 ± 20 | 141 ± 37 | 240 ± 96 | 35 |

3.2.2. SAXS and WAXS

TEM confirmed the heterogeneity and morphology of the prepared PIMS PSA. However, SAXS in Figure 4-12 a) showed no peaks indicative of a regular structure. SAXS is suitable for measuring short-range interactions and is a method for detecting density changes in polymers. It is understood that the shape of the polymer network identified by TEM was not measured by SAXS because the material was not etched, so the material was all connected and the density difference between each phase was not large.

On the other hand, WAXS is suitable for long-range interactions and is an indicator of regular molecular arrangement and crystallinity. In the WAXS measurement of Figure 4-12 b), no peaks indicating significant crystallization were observed, but a small increase in the WAXS peak and a shift in the peak position were observed in the B samples compared with R sample. The peak area is generally indicative of the crystal structure and the peak area is an indicator of the degree of crystallinity. As PSA is an amorphous polymer, the increase in the WAXS data indicating the degree of crystallinity is very small, but it can be seen that the degree of regular arrangement of molecules is slightly increased in the B samples compared to the R samples.

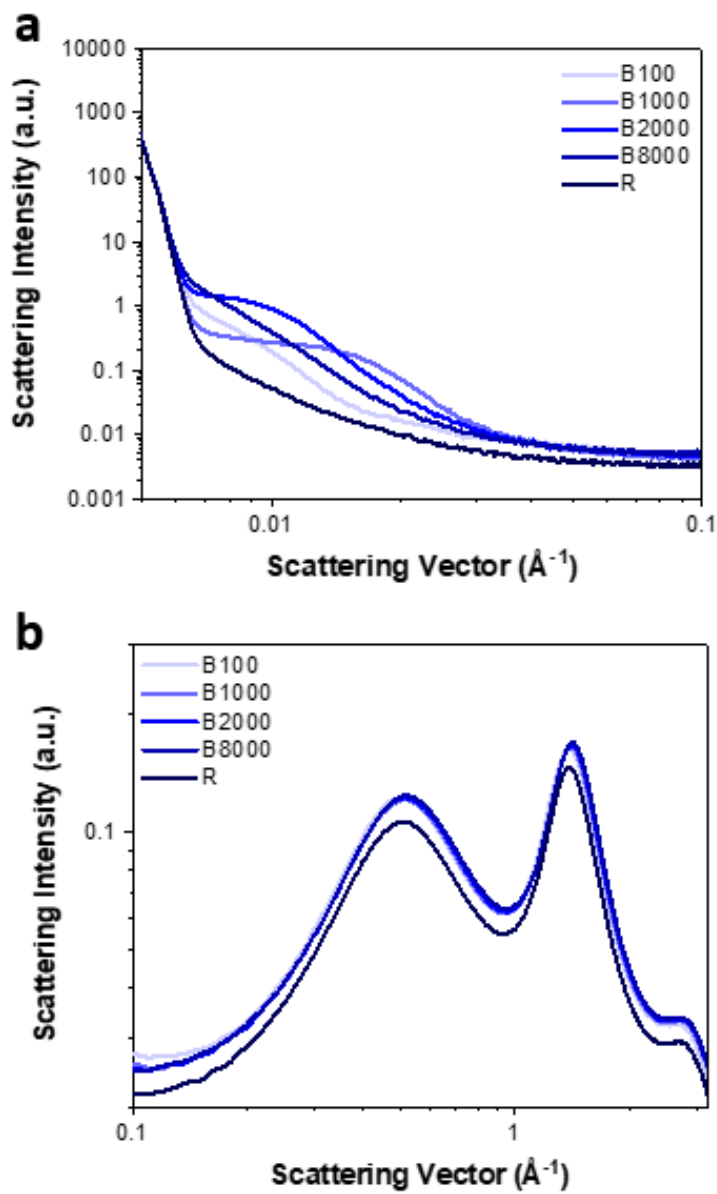


Figure 4-11. Representative a) SAXS and b) WAXS data of PIMS PSA (blue lines) and the homogeneous PSA (black line).

3.3. Rheological Properties according to Heterogeneous Structure

3.3.1. Rheological Properties

The changes in the morphology of the polymer network in PSA that we saw earlier lead to rheological differences. B70 and B80, which do not have a densely connected structure, exhibit a very low storage modulus at high temperatures as the polymer chains slide over each other and deform. As the PBA chain length increases, the high temperature storage modulus increases with increasing the entanglement. For B8000, it reaches storage modulus values similar to the R sample, which forms a fully crosslinked network.

In general, amorphous polymers are disordered random coils at high temperatures and retain their shape as they cool, with a slight decrease in volume. Crystalline polymers form a regular structure that arranges itself in a certain direction upon cooling. Examples of this type of crystallization include chain folding and the formation of lamellae and spheres. Crystalline polymers comprise polyethylene, polypropylene, polyamide, polyester, and polyacetal. These structures consist of small monomers without bulky groups to aid chain packing. The polyacrylic molecules used in this paper are classed as amorphous polymers due to the large size of their monomers, which generally prevents crystallization.

Initially, polyacrylic polymers take the form of amorphous random coils. In this study, we constructed a polymer network comprising long PBA polymers attached to a reticular structure via RAFT polymerization of Macro-CTA. The structure of the materials was verified via WAXS, revealing a minor rise in crystallinity. Utilizing TEM, we could verify the real size of the non-homogeneous domains.

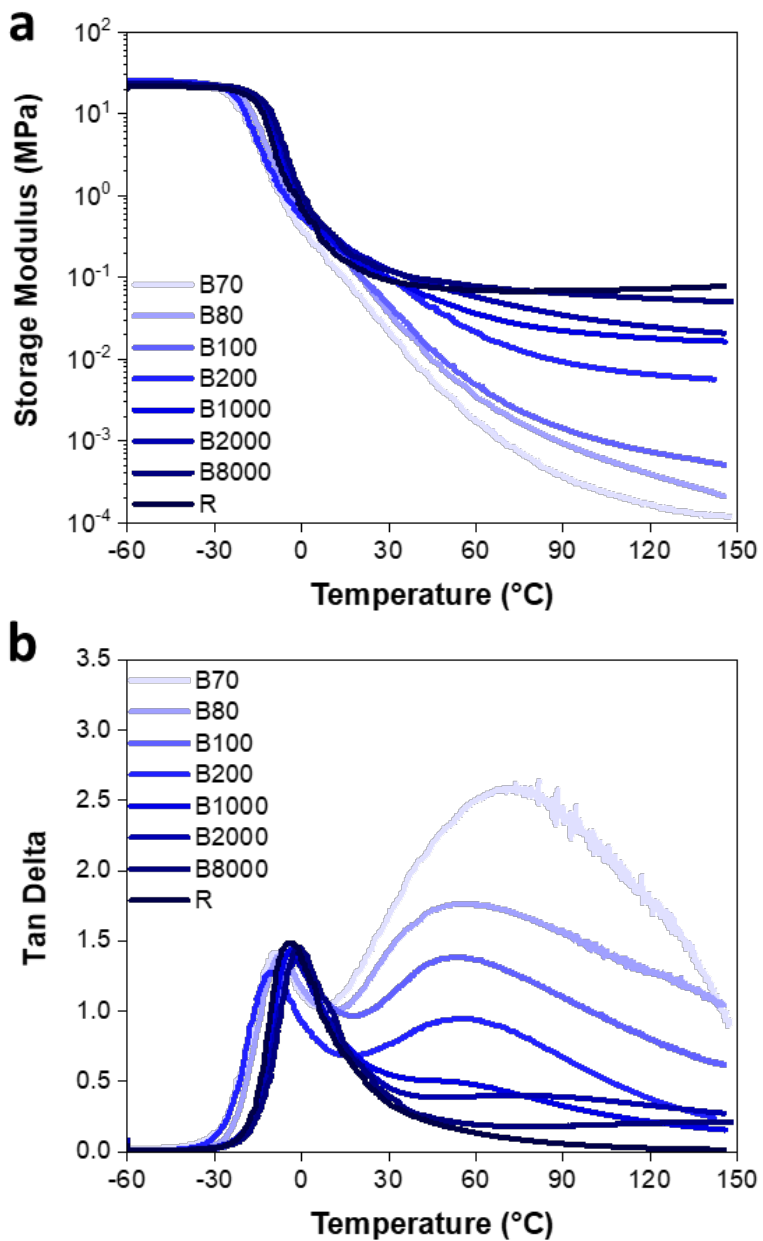


Figure 4-12. Temperature-dependent a) storage modulus and b) loss factor of homogeneous PSA (black line) and PIMS PSA samples (blue lines).

The PSA material, prepared by PIMS, is comprised of reticular networks that are covalently crosslinked and soft PBA domains. This heterogeneous structure resulted in a change in the tan delta value, which is commonly employed as an indicator of glass transition temperature. The response of the material is obtained by the DMA 1 Hz oscillation test with a temperature sweep.

The tan delta graph illustrated a more distinct separation of the peaks and a stronger intensity of the second peak for shorter PBA chain lengths compared to that of longer PBA chain lengths. As the length of PBA increases, the PBA chain becomes more entangled, akin to a long thread. This results in a stiffer PSA with reduced viscosity and damping effect at room temperature. In contrast, shorter PBA lengths lead to greater separation between the matrix and soft domains, revealing rheological properties that exhibit good damping effects at room temperature. The divergence of these tan delta peaks also serves as a reliable indicator of phase separation.

Based on previous studies (Bobrin, *et al.*, 2022, Shi, *et al.*, 2023), the first peak within the tan delta, was likely to be associated with the PBA rich phase, while the second peak was associated with the PBA poor crosslinked matrix phase. The position of the second peak shifts from 70 to 55 °C as DP of PBA block increases, in line with the previous research.

It is evident that the PBA rich phase has a lower glass transition temperature and is more prone to conformational change under external forces and strain. The temperature required for both phases to move is above 60 °C, which surpasses the T_g of the second peak. When repeatedly strained at ambient temperature, the PBA-richest soft phase is likely to be more responsive to strain.

Meanwhile, the area under the tan delta peak depends on the molecular weight distribution. We can also speculate that the crosslinked network structure composed of BA, AA, and PEGDA, which is responsible for the

second tan delta peak, has a wide M_w distribution, including various reticular structures and physically entangled chains.

As the temperature approaches 60 °C, both phases of the material can transition from a glass state to a more viscous behavior within the polymer. Specifically, a shorter chain length of PBA leads to reduced crosslinking and entanglement, resulting in a more viscous, less elastic behavior.

There are various hypotheses as to why a matrix has an exceptionally high T_g . Theory on T_g includes free volume theory, kinetic theory, and thermodynamic theory. Flory-Fox equation below shows the effect of molecular length on T_g .

$$T_g = T_g^\infty - \frac{K}{M_n}$$

If the molecule contains bulky groups that interfere with chain motion, this will be a factor in increasing T_g . The relationship between the copolymerization fraction and the glass transition temperature of a typical copolymer is shown in the Fox equation below, where M_i is the weight fraction of i .

$$\frac{1}{T_g} = \frac{M_1}{T_{g1}} + \frac{M_2}{T_{g2}}$$

The temperature point at which molecular-level flow occurs is called T_g . For flow to occur, a free volume above a certain size is required. The relationship between the melt viscosity of a polymer and its free volume is shown in the WLF equation, where a_T is the shift factor.

$$\log a_T = \frac{-17.44(T - T_g)}{51.6 + T - T_g}$$

In essence, T_g is influenced by both intramolecular chain stiffness and intermolecular interactions. Therefore, despite the lack of stiffness in the chemical structure of the matrix components, the restricted motion of the matrix can result in the high glass transition temperature due to the preferential movement of the PBA chains. Furthermore, given that numerous free chain ends are present in the PBA rich phase, the reticulated network seemingly possesses minimal free volume for movement, thus leading to the appearance of the tan delta peak at elevated temperatures.

3.3.2. Tensile Test

The rheological properties are influenced by the morphology of the network structure and consequently have an effect on the physical properties. B70 and B80, which contain a large fraction of disconnected and fragmented linear chains throughout the material, deform easily with no resisting force from within the material as they are stretched. They stretch easily and undergo plastic deformation as they are stretched. B100 shows linear elastic behavior up to 300% strain. In the range of linearly elastic behavior, it is easy to return to its original state, almost like a spring. This broad range of linear elasticity is evidence of the excellent elasticity and recovery properties of B100. Based on this, we can conclude that B100 has the best level of crosslinking and entanglement for its elastomeric properties. From B200 to B2000, the elongation at break decreases to a level of 200%. The linear elastic region appears below 50%. At strains above 50%, plastic deformation occurs and is not restored. These limits of elongation indicate an excessive degree of crosslinking and entanglement. Interestingly, B8000 exhibits similar Young's modulus and stress-strain curve

with R samples, until R broke at 100% strain. Because B8000 is composed of a combination of crosslinking and entanglement, it exhibits improved elongation and toughness over R, which is mainly composed by crosslinking structure. This is consistent with previous studies (Li, *et al.*, 2022) reporting increased elasticity and toughness of highly entangled networks, as is schematized in the Figure 4-15.

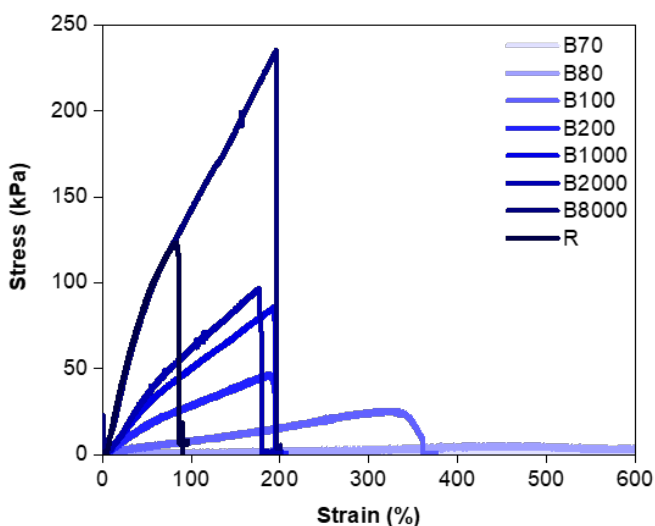


Figure 4-13. Stress-strain curves of homogeneous PSA (black line) and PIMS PSA samples (blue lines).

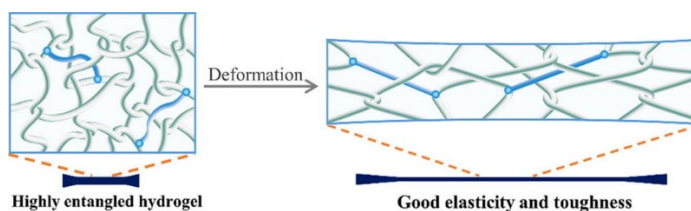


Figure 4-14. Schematic of increasing elasticity and toughness of highly entangled polymer networks (Li, *et al.*, 2022)

3.4. Mechanical Properties according to Heterogeneous Structure

3.4.1. Stress Relaxation Test

Stress relaxation test shows the same trend as the previous properties. The B70 and B80 samples, which lacked material stiffness and connectivity, were unable to recover after being held at 100% strain for 10 min. The B100 and B200 samples showed the best recovery properties, over 90%. Stress relaxation refers to the degree to which an externally applied force is dissipated. When an external force is applied, the polymer responds by conformational change, chain sliding, and the breaking of covalent bonds. The conformational change of the polymer spontaneously restores it back to its original high entropy state once the external force is gone. This characteristic is why elastomers are often called entropy springs, to distinguish them from metal springs. On the other hand, the sliding of chains in a polymer or the breaking of covalent bonds represents a loss of energy. When energy is dissipated within the material, there is no force left to be used for recovery. Samples B100 and B200 show a stress relaxation of about 2%, indicating that most of the strain has been used for conformational change of the polymer chain, hence the excellent recovery properties. The B1000, B2000, and B8000 samples show that as the PBA chain length increases, the stress relaxation becomes larger and more plastic deformation occurs. The R samples, which have crosslinked network as the main structure rather than entanglement, experienced more plastic deformation compared to the B samples and showed a 60% recovery from the initial state.

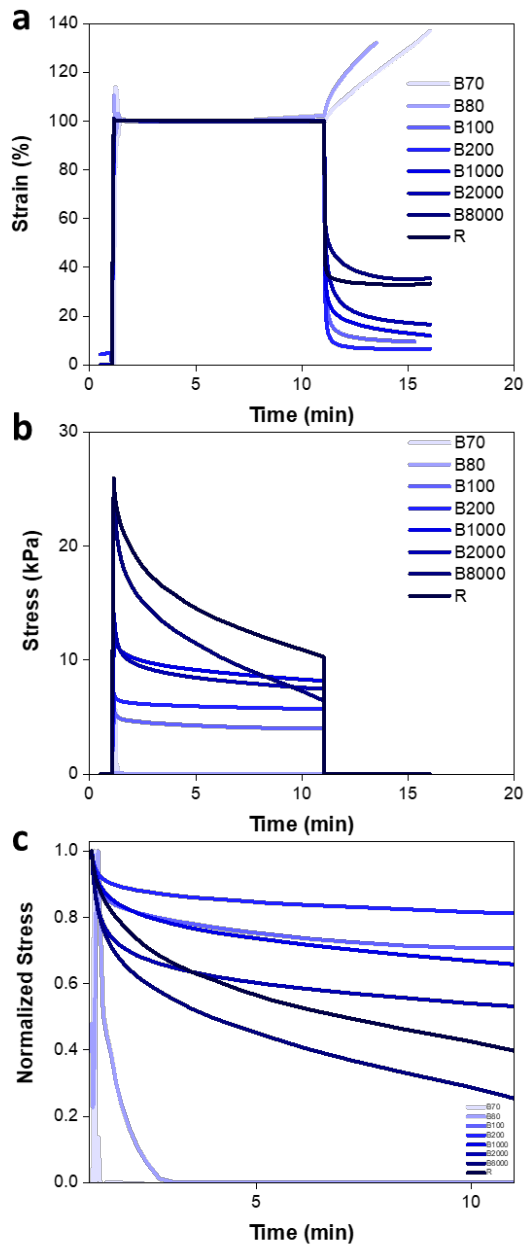


Figure 4-15. Variation of a) strain, b) stress, and c) normalized stress during a stress relaxation test.

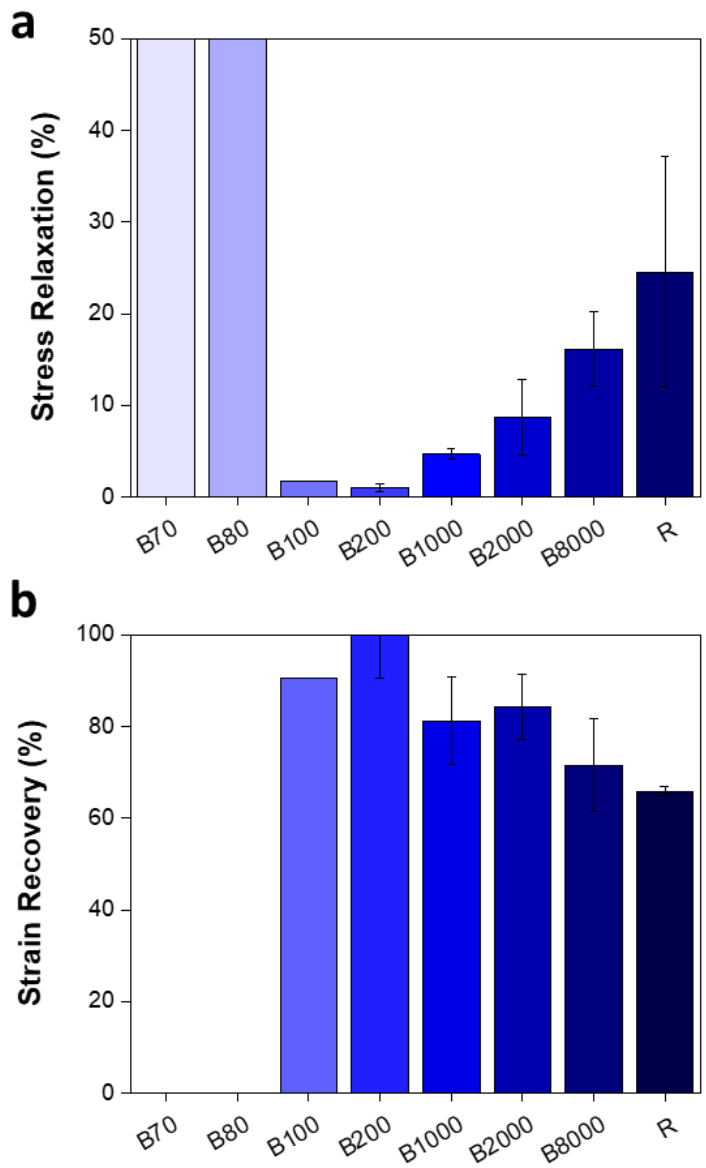


Figure 4-16. a) Stress relaxation of PSA samples after loading 100% strain for 10 min. b) Strain recovery of each PSA sample after 5 min of recovery time.

3.4.2. Adhesion Properties

The adhesion mechanism of PSA consists of an anchoring effect in which the adhesive is wetted on the substrate and anchored to the irregular surface of the substrate, as well as covalent bonds, intermolecular forces, van der Waals, and London dispersion forces caused by molecular contact between the adhesive and the substrate. In other words, 1) mechanical adhesion, which means anchoring effect, 2) chemical adhesion, which means covalent bonds and intermolecular forces, and 3) physical adhesion by close contact of molecules such as wetting. For acrylic based adhesives, the T_g of the base polymer determines the temperature range at which the initial adhesive force, tack, is expressed. Tack cannot be expressed by monomers, so cohesion is achieved through polymerization and crosslinking. Crosslinking of PSA is essential for cohesion, but excessive crosslinking leads to poor wetting. The shorter the PBA chain length, the less intermolecular entanglement, the softer and better wetting, and thus the better tack. However, B70 and B80 contain a large amount of short PBA chain, so the cohesive force is small, resulting in low adhesion and cohesive failure in the peel test. The entanglement and crosslinking of B100 exhibits an adequate level of cohesive force, resulting in excellent peel strength. As the length of PBA chains increases, the intermolecular entanglement increases, which reduces the initial adhesion force, and the peel strength decreases accordingly.

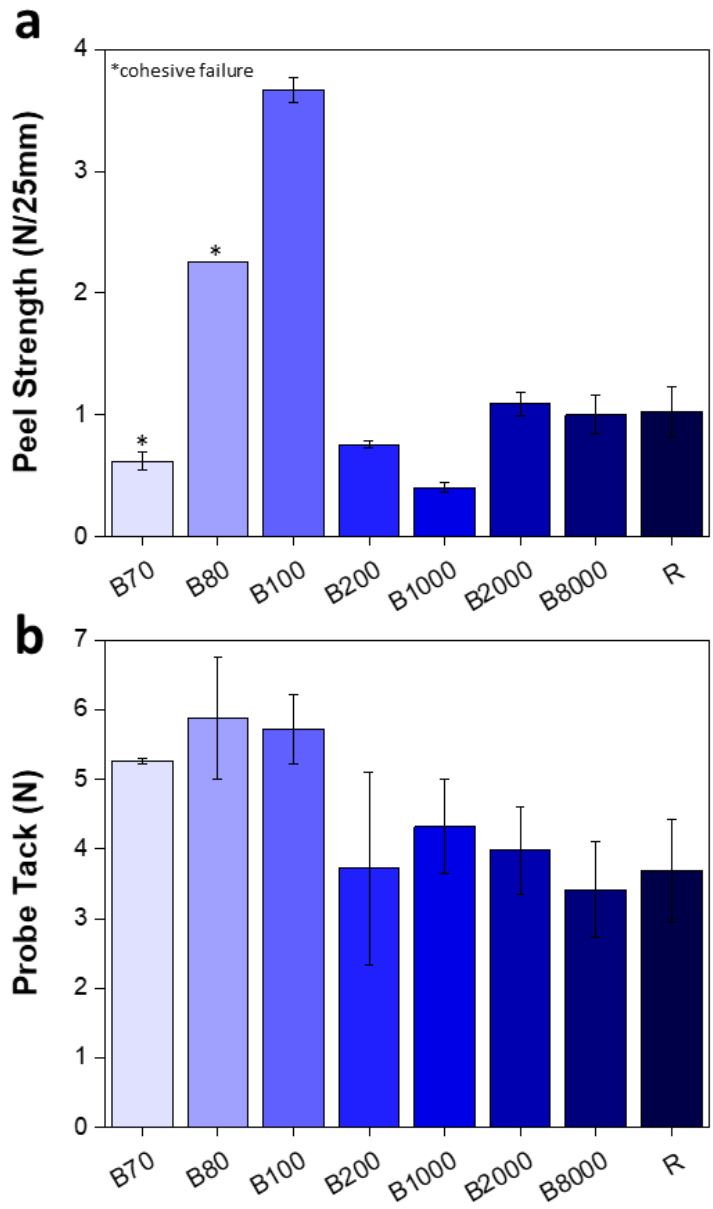


Figure 4-17. a) Peel strength and b) probe tack of PSA samples.

3.5. Polymer Network Structure according to PBA Chain Length Variation

3.5.1. Calculation of Molecular Weight between Crosslinking by Swelling Test

The swelling properties of a polymer are determined by the osmotic pressure of solvents with small molecules and the elasticity of the polymer network. The denser the crosslinked structure of a polymer, the less solvent it will absorb because there is a limit to how far the polymer chains can stretch, and the wider the crosslinked structure, the more solvent it will hold. Swelling experiments were conducted to determine the network structure of the polymer.

The mass swelling ratio of the PSA was calculated for each sample by dividing the PSA swollen weight (m_s) by the dry weight (m_d). The volume fraction of the polymer network, ϕ_p was estimated based on the measured weight. The density of polymer (ρ_p) was 1.087 g/ml of PBA, and the density of solvent (ρ_s) was 0.785 g/ml of Acetone.

$$\phi_p = \left[1 + \frac{\rho_p}{\rho_s} \left(\frac{m_s}{m_d} - 1 \right) \right]^{-1}$$

Since more than 95mol% of the prepared PSA samples consists of BA, the interaction parameter between PBA and acetone (χ_{12}) was obtained and used to calculate the length between crosslinking point. The Hansen solubility parameter (Hansen, 1995, Lindvig, *et al.*, 2002) δ_1 (for acetone) and δ_2 (for PBA) was used to calculate the interaction parameter.

$$\chi_{12} = \frac{v_1}{RT} (\delta_1 - \delta_2)^2$$

Theoretical solubility parameter can be calculated based on the structural formula of resin followed by the equation below (Gao, *et al.*, 2012), where F_i is molar attraction constant and V_i is molar volume of the atomic structure i . The solubility parameters of PBA were calculated from the atomic structure of BA. The values of F_i and V_i for the atomic groups of butyl acrylate are given in Table 4-4 (Gao, *et al.*, 2012). The solubility parameter of PBA(δ_2) was calculated to be 19.35.

$$\delta = \frac{F}{V_m} = \frac{\sum F_i}{\sum V_i}$$

Table 4-4. F_i and V_i of atomic group of poly butyl acrylate

| | F_i | V_i |
|-------|--------|-------|
| -CH3 | 303.4 | 33.5 |
| -CH2- | 1076 | 64.4 |
| -CH< | 176 | -1 |
| >C< | 0 | 0 |
| -COO- | 668.2 | 18 |
| SUM | 2223.6 | 114.9 |

The total solubility parameter (δ_t) can be calculated by the sum of the squared hansen solubility parameter for dispersion (δ_d), dipolar (δ_p), and hydrogen bonds (δ_h) as shown in the equation below (Hansen, 1995). The solubility parameter for acetone was calculated using the well-known values of δ_d 15.5, δ_p 10.4, and δ_h 7 (Koleske, 2012). The solubility parameter of acetone (δ_1) is 19.93. Using this, we obtained a value of 0.01 for the interaction parameter of PBA and acetone (χ_{12}).

$$\delta_t^2 = \delta_d^2 + \delta_p^2 + \delta_h^2$$

In order to understand the components of the polymer network in detail by dividing them into backbone, brush, crosslinker, and chain end, a new Flory-Rehner (F-R) approach (Borges, *et al.*, 2020) was used. In the modified F-R approach used here, molecular weight between crosslink calculated by classical F-R equation (Flory, *et al.*, Flory, *et al.*, 1943, Flory, 1950) is considered to be composed of the length of the crosslinker (XC) and the length of the backbone (BB), and define a new hypothetical segment λ connecting the end of the BB segment and the middle of the crosslinker segment as expressed in figure 4-19.

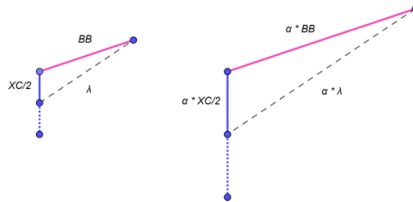


Figure 4-18. Hypothetical segment λ connecting the end of the backbone (BB) segment and the middle of the crosslinker (XC) segment (Borges, *et al.*, 2020)

Utilizing the experimental value of the swelling ratio and the modified F-R equation below, we found the length of the surrogate segment λ , M_i , where \bar{v} is the specific volume of the polymer (0.92 ml/g for PBA), V_1 is the molar volume of the solvent (74.16 ml/mol for acetone).

$$\frac{1}{M_\lambda} = - \frac{(\bar{v}/V_1)[\ln(1 - \phi_p) + \phi_p + \chi_{12}\phi_p^2]}{\phi_p^{1/3} - \phi_p/2}$$

The total molecular weight in-between crosslinks was obtained by subtracting the length corresponding to the crosslinker from the surrogate segment λ , using the equation below. Where M_{tc} is the total molecular weight between crosslinks and M_{XC} is the molecular weight of the crosslinking monomer, which is 250 for PEGDA in this paper.

$$M_{tc} = M_\lambda - M_{XC}/2$$

The PIMS PSA fabricated in this paper consists of a backbone (BB) segment of the crosslinking network, a brush (BR) segment resting on the backbone, a crosslinker (XC), and a linear PBA segment at the freely moving chain end (CE). We calculated M_{BB} , M_{BR} , and M_{CE} by separating them from each other. In general, the branch between the crosslinking points is considered to be the number of crosslinked monomers with only one side connected and the other side free, and the length of the brush attached to the backbone between the crosslinking points is considered to be equal to the length of the crosslinker.

Therefore, M_{BR} is 250, which is the M_n of the crosslinker, PEGDA. The M_{CE} was considered to be equal to the PBA chain length of PBA-CTA. M_{BB} is calculated by using the equation below, where M_r is the average molecular weight of a repeat unit. Mole fraction of the crosslinker, f_x , are essential for the application of the modified F-R equations. Here, the composition of the PSA film was assumed to be equal to the that of the raw material mixtures, since the conversion of the PSA film is close to 100%. The results of the calculation are summarized in the Table 4-5.

$$M_{BB} = M_{tc} - \frac{M_{BR}f_x M_{tc}}{M_r}$$

Table 4-5. Calculated M_{BB} and M_{CE} of the prepared PSA samples.

| | M_{BB} | M_{CE} |
|-------|----------|-----------|
| B70 | 347,769 | 9,592 |
| B80 | 194,114 | 11,888 |
| B100 | 100,174 | 12,950 |
| B200 | 2,635 | 27,751 |
| B1000 | 11,816 | 132,588 |
| B2000 | 28,530 | 237,035 |
| B8000 | 22,477 | 1,053,397 |
| R | 59,602 | - |

In entanglement-rich PIMS PSA, calculated M_{tc} based on the F-H theory explains both chemical crosslinking and physical entanglement points. B70 and B80 have long distances between chemical crosslinking and physical entanglement points, as shown in Figure 4-20 a). B70 and B80 have a gel fraction of 10% or less and are composed mostly of linear polymer chains, i.e. their polymer network is composed of a network of very low crosslinking density and many short linear chains. Because of the large number of linear chains and their short length, there is very little entanglement point.

B100 exhibits a gel fraction of 44%. B100 has a mixture of 56% moderately wide crosslinked network and 44% linear chains. The large distance between chemical crosslinking and physical entanglement appears to be a factor in exhibiting a linear elastic region in the wide elongation region.

B200, B1000, and B2000 have a gel fraction close to 80% due to the increase in physical entanglement as the PBA length increases. They are composed of 80% of crosslinked and entangled polymer network with very high crosslinking density and 20% of linear chains. The short inter-crosslink distances and high crosslink density are responsible for the reduced elongation at break. They found that as the PBA length increased, the distance between crosslinks tended to increase proportionally. In Figure 4-21 a), the M_{CE}/M_{BB} remained constantly at a ratio of 10 even though the PBA chain lengths differed by 5 and 10 times.

Although B8000 has a very long PBA chain length, M_{ic} was not significantly different from B2000. If the amount of entanglement was the same, M_{ic} would have increased. It is speculated that the number of entanglements has increased without a significant change in M_{ic} . The increased entanglement is what improved the toughness of the material.

Through the comparison of the B series, the relationship between PBA chain length and the morphology of the polymer network was determined. When the length of the PBA chain is below the DP 200, as the chain length increases, the distance between crosslinks and entanglement decreases. In this group (B70, B80, B100), the number of entanglement increases as the PBA length increases and the gel fraction increases.

For PBA lengths from DP 200 to 2000, M_{ic} increases proportionally as the PBA chain length increases. As a result, the ratio of M_{BB} to M_{CE} , i.e., the distance between crosslinks and entanglements and the length of the PBA chain, remains constant at 1:10 in this interval.

The entanglement distance does not change much beyond a certain level of PBA length. From the point where DP of the PBA is greater than 2000, it can be seen that the longer length of the PBA affects the number of entanglements more than the distance between entanglements. The number of entanglement

increases with increasing PBA chain length, which explains the increased toughness.

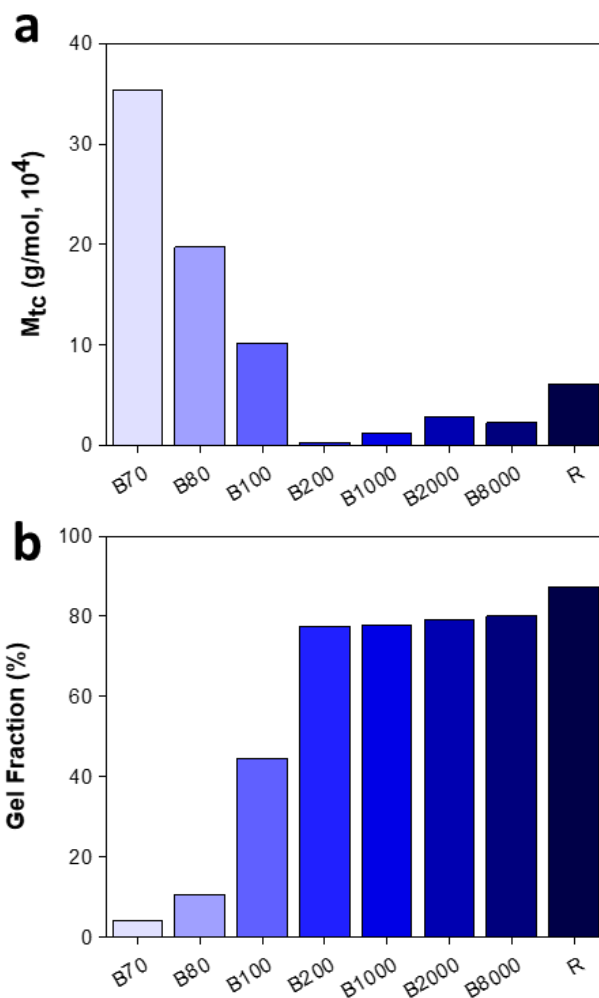


Figure 4-19. a) Total molecular weight between crosslinks and entanglement and b) gel fraction of the PSA samples.

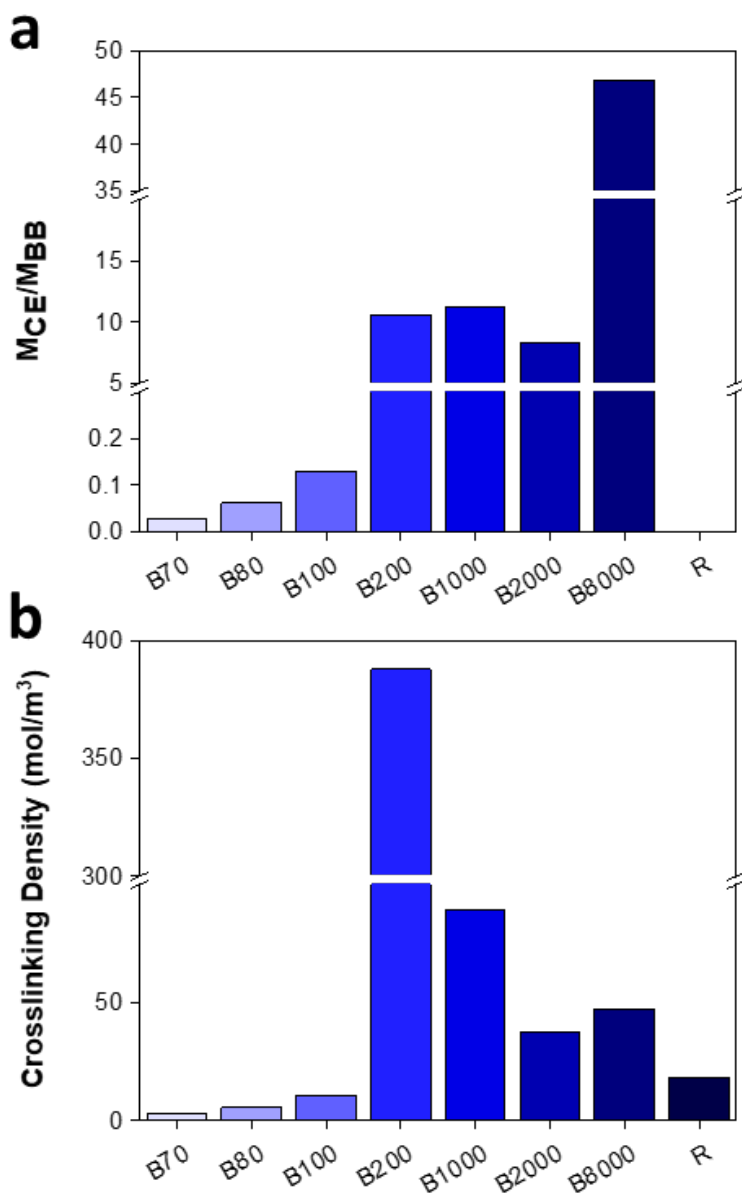


Figure 4-20. a) Ratio of the length of the chain end to the length of the backbone between the crosslink and entanglement points and b) crosslinking density of the PSA samples.

3.5.2. Schematic Molecular Structure

By changing the length of the PBA chain, we have gained a sequential understanding of the changes in the structure of the polymer network. As the PBA length increases, the number of propagating chains in the chain extension process decreases, resulting in a longer linear chain. In the case of B70, since the PBA chain length is short and the number of propagating chains is large, chain extension results in many short linear chains. These short linear chains are difficult to form entanglement and are easily dissolved upon contact with solvent, indicating a degradation of the gel fraction. B70 are subject to plastic deformation as the chains slide over each other when stretched. B100 has a structure with a good combination of moderate crosslinking and entanglement. Therefore, B100 is easily elongated when stretched. The elongation of B100 is a process in which the chains stretch and change conformation. Since the crosslinking and entanglement points of the polymer network are maintained, it behaves as an entropy spring and returns perfectly to its original state when the external force disappears. B1000 has a long length and a small number of PBA-CTAs, so chain extension results in long and small number of chains. As a result, it forms a densely entangled network. Since B1000 has many crosslinking points when stretched, the entanglement begins to unravel when the chain is stretched beyond its limit. Further strain causes the covalent bonds to break. This elongation behavior is the mechanism of plastic deformation. R has a very densely crosslinked structure. When stretched, the chain has a short range to stretch, and there is not much entanglement to unravel, so covalent bond cleavage occurs even at low strains. To better understand this mechanism, a schematic representation of the polymer network is shown in Figure 4-22. The length of the newly formed P(BA-stat-AA) in the process of chain extension considering PBA chain length, monomer molar fraction and number of PBA-CTAs, and the frequency of crosslinking and entanglement along the chain

length are shown in the Figure 4-22.

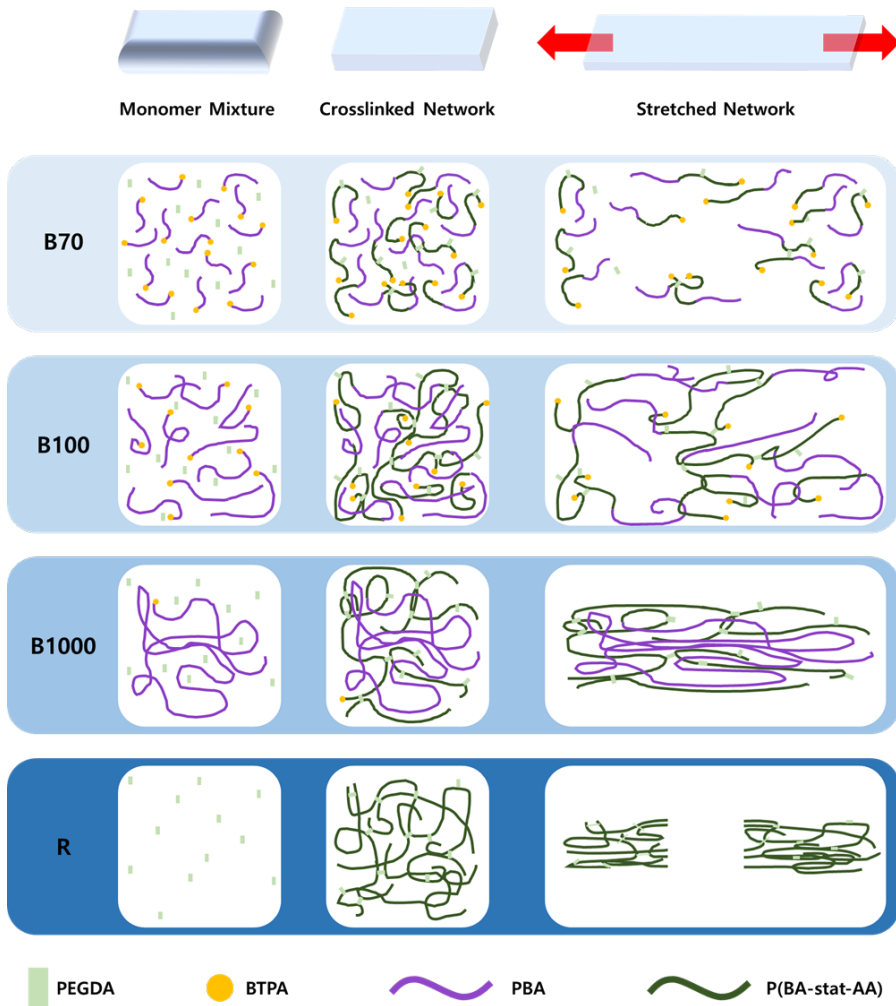


Figure 4-21. Schematic diagram of the PSA polymer network.

3.6. Application Test

3.6.1. Folding Test

In both room temperature and high temperature/humidity folding tests, all samples except B100 showed delamination and crack before the final cycle. The B100 sample did not show any defects after 200k of repeated folding. In the low temperature folding test, all samples except B100 and R showed delamination and crack. The cycle number at which each sample failed is summarized in the Figure 4-23. The appearance of the samples after each test is shown in the Figures 4-24, 4-25, 4-26.

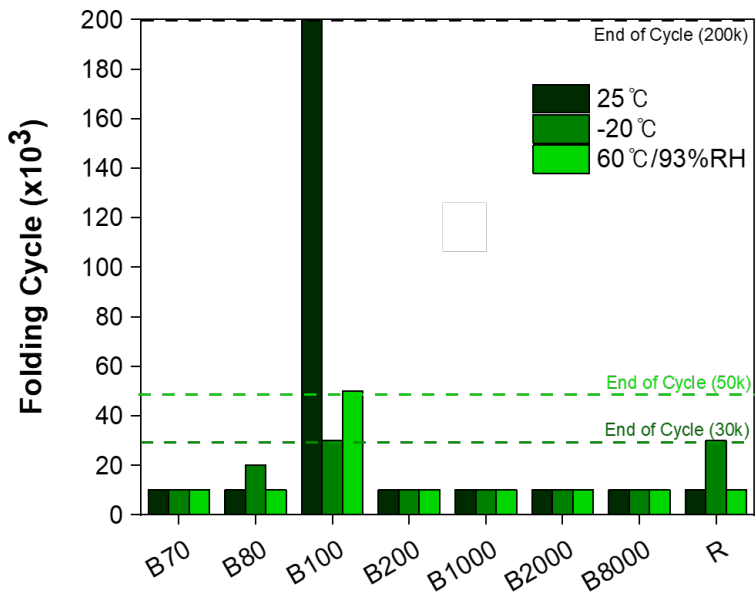


Figure 4-22. The folding cycle number at which each sample failed in the room temperature, low temperature, and high temperature/humidity folding tests.

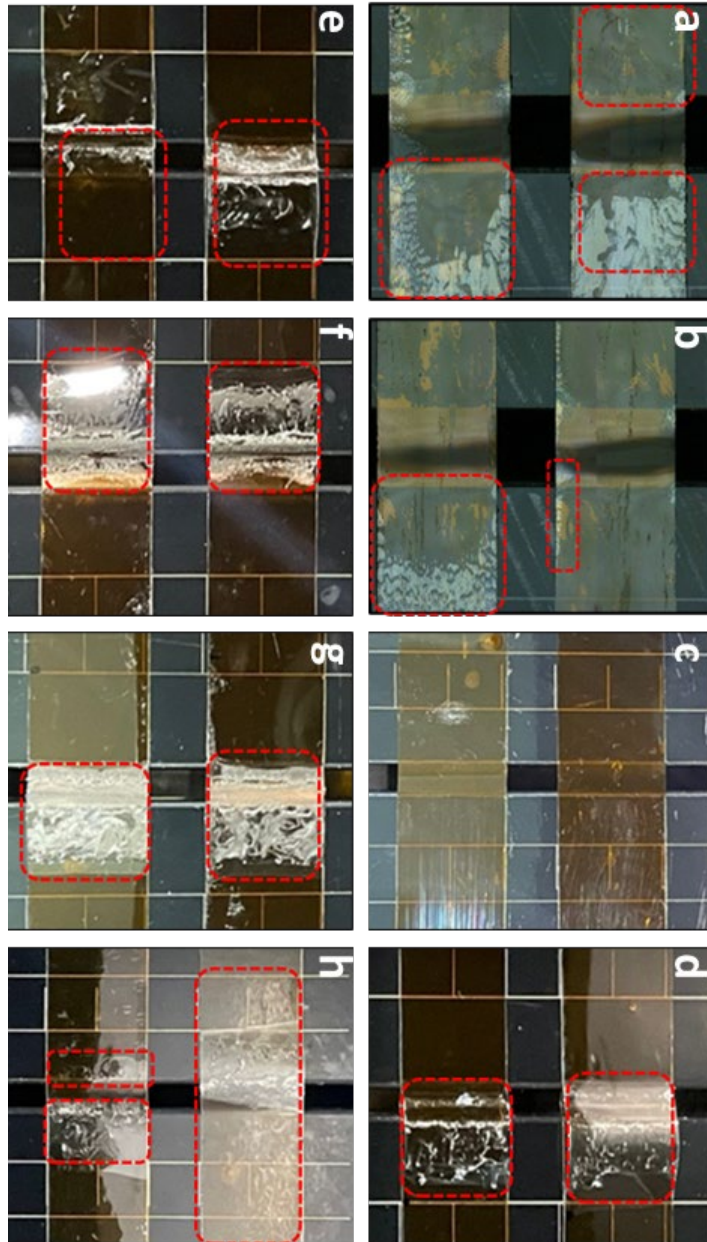


Figure 4-23. PSA samples after 200k folding test at 25 °C. a) B70, b) B80, c) B100, d) B200, e) B1000, f) B2000, g) B8000, h) R.

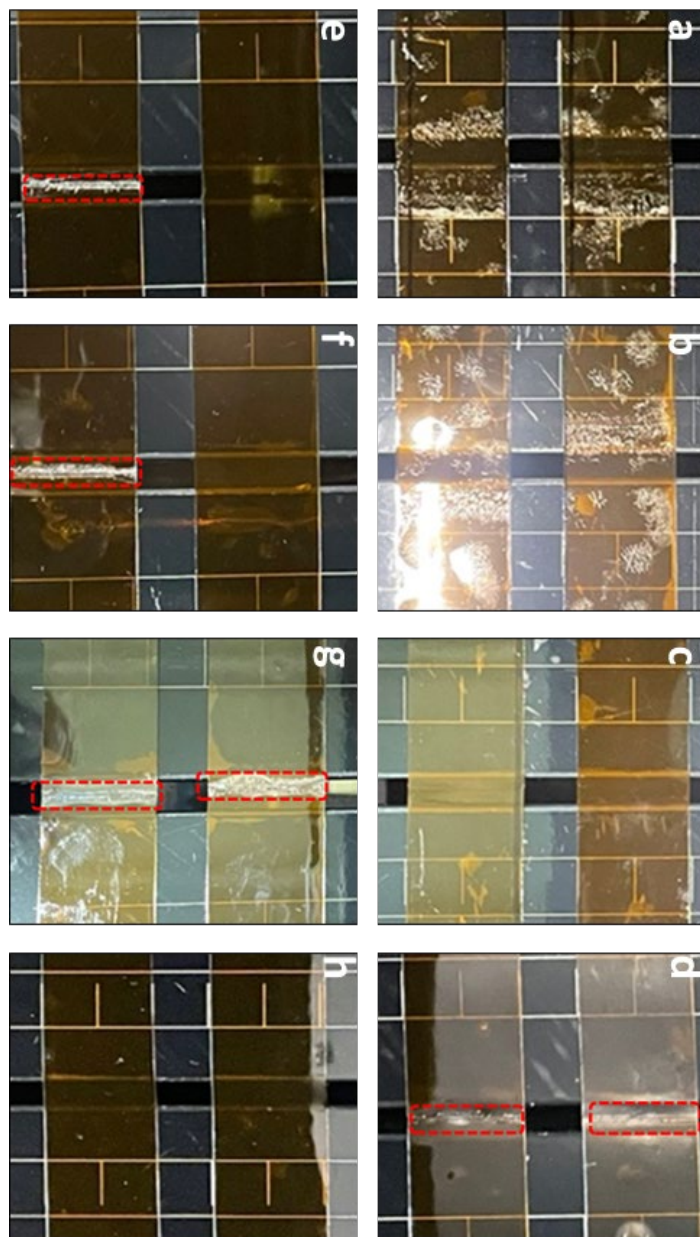


Figure 4-24. PSA samples after 30k folding test at -20 °C. a) B70, b) B80, c) B100, d) B200, e) B1000, f) B2000, g) B8000, h) R.

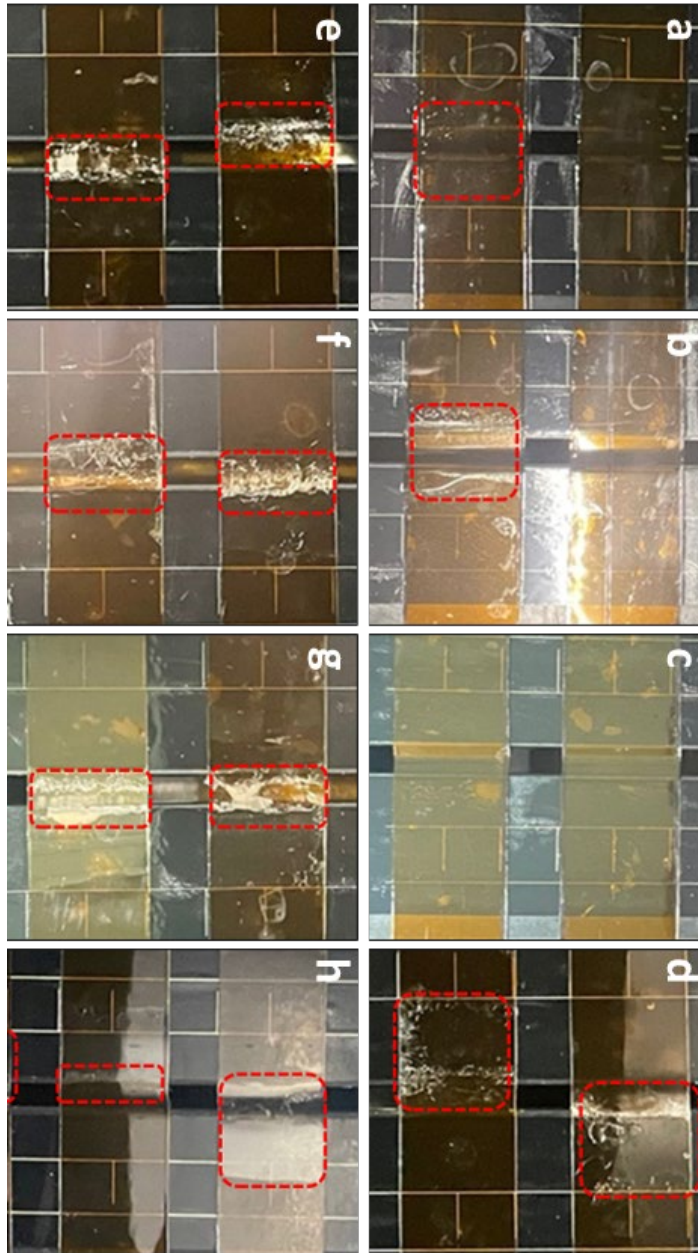


Figure 4-25. PSA samples after 50k folding test at 60 °C/93 %RH. a) B70, b) B80, c) B100, d) B200, e) B1000, f) B2000, g) B8000, h) R.

When the folding test results are considered together with the adhesion and recovery properties, B100 exhibits exceptional peel strength and strain recovery at room temperature, indicating excellent performance in the folding test at room temperature. Despite all samples fracturing due to high shear deformation in the high-temperature (60 °C) DMA strain recovery test, remarkable high-temperature adhesive properties (Figure 4-27 a) of B100 seem to have influenced its outstanding folding performance at high temperature. The degree of crosslinking of the material directly influenced the recovery performance in the low temperature (-20 °C) strain recovery test. B100 and R exhibited superior folding performance, while B2000 struggled in rapidly recurring deformation folding tests.

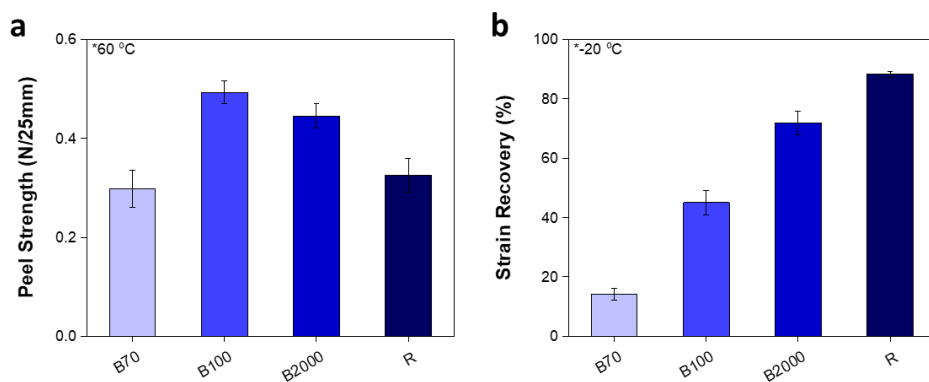


Figure 4-26. a) Peel strength at high temperature (60 °C) of representative PSA samples. b) Strain recovery properties at low temperature (-20 °C) of representative PSA samples.

3.6.2. Transmittance and Haze

The PSA samples including B series showed excellent transparency. They exhibited transparency that was almost as same as a single PET film. Haze was also barely degraded when compared to a single film of PET. Their optical performance is suitable for use as OCAs for displays. The optical property results indicate that the inhomogeneities in the PIMS PSAs contain domains smaller than the wavelength of visible light and are therefore undetectable by the naked eye. The PIMS method used in this paper is a breakthrough method that represents a significant improvement in physical properties while having little impact on transparency and haze degradation.

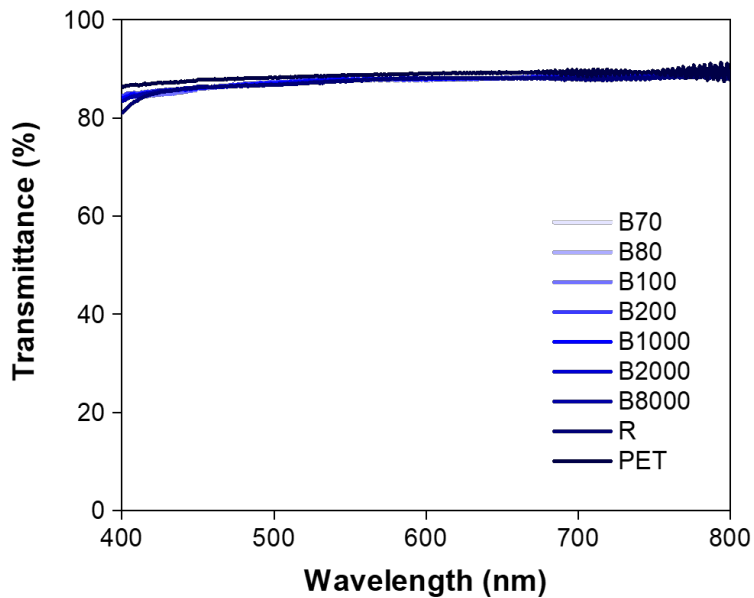


Figure 4-27. Transmittance property of the PSA samples and PET film.

Table 4-6. Haze of the PSA samples and PET films. Since the PSA was measured between two PET films, control refers to two of PET films.

| | Total Luminous Transmittance | Diffuse Luminous Transmittance | Haze (%) |
|---------|------------------------------|--------------------------------|----------|
| B70 | 0.8769 | 0.0187 | 2.1273 |
| B80 | 0.877 | 0.0187 | 2.1268 |
| B100 | 0.877 | 0.208 | 2.3715 |
| B200 | 0.8782 | 0.207 | 2.3626 |
| B1000 | 0.8777 | 0.0187 | 2.1273 |
| B2000 | 0.8774 | 0.0193 | 2.1986 |
| B8000 | 0.8774 | 0.0193 | 2.1992 |
| R | 0.8768 | 0.0177 | 2.0155 |
| PET | 0.8878 | 0.0142 | 1.6042 |
| Control | 0.7968 | 0.0304 | 3.8157 |

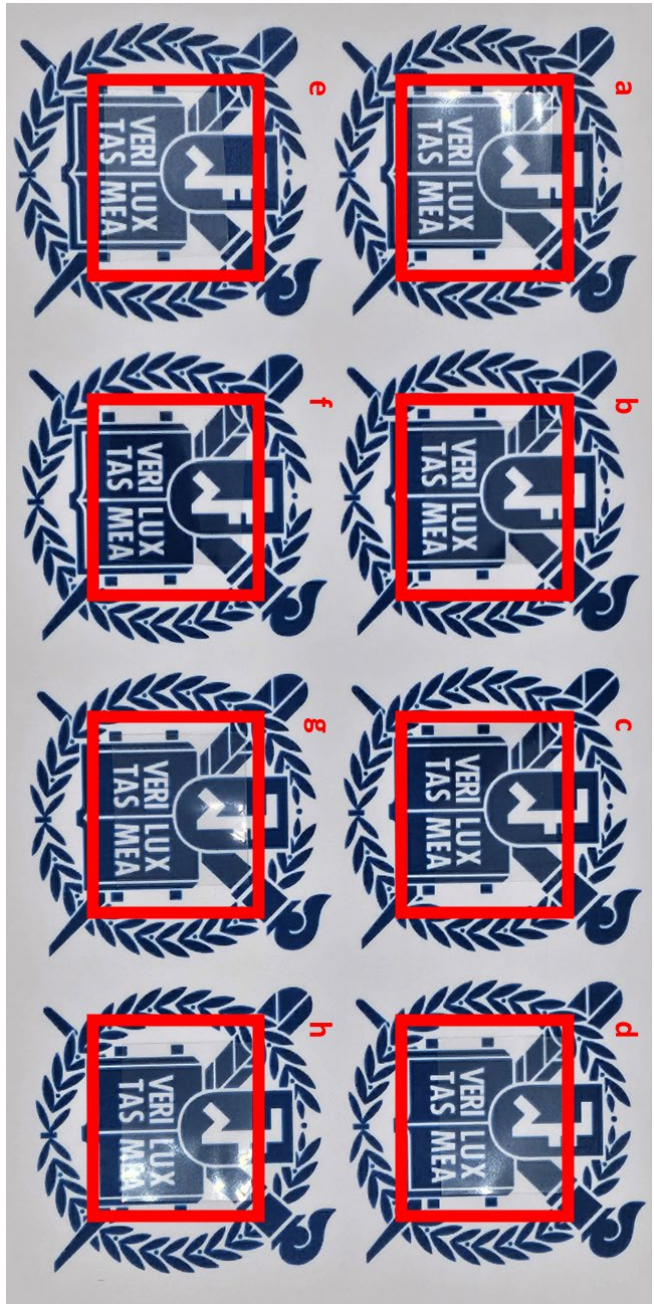


Figure 4-28. A photograph showing the transparency of the PSA samples. a) B70, b) B80, c) B100, d) B200, e) B1000, f) B2000, g) B8000, h) R.

4. Conclusions

We have shown excellent elongation, elasticity, and adhesive properties of heterogeneous PSA prepared using PIMS in Chapter 3. The purpose of Chapter 4 is to identify the structural causes of the polymer network that result in such excellent properties. To impart variables in the polymer network, the chain length of PBA-CTA was adjusted from DP 70 to 8000. PSA films having different lengths of PBA chains at the chain ends of the network were prepared. The effect of varying the length of the PBA chains on the polymer network morphology was confirmed by TEM image analysis. As the PBA length increases, the size and length of the soft domains increase, and the spacing become wider. The changes in the polymer network identified visually were also characterized rheologically and physically. When the PBA length was DP 100, it exhibited the best linear elastic behavior like a rubber. When the PBA was smaller than DP 100, the polymer network became fragmented and showed plastic deformation upon stretching. When the PBA is larger than DP 200, the elongation at break decreases as the entanglement increases. As the PBA length increases, the number of entanglement increases, showing an increase in toughness. The results of calculating the crosslinking and entanglement length by swelling test are well understood in relation to the physical properties. Finally, we tested the application of PIMS PSA as an OCA for flexible displays. Among the PIMS PSAs we fabricated, B100 with the appropriate degree of crosslinking can withstand 200k folding cycles and exhibit excellent transparency. The heterogeneous PSA utilizing PIMS will be a breakthrough method for developing OCAs for flexible displays with excellent properties. This is essential to consider as materials containing sulfur are susceptible to yellowing and odor. The PIMS structure used in this study contains sulfur atoms as covalent bonds in the cross-linked polymer, resulting in a cured OCA with

little odor when applied. In addition, the target application, a foldable display, has a structure that requires a protective film and is shipped from the factory with a protective film attached. This protective film blocks UV exposure in the application environment, eliminating discoloration and odor issues compared to other display types.

Chapter 5

Overall Conclusions

1. Overall Conclusions

The objective of this study was to develop a PSA with both excellent elasticity and adhesive properties, which is difficult to achieve with conventional homogeneous PSAs. In this study, we first prepared macro-scale inhomogeneous PSA using UV patterning, which confirmed the possibility of improving the properties of inhomogeneous PSA. However, this method had limitations in reducing the size of inhomogeneous domains. In our next study, we utilized PIMS to prepare heterogeneous PSA with domain sizes of nano meter scale. The PIMS PSAs showed excellent physical properties compared to homogeneous PSAs or PSA blended with linear chain. We wanted to understand what structure of the polymer network is responsible for this physical superiority of PIMS PSA. Understanding the relationship between the polymer network and flexibility can be a great contribution to future research of materials design. We designed polymer networks with different chain length of PBA at the chain ends of the network and understood the effect of increasing the length of PBA on the length of entanglement and crosslinked structures, the ratio of crosslinked backbone to chain end length, and the weight ratio of crosslinked polymers to linear polymer chains. From this study, we identified the degree of crosslinking and the length of end chains that resulted in the best physical properties of the heterogeneous PSAs.

1.1. Identify the Potential for Improving Properties of Heterogeneous PSA

To confirm the validity of introducing UV patterning technology, we kinetically verified the possibility of splitting the acrylic UV bulk curing process into two steps. After confirming UV-cured pattern formation in PSAs, strain recovery and stress relaxation performance were measured to confirm its applicability in flexible displays. Compared to the non-patterned sample, the patterned sample showed a significant improvement in recovery performance when the difference in UV curing energy between patterns was 2~3 J. At the same time, the adhesion performance of PSA was maintained except for the sample with the largest energy difference (4 J). In addition, all samples showed good transparency and applicability to Optical Clear Adhesive (OCA). In conclusion, the study showed that implementing the cure density patterning technique during the UV irradiation process can maintain the adhesive properties and transparency while improving the recovery properties of PSA without changing the polymer resin pre-composition or additive content. However, although the adhesive performance of the heterogeneous samples was not inferior to the homogeneous samples, the expected dramatic improvement was not achieved. This can be improved by reducing the domain size or designing other forms of heterogeneous structures.

1.2. Fabrication of Novel Nano Structured Heterogeneous PSA

Utilizing PIMS, we have successfully manufactured micro phase separated heterogeneous PSAs. PIMS PSAs exhibited remarkable properties including very low modulus, elongated elastic region, excellent recovery properties, and superior adhesive properties, despite having the same composition as homogeneous materials. The fact that these distinct properties emerged solely from changes in chemical structure, while maintaining the same composition, holds significant significance in the field of PSA material research.

This dramatic improvement in properties is not due to the presence of linear PBA in the matrix. L30 and L40 samples with blended inert PBA chains did not show a significant improvement in properties. This study is the first to fabricate heterogeneous PSA by using PIMS and provides clues to solve the long-standing challenge of PSA properties for application of flexible displays.

1.3. Study of Polymer Network exhibiting Linear Elasticity

We sought to identify the structural causes for the excellent elasticity of the PIMS polymer network. Various PSA films with different lengths of PBA chains at the chain ends of the network were prepared. The effect of different PBA chain lengths on the polymer network morphology was confirmed by TEM image analysis. The length of the PBA chains is directly related to the size and length of the soft domains, and the spacing between them increases. Physical and rheological evaluations were utilized to further explore the changes in the network. At DP 100, the PBA chains exhibited optimal linear elastic properties similar to rubber. When PBA was below DP 100, the polymer network became fragmented and exhibited plastic deformation under stretch. In contrast, when the PBA exceeded DP 200, the elongation at break decreased with increasing entanglement. The properties were correlated with the results of the swelling test to estimate the crosslinking and entanglement length. Finally, the application of PIMS PSA as an OCA for flexible displays was tested. Among the fabricated PIMS PSAs, B100 with appropriate crosslinking degree was able to withstand 200k folding cycles and exhibited good transparency. The utilization of heterogeneous PSAs using PIMS provides a breakthrough for the development of OCAs for flexible displays.

References

Allen, N. S., 1996, Photoinitiators for UV and Visible Curing of Coatings: Mechanisms and Properties, *Journal of Photochemistry and Photobiology A: chemistry*, **100** (1-3): 101-107

An, S., Lee, J., Kim, Y., Kim, T., Jin, D., Min, H., Chung, H. and Kim, S. S., 2010, 47.2: 2.8-inch WQVGA Flexible AMOLED Using High Performance Low Temperature Polysilicon TFT on Plastic Substrates, *SID Symposium Digest of Technical Papers*, **41** (1): 706-709, Wiley Online Library

Antman, S. S., 2005, Problems in Nonlinear Elasticity, *Nonlinear Problems of Elasticity*: 513-584

Avellar, L., Reese, T., Bhattacharya, K. and Ravichandran, G., 2018, Effect of Cohesive Zone Size on Peeling of Heterogeneous Adhesive Tape, *Journal of Applied Mechanics*, **85** (12).

Back, J.-H., Baek, D., Sim, K.-B., Oh, G.-Y., Jang, S.-W., Kim, H.-J. and Kim, Y., 2019, Optimization of Recovery and Relaxation of Acrylic Pressure-Sensitive Adhesives by using UV Patterning for Flexible Displays, *Industrial Engineering Chemistry Research*, **58**: 4331-4340

Back, J.-H., Baek, D., Sim, K.-B., Oh, G.-Y., Jang, S.-W., Kim, H.-J. and Kim, Y., 2019, Optimization of Recovery and Relaxation of Acrylic Pressure-Sensitive Adhesives by using UV Patterning for Flexible Displays, *Industrial & Engineering Chemistry Research*, **58** (10): 4331-4340

Back, J.-H., Baek, D., Park, J.-W., Kim, H.-J., Jang, J.-Y. and Lee, S.-J., 2020, Shock Absorption of Semi-Interpenetrating Network Acrylic Pressure-

Sensitive Adhesive for Mobile Display Impact Resistance, *International Journal of Adhesion and Adhesives*, **99**.

Back, J. H., Kwon, Y., Cho, H., Lee, H., Ahn, D., Kim, H. J., Yu, Y., Kim, Y., Lee, W. and Kwon, M. S., 2022, Visible-Light-Curable Acrylic Resins toward UV-Light-Blocking Adhesives for Foldable Displays, *Advanced Materials*: 2204776

Baek, S.-S. and Hwang, S.-H., 2017, Preparation of Biomass-based Transparent Pressure Sensitive Adhesives for Optically Clear Adhesive and Their Adhesion Performance, *European Polymer Journal*, **92**: 97-104

Barisa, R. E., Resalati, H., Hadi, M., Ghasemiyani, A. and Shakeri, A., 2014, The Structure and Physical -Chemical Properties of Polymers in Pressure-sensitive Adhesives (PSA), *Basparesh*, **4** (4), 77-85.

Barth, J. V., Costantini, G. and Kern, K., 2005, Engineering Atomic and Molecular Nanostructures at Surfaces, *Nature*, **437** (7059): 671-679

Bates, F. S., 1991, Polymer-polymer Phase Behavior, *Science*, **251** (4996): 898-905

Bates, F. S. and Fredrickson, G. H., 1999, Block Copolymers—Designer Soft Materials, *Physics Today*, **52** (2): 32-38

Benedek, I. and Feldstein, M. M., Handbook of Pressure-Sensitive Adhesives and Products:-Three Volume Set, 2008, CRC Press

Benedek, I., Pressure-Sensitive Formulation, 2020, CRC Press

Bennett, A. W. and Watts, D. C., 2004, Performance of Two Blue Light-Emitting-Diode Dental Light Curing Units with Distance and Irradiation-Time, *Dental Materials*, **20** (1): 72-79

Blagodatski, A., Sergeev, A., Kryuchkov, M., Lopatina, Y. and Katanaev, V. L., 2015, Diverse Set of Turing Nanopatterns Coat Corneae Across Insect Lineages, *Proceedings of the National Academy of Sciences*, **112** (34): 10750-10755

Blanazs, A., Armes, S. P. and Ryan, A. J., 2009, Self-assembled Block Copolymer Aggregates: from Micelles to Vesicles and Their Biological Applications, *Macromolecular Rapid Communications*, **30** (4-5): 267-277

Bobrin, V. A., Lee, K., Zhang, J., Corrigan, N. and Boyer, C., 2022, Nanostructure Control in 3D Printed Materials, *Advanced Materials*, **34** (4): 2107643

Bobrin, V. A., Yao, Y., Shi, X., Xiu, Y., Zhang, J., Corrigan, N. and Boyer, C., 2022, Nano-to Macro-scale Control of 3D Printed Materials via Polymerization Induced Microphase Separation, *Nature Communications*, **13** (1): 3577

Bonamy, D., Santucci, S. and Ponsen, L., 2008, Crackling Dynamics in Material Failure as the Signature of a Self-organized Dynamic Phase Transition, *Physical Review Letters*, **101** (4): 045501

Borges, F. T., Papavasiliou, G. and Teymour, F., 2020, Characterizing the Molecular Architecture of Hydrogels and Crosslinked Polymer Networks beyond Flory–Rehner—I. Theory, *Biomacromolecules*, **21** (12): 5104-5118

Bowman, C. and Newell, A., 1998, Natural Patterns and Wavelets, *Reviews of Modern Physics*, **70** (1): 289

Budiansky, B., 1965, On the Elastic Moduli of Some Heterogeneous Materials, *Journal of the Mechanics and Physics of Solids*, **13** (4): 223-227

Cabral, H., Miyata, K., Osada, K. and Kataoka, K., 2018, Block Copolymer Micelles in Nanomedicine Applications, *Chemical Reviews*, **118** (14): 6844-6892

Campbell, C. J., Clapper, J., Behling, R. E., Erdogan, B., Beagi, H. Z., Abrahamson, J. T. and Everaerts, A. I., 2017, P-198: Optically Clear Adhesives Enabling Foldable and Flexible OLED Displays, *SID Symposium Digest of Technical Papers*, **48** (1): 2009-2011, Wiley Online Library

Cao, J., Tan, Y., Chen, Y., Zhang, L. and Tan, J., 2021, Expanding the Scope of Polymerization-Induced Self-Assembly: Recent Advances and New Horizons, *Macromolecular Rapid Communications*, **42** (23): 2100498

Chattopadhyay, D., Panda, S. S. and Raju, K., 2005, Thermal and Mechanical Properties of Epoxy Acrylate/methacrylates UV Cured Coatings, *Progress in Organic Coatings*, **54** (1): 10-19

Chen, C.-J. and Lin, K.-L., 2000, Internal Stress and Adhesion of Amorphous Ni-Cu-P Alloy on Aluminum, *Thin Solid Films*, **370** (1-2): 106-113

Chen, Q., Bae, S. C. and Granick, S., 2011, Directed Self-assembly of a Colloidal Kagome Lattice, *Nature*, **469** (7330): 381-384

Cheng, G., Li, X., Nie, Y. and Li, H., 2019, FEM-Cluster based Reduction Method for Efficient Numerical Prediction of Effective Properties of Heterogeneous Material in Nonlinear Range, *Computer Methods in Applied Mechanics and Engineering*, **348**: 157-184

Chopade, S. A., So, S., Hillmyer, M. A. and Lodge, T. P., 2016, Anhydrous Proton Conducting Polymer Electrolyte Membranes via Polymerization-Induced Microphase Separation, *ACS Applied Materials & Interfaces*, **8** (9): 6200-6210

Chopade, S. A., Au, J. G., Li, Z., Schmidt, P. W., Hillmyer, M. A. and Lodge, T. P., 2017, Robust Polymer Electrolyte Membranes with High Ambient-Temperature Lithium-ion Conductivity via Polymerization-Induced Microphase Separation, *ACS Applied Materials & Interfaces*, **9** (17): 14561-14565

Christensen, R. M., 1968, Variational and Minimum Theorems for the Linear Theory of Viscoelasticity, *Zeitschrift Für Angewandte Mathematik und Physik ZAMP*, **19** (2): 233-243

Christensen, R. M., 1969, Viscoelastic Properties of Heterogeneous Media, *Journal of the Mechanics and Physics of Solids*, **17** (1): 23-41

Class, J. and Chu, S., The Viscoelastic Properties of Pressure-Sensitive Adhesives, 1984, in *Adhesive Chemistry*, Springer

Colley, A., Pfleging, B., Alt, F. and Häkkinä, J., 2020, Exploring Public Wearable Display of Wellness Tracker Data, *International Journal of Human-*

Computer Studies, **138**: 102408

Creton, C., 2003, Pressure-Sensitive Adhesives: an Introductory Course, *MRS Bulletin*, **28** (6): 434-439

Creton, C., Roos, A. and Chiche, A., 2005, Effect of the Diblock Content on the Adhesive and Deformation Properties of PSAs based on Styrenic Block Copolymers, *Adhesion: Current Research and Applications*: 337-363

Creton, C. and Ciccotti, M., 2016, Fracture and Adhesion of Soft Materials: a review, *Reports on Progress in Physics*, **79** (4): 046601

Czech, Z., 2007, Synthesis and Cross-linking of Acrylic PSA Systems, *Journal of Adhesion Science and Technology*, **21** (7): 625-635

Czech, Z. and Pelech, R., 2009, The Thermal Degradation of Acrylic Pressure-Sensitive Adhesives based on Butyl Acrylate and Acrylic Acid, *Progress in Organic Coatings*, **65** (1): 84-87

Czech, Z., Kowalczyk, A., Gąsiorowska, M., Soroka, J. and Kabatc, J., 2011, Novel Pyridinium Derivatives as Very Efficient Photoinitiators for UV-Activated Synthesis of Acrylic Pressure-Sensitive Adhesives, *International Journal of Adhesion and Adhesives*, **31** (7): 634-638

Czech, Z., Kowalczyk, A., Kabatc, J. and Świdorska, J., 2012, UV-crosslinkable Acrylic Pressure-Sensitive Adhesives for Industrial Application, *Polymer Bulletin*, **69** (1): 71-80

De Gennes, P.-G., *Scaling Concepts in Polymer Physics*, 1979, Cornell

University Press

Decker, C. and Moussa, K., 1990, Real-time Monitoring of Ultrafast Curing by UV-radiation and Laser Beams, *JCT, Journal of Coatings Technology*, **62** (786): 55-61

Decker, C., 1998, The Use of UV Irradiation in Polymerization, *Polymer International*, **45** (2): 133-141

Decker, C., 2002, Kinetic Study and New Applications of UV Radiation Curing, *Macromolecular Rapid Communications*, **23** (18): 1067-1093

Decker, C., 2002, Light-induced Crosslinking Polymerization, *Polymer International*, **51** (11): 1141-1150

Drobny, J., 2014, 14-Thermoplastic Elastomers Based on Recycled Rubber and Plastics, *Handbook of Thermoplastic Elastomers (Second Edition)*: 297-299

Fang, C., Jing, Y., Zong, Y. and Lin, Z., 2017, Effect of Trifunctional Crosslinker Triallyl Isocyanurate (TAIC) on the Surface Morphology and Viscoelasticity of the Acrylic Emulsion Pressure-Sensitive Adhesives, *Journal of Adhesion Science and Technology*, **31** (8): 858-873

Ferry, J. D., *Viscoelastic Properties of Polymers*, 1980, John Wiley & Sons

Flory, P. and Rehner, J., Statistical Mechanics of Crosslinked Polymer Networks II. Rubberlike Elasticity, *Journal of Chemistry. Pi*: 512-520

Flory, P. J. and Rehner Jr, J., 1943, Statistical Mechanics of Cross-linked

Polymer Networks II. Swelling, *The Journal of Chemical Physics*, **11** (11): 521-526

Flory, P. J., 1950, Statistical Mechanics of Swelling of Network Structures, *The Journal of Chemical Physics*, **18** (1): 108-111

Flory, P. J., Principles of Polymer Chemistry, 1953, Cornell University Press

Gallagher, J. J., Hillmyer, M. A. and Reineke, T. M., 2016, Acrylic Triblock Copolymers Incorporating Isosorbide for Pressure Sensitive Adhesives, *ACS Sustainable Chemistry & Engineering*, **4** (6): 3379-3387

Gao, J., Li, X., Lu, Q., Li, Y., Ma, D. and Yang, W., 2012, Synthesis and Characterization of Poly (methyl methacrylate-butyl acrylate) by Using Glow-Discharge Electrolysis Plasma, *Polymer Bulletin*, **68**: 37-51

Garboczi, E. J. and Day, A. R., 1995, An Algorithm for Computing the Effective Linear Elastic Properties of Heterogeneous Materials: Three-Dimensional Results for Composites with Equal Phase Poisson ratios, *Journal of the Mechanics and Physics of Solids*, **43** (9): 1349-1362

Gdalin, B. E., Bermesheva, E. V., Shandryuk, G. A. and Feldstein, M. M., 2011, Effect of Temperature on Probe Tack Adhesion: Extension of the Dahlquist Criterion of Tack, *The Journal of Adhesion*, **87** (2): 111-138

Geffroy, B., Le Roy, P. and Prat, C., 2006, Organic Light-Emitting Diode (OLED) Technology: Materials, Devices and Display Technologies, *Polymer International*, **55** (6): 572-582

Ghatak, A., 2010, Peeling off an Adhesive Layer with Spatially Varying Modulus, *Physical Review E*, **81** (2): 021603

Hansen, C. M., 1995, Solubility Parameters, *Paint Testing Manual*, **17**: 383-404

Hashin, Z. and Shtrikman, S., 1961, Note on a Variational Approach to the Theory of Composite Elastic Materials, *Journal of the Franklin Institute*, **271** (4): 336-341

Hashin, Z., 1965, Elasticity of Random Media, *Transactions of the Society of Rheology*, **9** (1): 381-406

Hashin, Z. a. and Shtrikman, S., 1962, On Some Variational Principles in Anisotropic and Nonhomogeneous Elasticity, *Journal of the Mechanics and Physics of Solids*, **10** (4): 335-342

He, M., 1989, Hutchinson. Crack Deflection at an Interface between Dissimilar Elastic Materials, *International Journal of Solids Structure*, **25** (9): 1053-1067

Hill, R., 1963, Elastic Properties of Reinforced Solids: Some Theoretical Principles, *Journal of the Mechanics and Physics of Solids*, **11** (5): 357-372

Hioe, J. and Zipse, H., 2010, Radical Stability and Its Role in Synthesis and Catalysis. *Organic and Biomolecular Chemistry*, **8** (16): 3609-3617

Hori, M. and Yonezawa, F., 1975, Statistical Theory of Effective Electrical, Thermal, and Magnetic Properties of Random Heterogeneous Materials. IV. Effective-Medium Theory and Cumulant Expansion Method, *Journal of Mathematical Physics*, **16** (2): 352-364

Hösel, M., Søndergaard, R. R., Jørgensen, M. and Krebs, F. C., 2013, Comparison of UV-Curing, Hotmelt, and Pressure Sensitive Adhesive as Roll-to-Roll Encapsulation Methods for Polymer Solar Cells, *Advanced Engineering Materials*, **15** (11): 1068-1075

Huang, C.-I. and Lodge, T. P., 1998, Self-consistent Calculations of Block Copolymer Solution Phase Behavior, *Macromolecules*, **31** (11): 3556-3565

Ichimiya, H., Takinoue, M., Fukui, A., Miura, K., Yoshimura, T., Ashida, A., Fujimura, N. and Kiriya, D., 2018, Tuning Transition-Metal Dichalcogenide Field-Effect Transistors by Spontaneous Pattern Formation of an Ultrathin Molecular Dopant Film, *ACS Nano*, **12** (10): 10123-10129

Inaba, Y. and Asama, H., 2022, Spontaneous Patterning Method Utilizing Transformation of UV-curable Emulsion, *Scientific Reports*, **12** (1): 1-9

Ishikawa, N., Furutani, M. and Arimitsu, K., 2016, Pressure-sensitive Adhesive utilizing Molecular Interactions between Thymine and Adenine, *Journal of Polymer Science Part A: Polymer Chemistry*, **54** (10): 1332-1338

Jackson, E. A. and Hillmyer, M. A., 2010, Nanoporous Membranes Derived from Block Copolymers: from Drug Delivery to Water Filtration, *ACS Nano*, **4** (7): 3548-3553

Jaglinski, T., Kochmann, D., Stone, D. and Lakes, R. S., 2007, Composite Materials with Viscoelastic Stiffness Greater than Diamond, *Science*, **315** (5812): 620-622

Jeon, C., Han, J. J. and Seo, M., 2018, Control of Ion Transport in Sulfonated Mesoporous Polymer Membranes, *ACS Applied Materials & Interfaces*, **10** (47): 40854-40862

Jiang, X., Li, S. and Shao, L., 2017, Pushing CO₂-philic Membrane Performance to the Limit by Designing Semi-interpenetrating Networks (SIPN) for Sustainable CO₂ Separations, *Energy & Environmental Science*, **10** (6): 1339-1344

Jin, D. U., Kim, T. W., Koo, H. W., Stryakhilev, D., Kim, H. S., Seo, S. J., Kim, M. J., Min, H. K., Chung, H. K. and Kim, S. S., 2010, 47.1: Invited paper: Highly Robust Flexible AMOLED Display on Plastic Substrate with New Structure, *SID Symposium Digest of Technical Papers*, **41** (1): 703-705, Wiley Online Library

Joo, H.-S., Park, Y.-J., Do, H.-S., Kim, H.-J., Song, S.-Y. and Choi, K.-Y., 2007, The Curing Performance of UV-curable Semi-interpenetrating Polymer Network Structured Acrylic Pressure-sensitive Adhesives, *Journal of Adhesion Science and Technology*, **21** (7): 575-588

Jung, S., Kim, J. H., Kim, J., Choi, S., Lee, J., Park, I., Hyeon, T. and Kim, D. H., 2014, Reverse-micelle-induced Porous Pressure-sensitive Rubber for Wearable Human-machine Interfaces, *Advanced Materials*, **26** (28): 4825-4830

Kajtna, J. and Krajnc, M., 2013, "Design of Experiments" Analysis in Study of Solventless UV Crosslinkable Acrylic Pressure Sensitive Adhesives, *International Journal of Adhesion and Adhesives*, **41**: 152-159

Khandpur, A. K., Foerster, S., Bates, F. S., Hamley, I. W., Ryan, A. J., Bras, W., Almdal, K. and Mortensen, K., 1995, Polyisoprene-polystyrene Diblock Copolymer Phase Diagram near the Order-disorder Transition, *Macromolecules*, **28** (26): 8796-8806

Kim, H.-C., Park, S.-M. and Hinsberg, W. D., 2010, Block Copolymer Based Nanostructures: Materials, Processes, and Applications to Electronics, *Chemical Reviews*, **110** (1): 146-177

Kim, J., Shim, H. J., Yang, J., Choi, M. K., Kim, D. C., Kim, J., Hyeon, T. and Kim, D. H., 2017, Ultrathin quantum dot display integrated with wearable electronics, *Advanced Materials*, **29** (38): 1700217

Kim, S., Kwon, H. J., Lee, S., Shim, H., Chun, Y., Choi, W., Kwack, J., Han, D., Song, M. and Kim, S., 2011, Low-power Flexible Organic Light-emitting Diode Display Device, *Advanced Materials*, **23** (31): 3511-3516

Koleske, J. V., 2012, Paint and Coating Testing Manual 15th Edition of the Gardner-Sward Handbook, *ASTM International: West Conshohocken, PA, USA*.

Kondo, S. and Miura, T., 2010, Reaction-diffusion Model as a Framework for Understanding Biological Pattern Formation, *Science*, **329** (5999): 1616-1620

Koo, I. M., Jung, K., Koo, J. C., Nam, J.-D., Lee, Y. K. and Choi, H. R., 2008, Development of Soft-actuator-based Wearable Tactile Display, *IEEE Transactions on Robotics*, **24** (3): 549-558

Kraus, G., Jones, F., Marrs, O. and Rollmann, K., 1976, Morphology and

Viscoelastic Behavior of Styrene-diene Block Copolymers in Pressure Sensitive Adhesives, *The Journal of Adhesion*, **8** (3): 235-258

Lee, J.-G., Shim, G.-S., Park, J.-W., Kim, H.-J. and Han, K.-Y., 2016, Kinetic and Mechanical Properties of Dual Curable Adhesives for Display Bonding Process, *International Journal of Adhesion and Adhesives*, **70**: 249-259

Lee, J.-H., Lee, T.-H., Shim, K.-S., Park, J.-W., Kim, H.-J., Kim, Y. and Jung, S., 2017, Effect of Crosslinking Density on Adhesion Performance and Flexibility Properties of Acrylic Pressure Sensitive Adhesives for Flexible Display Applications, *International Journal of Adhesion and Adhesives*, **74**: 137-143

Lee, J.-H., Kim, K.-M., Kim, H.-J. and Kim, Y., 2021, Ultraviolet-patterned Acrylic Pressure-sensitive Adhesives for Flexible Displays, *Polymer*, **237**: 124324

Lee, S.-W., Park, J.-W., Kwon, Y.-E., Kim, S., Kim, H.-J., Kim, E.-A., Woo, H.-S. and Swiderska, J., 2012, Optical Properties and UV-curing Behaviors of Optically Clear Semi-interpenetrated Structured Acrylic Pressure Sensitive Adhesives, *International Journal of Adhesion and Adhesives*, **38**: 5-10

Lee, S.-W., Park, J.-W., Park, C.-H., Kwon, Y.-E., Kim, H.-J., Kim, E.-A., Woo, H.-S., Schwartz, S., Rafailovich, M. and Sokolov, J., 2013, Optical Properties and UV-curing Behaviors of Optically Clear PSA-TiO₂ Nano-composites, *International Journal of Adhesion and Adhesives*, **44**: 200-208

Lee, S.-W., Park, J.-W., Park, C.-H. and Kim, H.-J., 2014, Enhanced Optical

Properties and Thermal Stability of Optically Clear Adhesives, *International Journal of Adhesion and Adhesives*, **50**: 93-95

Lee, S. S., Luciani, A. and Månson, J.-A. E., 2000, A Rheological Characterisation Technique for Fast UV-curable Systems, *Progress in Organic Coatings*, **38** (3): 193-197

Lee, T.-H., Kim, J.-S., Lee, J.-H. and Kim, H.-J., Pressure-sensitive Adhesives for Flexible Display Applications, 2019, in *Hybrid Nanomaterials-Flexible Electronics Materials*, IntechOpen

Leguizamón, S. C., Powers, J., Ahn, J., Dickens, S., Lee, S. and Jones, B. H., 2021, Polymerization-induced Phase Separation in Rubber-toughened Amine-cured Epoxy Resins: tuning Morphology from the Nano-to Macro-scale, *Macromolecules*, **54** (17): 7796-7807

Lequieu, J. and Magenau, A. J., 2021, Reaction-induced Phase Transitions with Block Copolymers in Solution and Bulk, *Polymer Chemistry*, **12** (1): 12-28

Levinson, H. J., Principles of Lithography, 2005, SPIE press

Li, D., Zhan, W., Zuo, W., Li, L., Zhang, J., Cai, G. and Tian, Y., 2022, Elastic, Tough and Switchable Swelling Hydrogels with High Entanglements and Low Crosslinks for Water Remediation, *Chemical Engineering Journal*, **450**: 138417

Li, G., Wang, W., Yang, W., Lin, Y., Wang, H., Lin, Z. and Zhou, S., 2016, GaN-based Light-emitting Diodes on Various Substrates: a critical review, *Reports*

on *Progress in Physics*, **79** (5): 056501

Li, L., Tirrell, M., Korba, G. A. and Pocius, A. V., 2001, Surface Energy and Adhesion Studies on Acrylic Pressure Sensitive Adhesives, *The Journal of Adhesion*, **76** (4): 307-334

Li, X., Liu, Z., Cui, S., Luo, C., Li, C. and Zhuang, Z., 2019, Predicting the Effective Mechanical Property of Heterogeneous Materials by Image Based Modeling and Deep Learning, *Computer Methods in Applied Mechanics and Engineering*, **347**: 735-753

Lilliu, G., Van Mier, J. and van Vliet, M., 1999, Numerical Characterization of the Elastic Properties of Heterogeneous Materials with a 3D Lattice Model, *WIT Transactions on Modelling and Simulation*, **22**:

Lindvig, T., Michelsen, M. L. and Kontogeorgis, G. M., 2002, A Flory–Huggins Model Based on the Hansen Solubility Parameters, *Fluid Phase Equilibria*, **203** (1-2): 247-260

Liu, L., Wu, Z., Zheng, Z., Zhou, Q., Chen, K. and Yin, P., 2022, Polymerization-induced Microphase Separation of Polymer-polyoxometalate Nanocomposites for Anhydrous Solid State Electrolytes, *Chinese Chemical Letters*, **33** (9): 4326-4330

Lodge, T. P., Pudil, B. and Hanley, K. J., 2002, The Full Phase Behavior for Block Copolymers in Solvents of Varying Selectivity, *Macromolecules*, **35** (12): 4707-4717

Lurie, A. I., Theory of Elasticity, 2010, Springer Science & Business Media

Luzhnica, G. and Veas, E., 2018, Investigating Interactions for Text Recognition Using a Vibrotactile Wearable Display, *23rd International Conference on Intelligent User Interfaces*: 453-465,

Maag, K., Lenhard, W. and Löffles, H., 2000, New UV Curing Systems for Automotive Applications, *Progress in Organic Coatings*, **40** (1-4): 93-97

Mai, Y. and Eisenberg, A., 2012, Self-assembly of Block Copolymers, *Chemical Society Reviews*, **41** (18): 5969-5985

Malescio, G. and Pellicane, G., 2003, Stripe Phases from Isotropic Repulsive Interactions, *Nature Materials*, **2** (2): 97-100

Måløy, K. J. and Schmittbuhl, J., 2001, Dynamical Event during Slow Crack Propagation, *Physical Review Letters*, **87** (10): 105502

Mapari, S., Mestry, S. and Mhaske, S., 2020, Developments in Pressure-Sensitive Adhesives: a review, *Polymer Bulletin*: 1-34

McIntosh, L. D., Schulze, M. W., Irwin, M. T., Hillmyer, M. A. and Lodge, T. P., 2015, Evolution of Morphology, Modulus, and Conductivity in Polymer Electrolytes prepared via Polymerization-induced Phase Separation, *Macromolecules*, **48** (5): 1418-1428

Melodia, D., Bhadra, A., Lee, K., Kuchel, R., Kundu, D., Corrigan, N. and Boyer, C., 2023, 3D Printed Solid Polymer Electrolytes with Bicontinuous Nanoscopic Domains for Ionic Liquid Conduction and Energy Storage, *Small*:

2206639

Micutz, M., Aricov, L., Ilie, C. and Staicu, T., 2016, Tailoring Rheological Properties of Uncrosslinked Water-borne Pressure-sensitive Adhesives by Means of Polymer Maximum Volume Fraction, *International Journal of Adhesion and Adhesives*, **70**: 10-16

Milton, G., 2002, *The Theory of Composites* (Cambridge Monographs on Applied and Computational Mathematics) Cambridge University Press, Cambridge, UK.

Moreau, W. M., *Semiconductor Lithography: Principles, Practices, and Materials*, 2012, Springer Science & Business Media

Motokawa, R., Iida, Y., Zhao, Y., Hashimoto, T. and Koizumi, S., 2007, Living Polymerization Induced Macro-and Microdomain Investigated by Focusing Ultra-small-angle Neutron Scattering, *Polymer journal*, **39** (12): 1312-1318

Nason, C., Roper, T., Hoyle, C. and Pojman, J. A., 2005, UV-induced Frontal Polymerization of Multifunctional (Meth) Acrylates, *Macromolecules*, **38** (13): 5506-5512

Nemat-Nasser, S. and Hori, M., *Micromechanics: Overall Properties of Heterogeneous Materials*, 2013, Elsevier

Ni, Y. and Chiang, M. Y. M., 2007, Prediction of Elastic Properties of Heterogeneous Materials with Complex Microstructures, *Journal of the Mechanics and Physics of Solids*, **55** (3): 517-532

Noori, H., Jain, M., Nielsen, K. and Brandys, F., 2018, Delamination in Deformed Polymer Laminated Sheet Metals, *International Journal of Adhesion and Adhesives*, **85**: 219-224

Oh, T., Cho, S., Yoo, C., Yeo, W., Oh, J. and Seo, M., 2023, Polymerization-Induced Microphase Separation of a Polymerization Mixture into Nanostructured Block Polymer Materials, *Progress in Polymer Science*: 101738

Oliver, W. C. and Pharr, G. M., 1992, An Improved Technique for Determining Hardness and Elastic Modulus using Load and Displacement Sensing Indentation Experiments, *Journal of Materials Research*, **7** (6): 1564-1583

Othmer, H. G., Painter, K., Umulis, D. and Xue, C., 2009, The Intersection of Theory and Application in Elucidating Pattern Formation in Developmental Biology, *Mathematical Modelling of Natural Phenomena*, **4** (4): 3-82

Paine, D. C., Yeom, H.-Y. and Yaglioglu, B., 2005, Transparent conducting oxide materials and technology, *Flexible flat panel displays*: 79-98

Park, C.-H., Lee, S.-J., Lee, T.-H. and Kim, H.-J., 2015, Characterization of an Acrylic Polymer Under Hygrothermal Aging as an Optically Clear Adhesive for Touch Screen Panels, *International Journal of Adhesion and Adhesives*, **63**: 137-144

Park, C.-H., Lee, S.-J., Lee, T.-H. and Kim, H.-J., 2016, Characterization of an Acrylic Pressure-sensitive Adhesive Blended with Hydrophilic Monomer Exposed to Hygrothermal Aging: Assigning Cloud Point Resistance as an

Optically Clear Adhesive for a Touch Screen Panel, *Reactive Functional Polymers*, **100**: 130-141

Park, J.-S., Kim, T.-W., Stryakhilev, D., Lee, J.-S., An, S.-G., Pyo, Y.-S., Lee, D.-B., Mo, Y. G., Jin, D.-U. and Chung, H. K., 2009, Flexible Full Color Organic Light-Emitting Diode Display on Polyimide Plastic Substrate Driven by Amorphous Indium Gallium Zinc Oxide Thin-Film Transistors, *Applied Physics Letters*, **95** (1): 013503

Park, J.-w., Lee, S.-J., Jung, H.-W., Ahn, H.-S., Kim, H.-J., Cho, J. K., Kim, B., Shin, S. and Hwang, T.-S., 2016, Evaluation of Soft Adhesives Containing Dual-Curable Melamine-based Compounds, *International Journal of Adhesion and Adhesives*, **70**: 315-321

Park, J., Kim, K. and Seo, M., 2018, Hyper-cross-linked Polymers with Controlled Multiscale Porosity via Polymerization-induced Microphase Separation within High Internal Phase Emulsion, *Chemical Communications*, **54** (57): 7908-7911

Pawin, G., Wong, K. L., Kwon, K.-Y. and Bartels, L., 2006, A Homomolecular Porous Network at a Cu (111) Surface, *Science*, **313** (5789): 961-962

Penfold, N. J., Yeow, J., Boyer, C. and Armes, S. P., 2019, Emerging Trends in Polymerization-induced Self-assembly, *ACS Macro Letters*, **8** (8): 1029-1054

Peng, S., Lohse, D. and Zhang, X., 2015, Spontaneous Pattern Formation of Surface Nanodroplets from Competitive Growth, *ACS Nano*, **9** (12): 11916-11923

Peterson, C. H., Werber, J. R., Lee, H. K. and Hillmyer, M. A., 2022, Tailored Mesoporous Microspheres by Polymerization-Induced Microphase Separation in Suspension, *ACS Applied Polymer Materials*, **4** (6): 4219-4233

Pharr, G. and Oliver, W., 1992, Measurement of Thin Film Mechanical Properties using Nanoindentation, *MRS Bulletin*, **17** (7): 28-33

Phillip, W. A., O'Neill, B., Rodwogin, M., Hillmyer, M. A. and Cussler, E., 2010, Self-assembled Block Copolymer Thin Films as Water Filtration membranes, *ACS Applied Materials & Interfaces*, **2** (3): 847-853

Pokeržnik, N. and Krajnc, M., 2015, Synthesis of a Glucose-based Surfmer and Its Copolymerization with n-butyl Acrylate for Emulsion Pressure Sensitive Adhesives, *European Polymer Journal*, **68**: 558-572

Ponson, L., 2009, Depinning Transition in the Failure of Inhomogeneous Brittle Materials, *Physical Review Letters*, **103** (5): 055501

Qi, S., Groves, J. T. and Chakraborty, A. K., 2001, Synaptic Pattern Formation during Cellular Recognition, *Proceedings of the National Academy of Sciences*, **98** (12): 6548-6553

Rajoriya, A., Shrivastava, M., Gossner, H., Schulz, T. and Rao, V. R., 2013, Sub 0.5 V Operation of Performance Driven Mobile Systems based on Area Scaled Tunnel FET Devices, *IEEE Transactions on Electron Devices*, **60** (8): 2626-2633

Rivlin, R. S., Barenblatt, G. I. and Joseph, D. D., Collected Papers of RS Rivlin,

1997, Springer Science & Business Media

Rothenburg, L., Ai. Berlin, A. I. and Bathurst, R. J., 1991, Microstructure of Isotropic Materials with Negative Poisson's Ratio, *Nature*, **354** (6353): 470-472

Roux, S. and Hild, F., 2008, Self-consistent Scheme for Toughness Homogenization, *International Journal of Fracture*, **154** (1): 159-166

Sajjad, H., Tolman, W. B. and Reineke, T. M., 2020, Block Copolymer Pressure-sensitive Adhesives derived from Fatty Acids and Triacetic Acid Lactone, *ACS Applied Polymer Materials*, **2** (7): 2719-2728

Samid-Merzel, N., Lipson, S. and Tannhauser, D., 1998, Pattern Formation in Drying Water Films, *Physical Review E*, **57** (3): 2906

Sanchez-Palencia, E. and Zaoui, A., 1987, Homogenization Techniques for Composite Media, *Homogenization Techniques for Composite Media*, **272**:

Satas, D., Handbook of Pressure Sensitive Adhesive Technology, 1989, Springer

Schulze, M. W., McIntosh, L. D., Hillmyer, M. A. and Lodge, T. P., 2014, High-Modulus, High-conductivity Nanostructured Polymer Electrolyte Membranes via Polymerization-induced Phase Separation, *Nano Letters*, **14** (1): 122-126

Schulze, M. W. and Hillmyer, M. A., 2017, Tuning Mesoporosity in Cross-linked Nanostructured Thermosets via Polymerization-induced Microphase Separation, *Macromolecules*, **50** (3): 997-1007

Seo, M. and Hillmyer, M. A., 2012, Reticulated Nanoporous Polymers by Controlled Polymerization-induced Microphase Separation, *Science*, **336** (6087): 1422-1425

Sethna, J. P., Dahmen, K. A. and Myers, C. R., 2001, Crackling Noise, *Nature*, **410** (6825): 242-250

Shanmugam, S., Cuthbert, J., Kowalewski, T., Boyer, C., and Matyjaszewski, K., 2018, Catalyst-free Selective Photoactivation of RAFT Polymerization: a Facile Route for Preparation of Comblike and Bottlebrush Polymers. *Macromolecules*, **51** (19): 7776-7784

Shen, H., Zhang, L. and Eisenberg, A., 1999, Multiple PH-induced Morphological Changes in Aggregates of Polystyrene-block-poly (4-vinylpyridine) in DMF/H₂O Mixtures, *Journal of the American Chemical Society*, **121** (12): 2728-2740

Shi, X., Yao, Y., Zhang, J., Corrigan, N. and Boyer, C., 2023, Polymerization Induced Microphase Separation of ABC Triblock Copolymers for 3D Printing Nanostructured Materials, *Small*: 2305268

Shyer, A. E., Rodrigues, A. R., Schroeder, G. G., Kassianidou, E., Kumar, S. and Harland, R. M., 2017, Emergent Cellular Self-organization and Mechanosensation Initiate Follicle Pattern in the Avian Skin, *Science*, **357** (6353): 811-815

Swift, T., Swanson, L., Geoghegan, M. and Rimmer, S., 2016, The pH-Responsive Behaviour of Poly (Acrylic Acid) in Aqueous Solution is

Dependent on Molar Mass, *Soft Matter*, **12** (9): 2542-2549

Tan, H. S. and Pfister, W. R., 1999, Pressure-sensitive Adhesives for Transdermal Drug Delivery Systems, *Pharmaceutical Science & Technology Today*, **2** (2): 60-69

Tanase, H., Mamiya, J. and Suzuki, M., 1998, A new Backlighting System using a Polarizing Light Pipe, *IBM Journal of Research and Development*, **42** (3.4): 527-536

Thomas, E. L., Anderson, D. M., Henkee, C. S. and Hoffman, D., 1988, Periodic Area-minimizing Surfaces in Block Copolymers, *Nature*, **334** (6183): 598-601

Thompson, L. F., *An Introduction to Lithography*, 1983, ACS Publications

Townsend, K. J., Busse, K., Kressler, J. and Scholz, C., 2005, Contact Angle, WAXS, and SAXS Analysis of Poly (β -hydroxybutyrate) and Poly (ethylene glycol) Block Copolymers Obtained via *Azotobacter vinelandii* UWD, *Biotechnology Progress*, **21** (3): 959-964

Tse, M. F., 1989, Studies of Triblock Copolymer-tackifying Resin Interactions by Viscoelasticity and Adhesive Performance, *Journal of Adhesion Science and Technology*, **3** (1): 551-570

Tse, M. F. and Jacob, L., 1996, Pressure Sensitive Adhesives based on Vectorr Sis Polymers I. Rheological Model and Adhesive Design Pathways, *The Journal of Adhesion*, **56** (1-4): 79-95

Van Hest, J., Delnoye, D., Baars, M., Van Genderen, M. and Meijer, E., 1995, Polystyrene-dendrimer Amphiphilic Block Copolymers with a Generation-Dependent Aggregation, *Science*, **268** (5217): 1592-1595

Vandenbrouck, F., Valignat, M. and Cazabat, A., 1999, Thin Nematic Films: Metastability and Spinodal Dewetting, *Physical Review Letters*, **82** (13): 2693

Walpole, L., 1966, On Bounds for the Overall Elastic Moduli of Inhomogeneous Systems—II, *Journal of the Mechanics and Physics of Solids*, **14** (5): 289-301

Walpole, L., 1966, On Bounds for the Overall Elastic Moduli of Inhomogeneous systems—I, *Journal of the Mechanics and Physics of Solids*, **14** (3): 151-162

Watt, J. P., Davies, G. F. and O'Connell, R. J., 1976, The Elastic Properties of Composite Materials, *Reviews of Geophysics*, **14** (4): 541-563

Whitesides, G. M., Mathias, J. P. and Seto, C. T., 1991, Molecular Self-Assembly and Nanochemistry: a Chemical Strategy for the Synthesis of Nanostructures, *Science*, **254** (5036): 1312-1319

Williams, E. D., Ayres, R. U. and Heller, M., 2002, The 1.7 Kilogram Microchip: Energy and Material Use in the Production of Semiconductor Devices, *Environmental Science & Technology*, **36** (24): 5504-5510

Xia, S., Ponson, L., Ravichandran, G. and Bhattacharya, K., 2012, Toughening and Asymmetry in Peeling of Heterogeneous Adhesives, *Physical Review*

Letters, **108** (19): 196101

Xia, S., Ponson, L., Ravichandran, G. and Bhattacharya, K., 2013, Adhesion of Heterogeneous Thin Films—I: Elastic Heterogeneity, *Journal of the Mechanics and Physics of Solids*, **61** (3): 838-851

Yamamoto, M., Nakano, F., Doi, T. and Moroishi, Y., 2002, Synthesis and PSA Performance Study for Novel Acrylic and Butyl Acrylate Block Copolymers, *International Journal of Adhesion and Adhesives*, **22** (1): 37-40

Yamanaka, K., Takagi, Y. and Inoue, T., 1989, Reaction-induced Phase Separation in Rubber-modified Epoxy Resins, *Polymer*, **30** (10): 1839-1844

Yoo, D., Won, D. J., Cho, W., Kim, S. and Kim, J., 2021, High-Resolution and Facile Patterning of Silver Nanowire Electrodes by Solvent-Free Photolithographic Technique Using UV-Curable Pressure Sensitive Adhesive Film, *Small Methods*, **5** (12): 2101049

Zhang, L. and Eisenberg, A., 1995, Multiple Morphologies of "Crew-cut" Aggregates of Polystyrene-b-poly (Acrylic Acid) Block Copolymers, *Science*, **268** (5218): 1728-1731

Zhang, L., Yu, K. and Eisenberg, A., 1996, Ion-induced Morphological Changes in "Crew-Cut" Aggregates of Amphiphilic Block Copolymers, *Science*, **272** (5269): 1777-1779

Zhou, L., Wang, A., Wu, S.-C., Sun, J., Park, S. and Jackson, T. N., 2006, All-Organic Active Matrix Flexible Display, *Applied Physics Letters*, **88** (8):

083502

List of Publications

This Ph.D. dissertation is based on the following publications.

- I. Kim, J. S., Hwang, J. U., Baek, D., Kim, H. J., & Kim, Y. 2021. Characterization and Flexibility Properties of UV LED Cured Acrylic Pressure-Sensitive Adhesives for Flexible Displays. *Journal of Materials Research and Technology*, 10, 1176-1183.

- II. Kim, J. S., Shim, G. S., Baek, D., Back, J. H., Jang, S. W., Kim, H. J., ... and Yeom, J. S. 2019. UV/UV step-curing of Optically Clear Acrylate Adhesives for Mobile Devices. *Express Polymer Letters*, 13 9.

- III. Kim, J. S., Kim, H. J., and Kim, Y. D. 2021. Flexibility Properties of Pressure-Sensitive Adhesive with Different Pattern of Crosslinking Density for Electronic Displays. *Journal of Materials Research and Technology*, 15, 1408-1415.

- IV. Kim, J. S., Back, J. H., Yi, M. B., Lee, S. J., Han, G. Y.,...,and Kim, H. J., Elastomeric Acrylic Pressure-Sensitive Adhesives for Flexible Display using Polymerization induced Microphase Separation, **in preparation.**

국문 초록

아크릴계 고분자는 분자 스스로 점착력을 나타내며 우수한 투명성을 지니는 장점이 있기 때문에 새로운 세대의 광학적, 전기적 장치 부품에 아크릴 점착 필름을 활용하고자 하는 연구가 계속되고 있다. 스트레처블 디스플레이와 같은 첨단 기능성 재료로의 적용을 위해서는 더 넓은 변형 영역에 걸친 탄성 거동이 요구되며 현재까지는 점착소재의 저온 모듈러스를 저감하는 것이 주된 개선 방향으로 연구되고 있다. 그러나 아크릴 점착 필름의 탄성 개선에 대한 기존 접근들은 점착 물성의 향상과는 상충되는 한계를 가지므로 본 논문에서는 점착 소재의 구조를 비균질화하여 탄성력과 점착력을 모두 개선하는 것을 그에 대한 해결책으로 제시하고자 한다. 고분자의 비균질화는 물성적으로 획기적인 변화를 나타낼 수 있어 전극과 다공성 전달체 등 다양한 분야에서의 적용이 활발하며 그 형태와 물성을 이해하는 시도들은 고분자 공중합체에 대한 기본적 물리화학에 기초하여 진보되고 있다. 따라서 아크릴 고분자의 비균질화에 따른 점착 소재의 형태학적, 분자 구조적, 물성적 이해는 가치있는 탐구 주제가 된다.

본 논문에서는 포토리소그래피와 PIMS를 각각 이용하여 아크릴 폴리머의 분자 구조를 보다 정밀하게 비균질화하는 방안을 연구하였으며 고분자 비균질화에 따른 점착 재료의 물성을 유변학적, 기계적 측면에서 체계적으로 살펴보고 고분자 가교 네트워크와 사슬 말단 길이의 변화에 따른 박막의 형태와 물성에 대해 연구함으로써 비균질화한 고분자 박막의 상 거동을 보다 깊이 이해하고 그것의

응용 가능성을 증대하는 것에 기여하고자 하였다.

제 1장에서는 아크릴 점착 소재의 유연 물성 개선 연구에 대한 중요성을 언급하고 비균질화를 통한 점착 소재의 물성 개선에 대한 이론적, 실험적 결과들을 정리하였다. 그리고 본 연구에서 아크릴 공중합체의 비균질화를 부여하는 주요 기술로서 활용한 중합 유도 미세상분리 법을 소개하였다.

제 2장에서는 포토리소그래피를 적용하기 위한 기초 연구를 진행하였으며 포토리소그래피 방법으로 비균질화한 점착 소재를 제조하고 비균질화된 점착 소재의 물성 개선 가능성을 확인하였다.

제 3장에서는 리빙라디칼 중합을 활용하여 PIMS 방법으로 부드러운 선형 고분자를 사슬 말단으로 갖는 가교 네트워크를 제조하였다. 고분자 네트워크의 구조와 상 거동 및 유연학적, 물리적 물성의 관계를 정리하였으며 제조한 비균질 점착 소재의 획기적인 넓은 선형 탄성 거동을 확인하였다.

제 4장에서는 사슬 말단의 선형 고분자 블록의 길이에 따른 공중합체 네트워크의 상 거동을 STEM을 이용하여 연구한 내용을 보고하였다. 리빙라디칼 중합 유도 미세 상분리 고분자의 자가 조립 형상을 가시화하여 보고한 것에서 나아가 Flory-Rehner 관계식의 확장을 토대로 분자 구조를 세분화하여 명확히 밝히고자 하였다. 미세 비균질화를 부여한 점착 소재의 분자 구조적 해석과 물성을 연관하여 이해하고 유연 디스플레이용 투명 점착 소재로의 적용 가능성을 검토하였다.

키워드 : 아크릴 점착소재, 유연 디스플레이용 점착소재, 엘라스토머, 비균질화, 포토리소그래피, 중합 유도 미세 상분리.

학 번 : 2018-29259